

**Sofia Batalha de
Oliveira
Pascoal Amado**

**Equalização Digital Para Sistemas de Transmissão
Ópticos Coerentes**

**Digital Equalization for Optical Coherent
Transmission Systems**

Sofia Batalha de
Oliveira
Pascoal Amado

Equalização Digital Para Sistemas de Transmissão Ópticos Coerentes

Digital Equalization for Optical Coherent Transmission Systems

Tese apresentada à Universidade de Aveiro para cumprimento dos requisitos necessários à obtenção do grau de Doutor em Telecomunicações, realizada sob a orientação do Professor Doutor Armando Humberto Moreira Nolasco Pinto, Professor Associado do Departamento de Electrónica, Telecomunicações e Informática da Universidade de Aveiro, e sob a co-orientação do Doutor Nelson de Jesus Cordeiro Muga, investigador sénior do Instituto de Telecomunicações de Aveiro

Apoio financeiro da Fundação para a Ciência e a Tecnologia (FCT) através das bolsas PD/BD/52593/2014 e da FCT e do Fundo Europeu de Desenvolvimento Regional (FEDER) através do Programa Operacional Factores de Competitividade (COMPETE) e do Quadro de Referência Estratégico Nacional (QREN) no âmbito dos projetos PTDC/EEI-TEL/3283/2012 (DiNEq), POCI-01-0145-FEDER-029405 (DSPMetroNet) e UID/EEA/50008/2013 (SoftTransceiver e Optical-5G).

FCT Fundação para a Ciência e a Tecnologia

MINISTÉRIO DA CIÊNCIA, TECNOLOGIA E ENSINO SUPERIOR Portugal

Instituição de acolhimento:



o júri / the jury

presidente / president

Doutora Maria Manuel Rocha Teixeira Baptista

Professora Catedrática da Universidade de Aveiro

vogais / examiners committee

Doutor Henrique José Almeida da Silva

Professor Associado da Faculdade de Ciências e Tecnologia da Universidade de Coimbra

Doutor Henrique Manuel de Castro Faria Salgado

Professor Associado da Faculdade de Engenharia da Universidade do Porto

Doutora Maria do Carmo Raposo de Medeiros

Professora Associada da Universidade de Coimbra

Doutor João Lopes Rebola

Professor Auxiliar do Instituto Universitário de Lisboa

Doutor Armando Humberto Moreira Nolasco Pinto

Professor Associado da Universidade de Aveiro (orientador)

agradecimentos / acknowledgements

Há cinco anos iniciei esta aventura não certa de que estaria a tomar a decisão correcta. Neste momento não poderia estar mais certa. É com muita pena mas também com um grande alívio que chego ao fim deste longo mas gratificante percurso académico, repleto de novas experiências, aprendizagens, compromissos e conquistas, que me fizeram crescer e aprender a lutar sem nunca desistir.

O sucesso deste trabalho foi apenas possível graças à ajuda e apoio incondicional de um conjunto de pessoas a quem gostaria de deixar aqui o meu profundo e sentido agradecimento. Começo por agradecer ao meu orientador, professor Armando Nolasco Pinto, por ter aceite orientar-me e por todo o conhecimento que me transmitiu ao longo destes anos. Por todas as observações e sugestões feitas durante a revisão deste trabalho gostaria de agradecer ao meu coorientador, Nelson Jesus Muga. Por estar sempre disposto a ajudar, mesmo quando as horas vagas eram reduzidas, por todas as oportunidades de colaboração internacional que me proporcionou e por todas as ideias inovadoras e discussões estimulantes um obrigada especial ao Fernando Guiomar. Este que para além de colega de trabalho tornou-se num amigo para a vida. Aos meus colegas Ricardo Ferreira e Celestino Martins que para além de terem contribuído directamente para o trabalho aqui apresentado com estimulantes discussões, devo também um obrigado pelas gargalhadas e tranquilidade que me proporcionaram pela forma descomplicada com que encaram a vida. Agradeço também a contribuição preponderante para este trabalho dada pelo Dr. Andrea Carena e Dr. Jacklyn Reis, cujo apoio científico nas colaborações estabelecidas foi determinante para melhorar a qualidade do trabalho desenvolvido. Agradeço ainda aos meus novos colegas de trabalho da Cisco Optical GmbH pelo seu papel motivador e inspirador para a conclusão da minha dissertação de doutoramento.

Aos meus pais por terem sido sempre um exemplo de vida para mim, na maneira como sempre trabalharam e lutaram arduamente para alcançar os seus objectivos. Tenho a certeza que foi de vós que herdei toda a minha determinação e perseverança. À minha irmã pela sua veia de psicóloga sempre com palavras de apoio e motivação nos momentos mais difíceis. Obrigada pela vossa paciência e por sempre terem acreditado em mim. Finalmente ao Fábio, devo-te a ti a força para não desistir quando a única vontade era essa, foste sempre o meu pilar. Não há palavras que consigam descrever o quão grata te estou. Obrigada pelas valiosas sugestões e empolgantes discussões, obrigada por estares sempre disposto a ajudar, obrigada pelo teu suporte incondicional e pela tua paciência inesgotável. Obrigada por seres como és.

palavras-chave

Sistemas de comunicação ótica, formatos de modulação de ordem elevada, detecção coerente, processamento digital de sinal, supercanais, 400G, equalização não linear, propagação digital inversa.

resumo

A presente tese foca-se na equalização digital das distorções da fibra para sistemas óticos de transmissão coerente. São propostas novas técnicas eficientes e de baixa complexidade para a equalização e mitigação das distorções não lineares da fibra, e o compromisso entre desempenho e complexidade é testado numericamente e demonstrado experimental em sistemas de transmissão metro e longa distância baseados em supercanais 400G.

A propagação digital inversa baseada no método de split-step Fourier e equalizadores não lineares de séries de Volterra de baixa complexidade são testadas experimentalmente num sistema baseado em supercanais uniformes. Ao contrário dos métodos convencionais utilizados, estas técnicas podem ser implementadas utilizando menos interações e ainda estender o alcance do sistema face às técnicas de equalização linear. Para além disso, a complexidade do método baseado em Volterra pode ser facilmente ajustada alterando a dimensão do filtro não linear de acordo com os requisitos do sistema, concedendo assim maior flexibilidade ao bloco de equalização não linear.

Tendo em vista as futuras redes flexíveis, um supercanal híbrido na frequência é proposto de modo a aumentar a granularidade da taxa de transmissão do sistema. A problemática da relação de potência entre as portadoras do supercanal é abordada e otimizada em regimes de operação linear e não linear utilizando paradigmas diferentes de códigos correctores de erros. A aplicação de um único código corrector de erros à totalidade do supercanal mostra ser a abordagem mais robusta, tolerando maiores incertezas na optimização dos parâmetros do sistema.

O ganho de desempenho dado pela aplicação de diferentes técnicas de propagação digital inversa em sistemas de supercanais híbridos na frequência é também analisado, assim como as suas implicações na relação óptima de potência. Mostra-se que esta pode ser restringida à portadora que transporta o formato de modulação de ordem mais elevada, uma vez que o benefício trazido pelas restantes portadoras é negligenciável, permitindo reduzir significativamente a complexidade do algoritmo aplicado.

keywords

Optical communication systems, high-order modulation formats, coherent detection, digital signal processing, superchannels, 400G, nonlinear equalization, digital backpropagation.

abstract

This thesis focus on the digital equalization of fiber impairments for coherent optical transmission systems. New efficient and low-complexity equalization and mitigation techniques that counteract fiber nonlinear impairments are proposed and the tradeoff between performance and complexity is numerically assessed and experimentally demonstrated in metro and long-haul 400G superchannels-based transmission systems.

Digital backpropagation (DBP) based on low-complexity split-step Fourier method and Volterra series nonlinear equalizers are experimentally assessed in an uniform superchannel system. In contrast with standard DBP methods, these techniques prove to be able to be implemented with larger step-sizes, consequently requiring a reduced number of multiplications, and still achieve a significant reach extension over linear equalization techniques. Moreover, given its structure, the complexity of the proposed Volterra-based DBP approach can be easily adjusted by changing the nonlinear filter dimension according to the system requirements, thus providing a higher flexibility to the nonlinear equalization block.

A frequency-hybrid superchannel envisioning near-future flexible networks is then proposed as a way to increase the system bit-rate granularity. The problematic of the power-ratio between superchannel carriers is addressed and optimized for linear and nonlinear operation regimes using three distinct FEC paradigms. Applying a single FEC to the entire superchannel has a simpler implementation and is found to be a more robust approach, tolerating larger uncertainties on the system parameters optimization.

We also investigate the performance gain provided by the application of different DBP techniques in frequency-hybrid superchannel systems, and its implications on the optimum power-ratio. It is shown that the application of DBP can be restricted to the carrier transporting the higher cardinality QAM format, since the DBP benefit on the other carriers is negligible, which might bring a substantially complexity reduction of the DBP technique applied to the superchannel.

Contents

Contents	i
List of Figures	iii
List of Tables	vii
List of Acronyms	ix
List of Symbols	xv
1 Introduction	1
1.1 Motivation and Objectives	3
1.2 Thesis Outline	4
1.3 Main Contributions	5
1.4 List of Publications	6
1.4.1 Papers in international journals	6
1.4.2 Papers in conference proceedings	7
1.4.3 Patents	9
References	9
2 Coherent Transmission Systems	15
2.1 Digital Coherent Optical System	16
2.1.1 Coherent receiver	16
2.1.2 Coherent transmitter	19
2.2 Post-Detection Digital Signal Processing	21
2.2.1 Pre-processing	21
2.2.2 Channel equalization	22
2.2.3 Clock recovery	26
2.2.4 Carrier recovery	28
2.2.5 Symbol demapping	30
2.3 High-Order Modulation Formats	31
2.4 Hybrid Modulation Formats	33
2.5 Superchannels	36
2.6 Conclusions	40
References	40

3	Low-Complexity DBP Algorithms	55
3.1	Digital Backpropagation Concept	56
3.2	Digital Backpropagation Algorithms	59
3.2.1	Split-step Fourier method	59
3.2.2	Weighted split-step Fourier method	61
3.2.3	Time-domain Volterra series nonlinear equalizer	61
3.2.4	Weighted Volterra series nonlinear equalizer	64
3.3	400G WDM Transmission System	66
3.3.1	Experimental setup	66
3.3.2	Digital signal processing	67
3.4	Digital Backpropagation Optimization	69
3.5	Experimental Performance Analysis	72
3.6	Computational Effort	76
3.7	Conclusions	79
	References	80
4	Frequency-Hybrid Superchannel	85
4.1	Superchannel Configuration	86
4.2	Nonlinear Interference	87
4.2.1	Gaussian noise model	87
4.2.2	Enhanced Gaussian noise model	89
4.2.3	System performance estimation	89
4.3	400G Frequency-Hybrid Transmission System	90
4.3.1	Experimental setup	91
4.3.2	Digital signal processing	92
4.4	Individual Superchannel Carriers Performance	93
4.5	Joint Power-Ratio and FEC Optimization	96
4.5.1	FEC paradigms	96
4.5.2	Power ratio optimization	99
4.6	Advanced Nonlinear Compensation Strategies	106
4.7	Conclusions	108
	References	109
5	Conclusions and Future Work	113
5.1	Conclusions	113
5.2	Future work	115
	References	116

List of Figures

1.1	Cisco Visual Networking Index traffic forecast from the years 2016 to 2021, in exabytes per month.	1
2.1	Configuration of the coherent receiver employing phase and polarization diversity.	17
2.2	Configuration of the a dual-polarization in-phase and quadrature optical modulator.	19
2.3	Time-domain waveform of two adjacent <i>sinc</i> pulse shaping filters.	20
2.4	Configuration of the in-phase and quadrature modulator.	21
2.5	Post-detection digital signal processing subsystems used in coherent receivers.	22
2.6	Block diagram for the channel impairments equalization, where two concatenated blocks are applied to perform static and adaptive equalization of the signal independently.	23
2.7	Block diagram of the clock recovery algorithm.	27
2.8	Block diagram of the frequency recovery algorithm based on the differential phase-based method.	29
2.9	Block diagram of the phase recovery algorithm based on the Viterbi-Viterbi algorithm.	30
2.10	Theoretical bit-error ratio as a function of the signal-to-noise ratio for QPSK and M-QAM formats.	32
2.11	Structure of a frame based on time-domain hybrid modulation format between QPSK and 16QAM.	33
2.12	Spectrum of a transmitted signal based on frequency-domain hybrid modulation format, the hybrid between QPSK and 16QAM is considered.	35
2.13	WDM spectrum of a superchannel-based system, where each superchannel is made of five carriers separated by a guard-band.	37
3.1	Schematic representation of the digital backpropagation concept.	58
3.2	Block diagram depicting the implementation of the SSFM, where the linear and nonlinear steps are implemented in a serial configuration.	59
3.3	Block diagram depicting the implementation of the VSNE-based DBP techniques.	62
3.4	Block diagram depicting the implementation of the time-domain VSNE-based DBP approach.	63

3.5	Block diagram depicting the implementation of the W-VSNE-based DBP approach.	65
3.6	Laboratorial setup of an ultra-long-haul WDM transmission system composed of 5 dual-carrier PM-16QAM 400G superchannels.	67
3.7	Sequence of post-detection DSP algorithms for the processing of the dual-carrier PM-16QAM 400G superchannels.	68
3.8	Two stages N_{NL} and ξ parameters optimization for W-VSNE{0} algorithm, when considering an input power of -1 dBm, a propagation distance of 5000 km and the set of step-sizes considered in the evaluation of the algorithm.	70
3.9	N_{NL} optimization for W-SSFM and W-VSNE algorithms, considering an input power of -2 dBm, a propagation distance of 5000 km and a DBP step-size of 50 km and 500 km.	71
3.10	ξ optimization for W-SSFM and W-VSNE algorithms, considering an input power of -2 dBm, a propagation distance of 5000 km and a DBP step-size 500 km.	72
3.11	Performance of the linear and nonlinear equalization algorithms: BER as a function of the transmission distance, when considering a fixed DBP step-size of 500 km and an input power of -2 dBm.	73
3.12	Estimated maximum reach as a function of the input power, considering a fixed step-size of 500 km, for the different static equalization algorithms.	74
3.13	Estimated maximum reach as a function of the DBP step-size, for CDE, SSFM, W-SSFM and W-VSNE methods.	75
4.1	Proposed frequency-hybrid superchannel composed of a central PM-64QAM carrier and two edge PM-16QAM carriers, each carrier operating at 18 GBaud.	86
4.2	Experimental setup of an WDM transmission system composed by 9 of the proposed 400G frequency-hybrid superchannels.	91
4.3	Maximum reach as a function of the mean power per superchannel, for different values of PR between carriers, when considering CDE or alternatively DBP of each superchannel carrier.	94
4.4	Block diagram for the implementation of the considered FEC paradigms: a) SC-FEC and b) IC-FEC or Flex-FEC.	97
4.5	Pre-FEC BER as a function of the OH_{64QAM} and respective OH_{16QAM} , for a pos-FEC BER of 1×10^{-15}	99
4.6	Maximum reach as a function of the power-ratio for different sets of FEC OHs, when a) CDE and b) DBP are applied.	102
4.7	Maximum reach as a function of the OH_{64QAM} and OH_{16QAM} , for both CDE and DBP techniques.	103
4.8	System performance in terms of maximum reach as a function of power-ratio for the three FEC strategies, when applying a) CDE and b) DBP individually over each superchannel carrier.	104

4.9	Optimum mean power per superchannel as a function of power-ratio for both FEC strategies, when applying a) CDE and b) DBP on each superchannel carrier.	105
4.10	Theoretical performance comparison, in terms of maximum reach, for different DBP applications and for all three FEC paradigm: a) SC-FEC; b) IC-FEC and c) Flex-FEC.	107

List of Tables

3.1	Complexity and latency of DBP based on the SSFM, W-SSFM and W-VSNE as function of the transmission distance.	78
-----	--	----

List of Acronyms

100G 100 Gbit/s

400G 400 Gbit/s

1T 1 Tbit/s

ADC analog-to-digital converter

AOS acousto-optical switches

AOM acousto-optic modulators

ASE amplified spontaneous emission

ASIC application specific integrated circuit

AWGN additive white Gaussian noise

B2B back-to-back

BER bit-error rate

CD chromatic dispersion

CDE chromatic dispersion equalization

CMA constant modulus algorithm

CO-OFDM coherent orthogonal frequency division multiplexing

CPE carrier phase estimation

DA data-aided

DAC digital-to-analog converter

DBP digital backpropagation

DD decision-directed

DFB distributed feedback

DFT	discrete Fourier transform
DGD	differential-group delay
DSP	digital signal processing
DP-IQM	dual-polarization in-phase and quadrature modulator
ECL	external cavity laser
EDFA	erbium-doped fiber amplifier
EGN	enhanced Gaussian noise
ENOB	effective number of bits
FD	frequency-domain
FDHMF	frequency-domain hybrid modulation format
FEC	forward error correction
Flex-FEC	independent carrier flexible FEC
Flex-PAM	flexible pulse amplitude modulation
FFT	fast Fourier transform
FIR	finite impulse response
FWM	four-wave mixing
GN	Gaussian noise
GVD	group-velocity dispersion
LMS	least mean square
LO	local oscillator
LSPS	loop synchronous polarization scrambler
LUT	look-up-table
IC-FEC	independent carrier FEC
IFFT	inverse fast Fourier transform
IIR	infinite impulse response
IQM	in-phase and quadrature modulator
IP	Internet Protocol

ISI	inter-symbol interference
MC	multi-carrier
MCI	multi-channel interference
MIMO	multiple-input multiple-output
ML-DD	maximum likelihood decision-directed
MR	maximum reach
MSE	mean square error
MZM	Mach-Zehnder modulator
NCG	net coding gain
NLE	nonlinear equalization
NLI	nonlinear interference
NLSE	nonlinear Schrödinger equation
OH	overhead
OOK	on-off keying
OIF	Optical Internetworking Forum
OSNR	optical signal-to-noise ratio
PAM	pulse amplitude modulation
PBC	polarization beam combiner
PBS	polarization beam splitter
PDL	polarization dependent loss
PDM	polarization-division multiplexing
PI	polarization interleaving
PM	polarization-multiplexed
PMD	polarization-mode dispersion
PR	power-ratio
PRBS	pseudo random bit sequence
P/S	parallel-to-serial

PSCF	pure silica core fiber
PSD	power spectral density
PSK	phase-shift keying
P-SSFM	parallel SSFM
QAM	quadrature amplitude modulation
QPSK	quadrature phase-shift keying
RDE	radially-directed equalizer
RM	real multiplication
ROADM	reconfigurable optical add-drop multiplexer
SC-FEC	superchannel FEC
SCI	self-channel interference
SD-FEC	soft-decision FEC
SE	spectral efficiency
simVSNE	simplified Volterra series nonlinear equalizer
symVSNE	symmetric Volterra series nonlinear equalizer
S/P	serial-to-parallel
SPM	self-phase modulation
SNR	signal-to-noise ratio
SSFM	split-step Fourier method
SSMF	standard single-mode fiber
TD	time-domain
TDHMF	time-domain hybrid modulation format
ULA	ultra-low-area
ULH	ultra-long-haul
ULL	ultra-low-loss
VOA	variable optical attenuator
VSNE	Volterra series nonlinear equalizer

VSTF	Volterra series transfer function
WB	wide-band
WDM	wavelength-division multiplexing
WSS	wavelength selective switch
W-SSFM	weighted SSFM
W-VSNE	weighted VSNE
XCI	cross-channel interference
XPM	cross-phase modulation
XPolM	cross-polarization modulation

List of Symbols

Symbol	Designation
a_k	chromatic dispersion equalization filter taps
A_{eff}	effective core area
A_s	complex amplitude of the received optical signal
A_{LO}	complex amplitude of the continuous-wave local oscillator
$A_{x/y}^{CD}$	linear equalized signal in the x/y polarization components
$A_{x/y}^{EQ}$	totally equalized signal in the x/y polarization components
$A_{x/y}^{NL,(K)}$	nonlinear equalized signal in the x/y polarization components
B_m	equivalent noise bandwidth used for OSNR calculation
BpS	number of bits encoded in each symbol
BER_{M-QAM}	bit error rate for M-QAM constellation
BER_n	bit error rate on the n-th superchannel carrier
BER_{posFEC}	pos-forward error correction bit error rate
BER_{preFEC}	pre-forward error correction bit error rate
BER_{SC}	bit error rate on the entire superchannel
B_r	reference optical bandwidth (typically 0.1 nm)
BW	bandwidth
BW_N	optical noise bandwidth
c	speed of light in vacuum
D	dispersion parameter
E	complex electrical field envelop
E_s	complex electrical field of the received optical signal
E_{LO}	complex electrical field of the continuous-wave local oscillator
$erfc(\cdot)$	complementary error function
f	frequency constant
F	optical amplifier noise
f_0	central frequency of the optical channel
$\mathcal{F}\cdot$	Fourier transform operator
$\mathcal{F}^{-1}\cdot$	inverse Fourier transform operator
G	optical amplifier gain
G_{ASE}	dual-polarization ASE noise power spectral density
G_{NLI}	nonlinear interference power spectral density
G_{NLI}^{corr}	correction term to account for the signal non-Gaussianity effect
G_{NLI}^{EGN}	nonlinear interference power spectral density for the EGN model

G_{SCI}^{EGN}	power spectral density of the self-channel interference
G_{MCI}^{EGN}	power spectral density of the multi-channel interference
G_{XCI}^{EGN}	power spectral density of the cross-channel interference
G_{WDM}	power spectral density that each of the three pumps carry
h	spatial step-size
h_{eff}	effective step-size for digital backpropagation
$h_{xx/xy/yx/yy}$	adaptive equalization algorithm filter taps
h_{RC}	impulse response of the raised-cosine filter
H_{CD}	frequency domain transfer function for CDE
H_{RC}	frequency domain transfer function of the raised-cosine filter
i	imaginary unit
I	signal intensity
$I_{x/y}$	in-phase signal component in the x/y polarization
$I_{I,x/y}$	in-phase photocurrent in the x/y polarization
$I_{Q,x/y}$	quadrature photocurrent in the x/y polarization
K	fiber branch order in VSNE-based DBP techniques
$k_{1/2}$	proportional integrator filter constants
L_{eff}	fiber length
L_{eff}	effective length of the fiber
L_{span}	fiber span length
$M_{1/2}$	number of symbols corresponding to each modulation format
M_n	constellation cardinality of the n-th superchannel carrier
N	number of taps for the FIR filter
N_{FFT}	Fourier transform block-size
n_0	linear refractive index
n_2	nonlinear refractive index
N_k	number of parallel VSNE filters
N_{NL}	number of symbols used for the power-weighted average
N_{RM}	number of real multiplications per sample
N_s	noise power introduced within the B_m
N_{spans}	total number of fiber spans in a link
N_{steps}	number of steps
P	signal power
P_{ASE}	amplified spontaneous emission noise power
P_{B2B}	back-to-back noise power
P_{in}	input power
P_{LO}	power of the continuous-wave local oscillator
P_{NLI}	nonlinear interference noise power
P_{opt}	optimum launched power per superchannel
P_{out}	output power
P_{tx}	average signal power per channel
P_s	power of the received optical signal
$OH_{64QAM/16QAM}$	PM-64QAM/PM-16QAM carrier overhead
OH_{SC}	superchannel overhead

$Q_{x/y}$	quadrature signal component in the x/y polarization
R	responsivity of the photodiode
SNR_{NL}	nonlinear signal-to-noise ratio
SNR_{total}	signal-to-noise ratio accounting for all fiber impairments
R	responsivity
R_c	code rate
R_s	symbol rate
t	time constant
t_n	discrete time instant
T	symbol period
z	spatial coordinate
$(\cdot)^*$	complex conjugate of (\cdot)
α	fiber attenuation coefficient
β_2	group velocity dispersion coefficient
γ	fiber nonlinear coefficient
δ	phase difference between the two polarization modes
Δ_f	channel spacing
$\Delta\omega$	digital frequency resolution
$\varepsilon_{x/y}$	cost function for adaptive equalization in x/y polarization
κ_{QAM}	frame ratio between modulation formats
κ	imaginary constant
$\theta_{mod,x/y}$	phase modulation in the x/y polarization
$\theta_{noise,x/y}$	phase noise in the x/y polarization
θ_s	phase of the received optical signal
θ_{LO}	phase of the continuous-wave local oscillator
λ	carrier wavelength
μ	convergence rate of the adaptive equalization algorithm
ξ	nonlinear digital backpropagation optimization parameter
ρ	roll-off factor of the raised-cosine filter
τ	estimated time delay of the controlled oscillator block
τ_{RM}	latency in number of serial real multiplications
φ	received signal phase noise
χ	nonlinear interference accumulation along the channel
ω	angular frequency
ω_{IF}	intermediate frequency of the baseband signal
ω_s	angular frequency of the received optical signal
ω_{LO}	angular frequency of the continuous-wave local oscillator
ω_n	discrete angular frequency

Chapter 1

Introduction

Internet traffic has been significantly increasing for the last two and a half decades. According to the Cisco visual networking index report, the global Internet Protocol (IP) traffic will continue to increase at a rate of 24% per year until 2021 mainly driven by the progressively increase of cloud computing, mobile data, media streaming, among others [1, 2]. Twenty years ago, global Internet networks carried approximately 100 Gbit of traffic per hour, while in 2016, it reached more than 26,600 Gbit of traffic per second [1]. From Figure 1.1 it can be observed that the global IP traffic is expected to almost triple from 2016 to 2021. The insatiable demand for more bandwidth drove and continues to drive the development of new techniques towards the enabling of the network scalability.

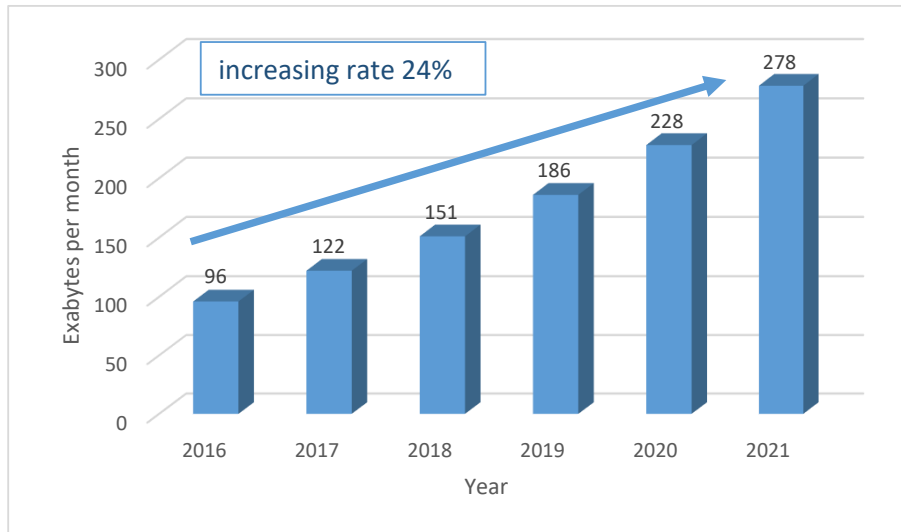


Figure 1.1: Cisco Visual Networking Index traffic forecast from the years 2016 to 2021, in exabytes per month [1].

The recent technological achievements in the optical and electrical domains enabled the adoption of advanced modulation techniques, together with coherent detection and digital signal processing (DSP) for metro and core optical transmission systems. Coherent detection systems offer the possibility to convert to the electrical domain the optical amplitude, phase and polarization of the received signals, enabling the use of DSP

techniques to compensate for the transmitter, optical channel and receiver impairments. This in turn eliminates the need for complex and costly compensation techniques applied in the optical domain, thus avoiding the use of optical components such as dispersion-compensation fibers, optical-polarization controllers and optical-delay lines, as were used previously in direct detection systems [3]. Besides, coherent detection leveraged the adoption of advanced modulation formats based on polarization-multiplexed (PM) and quadrature amplitude modulation (QAM) formats. The use of such modulation formats brings associated a possible increase of the system spectral efficiency (SE), which is defined as the information rate that is being transmitted over a given bandwidth and it is usually measured in bits/s/Hz. Which means that, for the same optical bandwidth, the amount of data being transmitted in each carrier can be increased, or alternatively, for the same information rate, the optical bandwidth can be reduced [4].

High-speed optical transmission systems based on coherent detection and advanced modulation formats have proliferated in the last few years. They proved to be a reliable alternative to the standardized 10G single-channel systems based on simple on-off keying (OOK) modulation formats (1 bit per symbol) and direct detection. PM-quadrature phase-shift keying (QPSK) modulation format (2 bits per symbol and per polarization) was considered by the Optical Internetworking Forum (OIF) the standard for the currently deployed long-haul 100 Gbit/s (100G) systems [2]. The PM-QPSK has a high tolerance to the optical fiber transmission impairments, such as chromatic dispersion (CD), polarization-mode dispersion (PMD), and optical loss, yielding a good balance between fiber capacity and optical reach. Moreover, since it is compatible with the standard 50 GHz ITU-T fixed grid, and therefore with the installed reconfigurable optical add-drop multiplexers (ROADMs) that are based on wavelength selective switch (WSS) technology, the accommodation of PM-QPSK signals dismisses the additional costs associated to the replacement of the existing networks infrastructures [4–6]. For the standard 50 GHz ITU-T fixed grid, the recently proposed PM-QPSK-based 100G systems enables a ten fold improvement of the SE when compared to the standard OOK-based 10G systems (2 bits/s/Hz for PM-QPSK over 0.2 bits/s/Hz for OOK).

Despite the advantages brought by coherent systems, the continuous growth of data traffic has been pushing the currently deployed 100G optical networks to its limits. Telecommunication operators are now looking for new cost-effective transmission paradigms for the next-generation high-speed optical communication systems, that allows the scale of the network capacity without compromising the optical transmission reach [3, 7–9]. Currently, the tradeoff between SE and maximum transmission distance is at the center of the investigation for the next-generation networks.

A simple way to improve SE is by increasing the modulation formats order. However, in such a case, for the same optical power, the constellation points of the higher-order modulation formats become closer to each other, thus negatively affecting the optical signal-to-noise ratio (OSNR) requirements. This, in turn, will reduce the optical transmission distance achievable prior to the regeneration nodes for the same bit-error rate (BER) threshold [10]. Besides, high-order modulation formats are significantly more sensitive to fiber transmission impairments and to narrow optical filtering [2]. On the other hand, for the same modulation format, the SE of the system can be improved by

the use of a higher symbol rate (when considering the same optical grid). However, it will require the use of higher-speed analog-to-digital converters (ADCs) and digital-to-analog converters (DACs), while higher-order modulation formats will require converters with a higher effective number of bits, which in both cases might be hard to achieve due to budget or technological constraints [5].

Different technologies have been proposed seeking for a good compromise between SE and transmission distance. Most recently, optical transmission systems based on superchannels associated with flexible-grid networks have been attracting significant attention due to their capability to increase the SE and adaptability to the traffic demand, while dismissing the replacement of the installed equipments [2, 11–22]. The main idea behind superchannels is the ability to split a high bandwidth optical channel into several smaller bandwidth optical carriers with a small guard-bands between them, which are then propagated through the network as a single optical channel [9, 23, 24].

The superchannel approach allows to relax the required bandwidth of the optical and electrical components due to the use of lower data rates in each optical carrier, presenting an advantage when compared to a single-carrier approach. Moreover, the low data rate optical carriers can be spaced on existing 50 GHz grid channels, enabling its compatibility with existing or future flexible grid wavelength-division multiplexing (WDM) systems [10]. Also, according to the symbol-rate optimization theory presented in [25], superchannel systems are less impacted by nonlinearities than single-carrier systems, bringing an extension of the maximum transmission reach. In the single-carrier transmission systems we have single intra-channel impairments known as self-phase modulation (SPM), while for the case of superchannels we have SPM, cross-phase modulation (XPM) and also some four-wave mixing (FWM) within the superchannel. However, it is likely that the SPM of a single-carrier system is higher than the combination of all sources of nonlinear impairments in the superchannel system. But, it must be pointed out that, in superchannel systems, nonlinearities might be more difficult to compensate, since the cooperation between receivers is required to remove the XPM between carriers. From another point of view, as mentioned above, higher-order modulation formats which require higher OSNR tend to be used, consequently higher signal input power is required, which in turn pushes the transmission system into the nonlinear regime. In addition, the use of smaller guard-bands between superchannel carriers comes at the expense of increased nonlinear inter-carrier interference and consequent degradation of the system performance. Fortunately, the carriers composing the optical superchannel are routed together through the same fiber path, being exposed to the same nonlinear impairments. This opens the possibility to perform multi-carrier mitigation of the nonlinear transmission impairments in the electrical domain.

1.1 Motivation and Objectives

Nonlinear impairments are nowadays the most limiting factor of the SE and reach in optical transmission systems [26]. Along the last decade, the study and development of nonlinear equalization techniques has been a subject of strong scientific interest [27–41]. However, it is well known that the computational complexity of nonlinear equalization

techniques is high, which makes their implementation difficult due to energy and computational power, size and technology constraints. Therefore, the tradeoff between complexity and performance of such techniques is of great importance. Low-complexity nonlinear equalization techniques need to be developed, whose complexity remains suitable for the implementation in application specific integrated circuits (ASICs), while still providing relevant improvements on the system performance [42]. Therefore, while developing digital equalization algorithms, the computational resources associated with them have to be clearly identified. Thereby, the development of metrics that quantifies the computational requirements associated to each algorithm, becomes an important contribution to the research field.

Motivated by the constant need for high performance, spectrally efficient and flexible networks, along this work we propose and evaluate the performance of efficient and low-complexity nonlinear compensation and mitigation techniques to be applied in future high-speed superchannel based long-haul and ultra-long-haul WDM transmission systems. The main objectives of this thesis are:

- Develop and validate low-complexity digital equalization techniques for the compensation of nonlinear transmission impairments;
- Quantify the computational effort associated with the proposed low-complexity techniques and compare them with standard techniques;
- Study and develop advanced techniques for nonlinear mitigation in next-generation superchannels based transmission systems;
- Numerically assess and experimentally validate the proposed nonlinear equalization and mitigation techniques.

1.2 Thesis Outline

This thesis is divided into five main chapters and it is structured as follows. Chapter 2 summarizes the coherent transmitter and receiver architectures and the set of DSP algorithms used in high-speed and long-haul WDM transmission systems. It then contextualizes the recently proposed hybrid modulation formats and superchannel-based coherent optical fiber transmission systems.

The concept of digital backpropagation (DBP) is introduced in Chapter 3, where several low-complexity DBP algorithms are compared with the traditional ones in terms of performance and computational effort. A dual-carrier 400G ultra-long-haul (ULH) WDM optical transmission system based on PM-16QAM carriers is used to experimentally analyze the different DBP algorithms. We also investigate the required DBP step-size, number of real multiplication and latency requirements associated to each of the DBP algorithms.

Given the seek for higher granularity in optical transmission systems, the concept of frequency-hybrid superchannels is studied in Chapter 4, where a 400G frequency-hybrid superchannel solution based on three carriers, two edge PM-16QAM carriers and a central

PM-64QAM carrier, compatible with the 62.5 GHz grid slot is proposed. The optimum power-ratio (PR) between superchannel carriers is evaluated for three different forward error correction (FEC) schemes and it is investigated in linear and nonlinear regimes of operation through the enhanced Gaussian noise (EGN) model, which is validated by experimental and simulation results.

Finally, in Chapter 5 we draw the main conclusions from this work and propose some topics that in our opinion might be interesting for future investigations.

1.3 Main Contributions

In this thesis, we propose techniques for the compensation and mitigation of nonlinear impairments for application in high-speed single-carrier and superchannel based coherent optical fiber transmission systems. The experimental validations of the proposed techniques were possible due to international collaborations made with top-level research institutes equipped with state-of-the-art laboratorial facilities. The author considers that the main contributions of this work can be summarized as follow:

- Experimental demonstration of the parallel SSFM (P-SSFM) for time-domain nonlinear equalization in an ULH 400G optical transmission system. Where for a reach enhancement of 500-800 km over linear equalization, we demonstrate a 5× reduction of the required step-size when compared to the standard split-step Fourier method (SSFM) [J7, C12, C13];
- Experimental assessment of the performance versus complexity of advanced split-step and Volterra-based DBP techniques in an ULH transmission system composed of five dual-carrier PM-16QAM 400G superchannels. The recently proposed weighted VSNE (W-VSNE) provides an improvement of the maximum transmission distance, together with a reduction of the total number of DBP steps required relatively to the widely used SSFM implementation [J7, C12, C13];
- Proposal and experimental evaluation, in a long-haul transmission system, of a 400G frequency-hybrid superchannel solution compatible with the 62.5 GHz grid slot. The optimum power-ratio between superchannel carriers is analytically determined in linear and nonlinear regimes of operation using the EGN model and validated by experimental and simulation results [J10, C18];
- Evaluation of the 400G superchannel performance in terms of maximum reach and optimum launch power when considering distinct FEC paradigms. System performance is also analyzed when nonlinear compensation via DBP techniques is applied, assessing the improvement in maximum reach and their impact on the optimum power-ratio and launch power [J10, C18].

In addition other relevant contributions were achieved as a result of a tight collaboration within Optical Communication research group of Instituto de Telecomunicações. These main other contributions are:

- Development of the low-complexity symmetric Volterra series nonlinear equalizer (symVSNE) and simplified Volterra series nonlinear equalizer (simVSNE) algorithms for frequency-domain nonlinear compensation [J1, C8, C5, C3, C1];
- Development of the low-complexity W-VSNE algorithms for time-domain nonlinear compensation [J2, C7];
- Development and optimization of coherent technologies for future access networks [J9, J6, J4, C14, C6];
- Real-time implementation of DSP algorithms for future access networks [J9, J6, J4, J3, C16, C14, C9, C6, C4];
- Development of a reduced complexity finite impulse response (FIR) filter for time-domain linear compensation [J8, C17, P1];
- Implementation of multi-carrier DBP techniques for superchannel-based optical transmission systems [J5, C15, C11].

1.4 List of Publications

The major achievements resulting from this work were submitted for peer-review by the international scientific community. The published works can be found in the following list of publications:

1.4.1 Papers in international journals

- [J10] **S. B. Amado**, F. P. Guiomar, N. J. Muga, A. Nespola, L. Bertignono, A. Carena and A. N. Pinto, “Nonlinear Mitigation of a 400G Frequency-Hybrid Superchannel for the 62.5 GHz Slot,” *IEEE/OSA Journal of Lightwave Technology*, vol. 35, no. 18, pp. 3963 - 3973, September, 2017.
- [J9] R. Ferreira, A. Shahpari, **S. B. Amado**, M. V. Drummond, J. D. Reis, A. N. Pinto, A. Teixeira, “Optimized carrier frequency and phase recovery based on blind Mth power schemes,” *IEEE Photonics Technology Letters*, vol. 28, no. 21, pp. 2439 - 2442, November, 2016.
- [J8] C. S. Martins, F. P. Guiomar, **S. B. Amado**, R. M. Ferreira, S. Ziaie, A. Shahpari, A. L. Teixeira and A. N. Pinto, “Distributive FIR-Based Chromatic Dispersion Equalization for Coherent Receivers,” *IEEE/OSA Journal of Lightwave Technology*, vol. 34, no. 21, pp. 5023 - 5032, November, 2016.
- [J7] **S. B. Amado**, F. P. Guiomar, N. J. Muga, R. M. Ferreira, J. D. Reis, S. M. Rossi, A. Chiuchiarelli, J. R. F. Oliveira, A. L. Teixeira and A. N. Pinto, “Low Complexity Advanced DBP Techniques for Ultra-Long-Haul 400G Transmission Systems,” *IEEE/OSA Journal of Lightwave Technology*, vol. 34, no. 8, pp. 1793 - 1799, April, 2016. (*invited paper*)

- [J6] A. Shahpari, R. Ferreira, F. P. Guiomar, **S. B. Amado**, S. Ziaie, C. Rodrigues Rodrigues, J.D. Reis, A. N. Pinto, A. Teixeira, “Real-time bidirectional coherent Nyquist UDWDM-PON coexisting with multiple deployed systems in field-trial,” *IEEE/OSA Journal of Lightwave Technology*, vol. 34, no. 7, pp. 1643 - 1650, April, 2016. (*invited paper*)
- [J5] F. P. Guiomar, **S. B. Amado**, J. D. Reis, S. M. Rossi, A. Chiuchiarelli, J. R. F. Oliveira, A. L. Teixeira and A. N. Pinto, “Multi-Carrier Digital Backpropagation for 400G Optical Superchannels,” *IEEE/OSA Journal of Lightwave Technology*, vol. 34, no. 8, pp. 1896 - 1907, April, 2016. (*invited paper*)
- [J4] R. M. Ferreira, J. D. Reis, S. M. Rossi, **S. B. Amado**, F. P. Guiomar, Ali Shahpari, J. R. F. Oliveira, A. N. Pinto and A. L. Teixeira, “Coherent Nyquist UDWDM-PON with Digital Signal Processing in Real-Time,” *IEEE/OSA Journal of Lightwave Technology*, vol. 34, no. 2, pp. 826-833, January, 2016. (*invited paper*)
- [J3] R. M. Ferreira, J. D. Reis, **S. B. Amado**, A. Shahpari, F. P. Guiomar, J. R. F. Oliveira, A. N. Pinto and A. L. Teixeira, “Performance and Complexity of Digital Clock Recovery for Nyquist UDWDM-PON in Real-Time,” *IEEE Photonics Technology Letters*, vol. 27, no. 21, pp. 2230-2233, November, 2015.
- [J2] F. P. Guiomar, **S. B. Amado**, C. S. Martins and A. N. Pinto, “Time Domain Volterra-Based Digital Backpropagation for Coherent Optical Systems,” *IEEE/OSA Journal of Lightwave Technology*, vol. 15, no. 33, pp. 3170-3181, 2015.
- [J1] F. P. Guiomar, **S. B. Amado**, A. Carena, G. Bosco, A. Nespola, A. L. Teixeira and A. N. Pinto, “Fully-Blind Linear and Nonlinear Equalization for 100G PM-64QAM Optical Systems,” *IEEE/OSA Journal of Lightwave Technology*, vol. 33, no. 7, pp. 1265-1274, 2015. (*invited paper*)

1.4.2 Papers in conference proceedings

- [C18] **S. B. Amado**, F. P. Guiomar, N. J. Muga, A. Nespola, L. Bertignono, A. Carena and A. N. Pinto, “400G Frequency-Hybrid Superchannel for the 62.5 GHz Slot,” in *Proc. Optical Fiber Communication Conference (OFC)*, paper Th4D.4, Los Angeles, California, USA, March, 2017.
- [C17] C. S. Martins, **S. B. Amado**, S. M. Rossi, A. Chiuchiarelli, J. D. Reis, A. Carena, F. P. Guiomar and A. N. Pinto, “Low-Complexity Chromatic Dispersion Equalizer for 400G Transmission Systems,” in *Proc. Optical Fiber Communication Conference (OFC)*, paper Th2A.56, Los Angeles, California, USA, March, 2017.
- [C16] R. Ferreira, A. Shahpari, **S. B. Amado**, J.D. Reis, A. N. Pinto, A. Teixeira, “Real-Time Flexible Heterogeneous UDWDM System for Coherent PON,” in *Proc. 42nd European Conf. on Optical Communications (ECOC)*, Dusseldorf, Germany, pp. 1 - 3, September, 2016.

- [C15] A. N. Pinto, **S. B. Amado**, C. S. Martins, S. Ziaie, N. J. Muga and F. P. Guiomar, “Multi-carrier high-speed optical communication systems supported by digital signal processing,” in *Proc. 18th International Conference on Transparent Optical Networks (ICTON)*, Trento, 2016, pp. 1-4.
- [C14] R. Ferreira, A. Shahpari, F. Guiomar, **S. B. Amado**, M. Drummond, J. D. Reis, A. Pinto, and A. L. Teixeira, “Hardware Optimization for Carrier Recovery based on Mth Power Schemes,” in *Proc. Optical Fiber Communication Conference (OFC)*, paper Th2A.43, Anaheim, California, USA, March, 2016.
- [C13] **S. B. Amado**, F. P. Guiomar, N. J. Muga, J. D. Reis, S. M. Rossi, A. Chiuchiarelli, J. R. F. Oliveira, A. L. Teixeira and A. N. Pinto, “Experimental Demonstration of the Parallel Split-Step Method in Ultra-Long-Haul 400G Transmission,” in *Proc. 41st European Conf. Optical Communication (ECOC)*, paper Th.2.6.2, Valencia, Spain, September, 2015.
- [C12] **S. B. Amado**, F. P. Guiomar, N. J. Muga, J. D. Reis, S. M. Rossi, A. Chiuchiarelli, J. R. F. Oliveira, A. L. Teixeira and A. N. Pinto, “Experimental Demonstration of the Weighted Volterra Series Nonlinear Equalizer,” in *Proc. 10th Conference on Telecommunications (ConfTele)*, Aveiro, Portugal, September, 2015.
- [C11] F. P. Guiomar, **S. B. Amado**, J. D. Reis, S. M. Rossi, A. Chiuchiarelli, J. R. F. Oliveira, A. L. Teixeira and A. N. Pinto, “Ultra-Long-Haul 400G Superchannel Transmission with Multi-Carrier Nonlinear Equalization,” in *Proc. 41st European Conf. Optical Communication (ECOC)*, paper Th.2.2.4, Valencia, Spain, September, 2015.
- [C10] **S. B. Amado**, F. P. Guiomar, N. J. Muga and A. N. Pinto, “Assessment of Nonlinear Equalization Algorithms for Coherent Optical Transmission Systems using an FPGA,” in *Proc. International Conference on Transparent Optical Networks (ICTON)*, paper Mo.C1.4, Budapest, Hungary, July, 2015.
- [C9] A. N. Pinto, **S. B. Amado**, C. S. Martins, S. Ziaie, N. Muga, R. Ferreira, A. L. Teixeira and F. P. Guiomar, “Real-Time Digital Signal Processing for Coherent Optical Systems,” in *Proc. International Conference on Transparent Optical Networks (ICTON)*, paper Mo.C1.2 Budapest, Hungary, June, 2015.
- [C8] F. P. Guiomar, **S. B. Amado**, C. S. Martins, J. D. Reis, A. L. Teixeira and A. N. Pinto, “Volterra-based Digital Backpropagation: Performance and Complexity Assessment,” in *Proc. Advanced Photonics for Communications*, Boston, USA, June 2015. (*invited paper*)
- [C7] F. P. Guiomar, **S. B. Amado**, C. S. Martins and A. N. Pinto, “Parallel Split-Step Method for Digital Backpropagation,” in *Proc. Optical Fiber Communication Conference (OFC)*, paper Th2A.28, Los Angeles, USA, March 2015.

- [C6] R. M. Ferreira, J. D. Reis, S. M. Rossi, **S. B. Amado**, A. Shahpari, N. G. Gonzalez, J. R. F. Oliveira, A. N. Pinto and A. L. Teixeira, “Demonstration of Nyquist UDWDM-PON with Digital Signal Processing in Real-Time,” in *Proc. Optical Fiber Communication Conference (OFC)*, paper Th3I.4, Los Angeles, USA, March 2015.
- [C5] F. P. Guiomar, **S. B. Amado**, A. Carena, G. Bosco, A. Nespola and A. N. Pinto, “Transmission of PM-64QAM over 1524 km of PSCF using Fully-Blind Equalization and Volterra-Based Nonlinear Mitigation,” in *Proc. 40th European Conf. Optical Communication (ECOC)*, paper We.3.3.3, Cannes, France, September, 2014.
- [C4] R. Ferreira, A. Shahpari, **S. B. Amado**, P. Costa, J. D. Reis, F. P. Guiomar, A. N. Pinto and A. L. Teixeira, “Impact of TWDM on Optional Real-Time QPSK WDM Channels,” in *Proc. 40th European Conf. Optical Communication (ECOC)*, paper P.7.19, Cannes, France, September 2014.
- [C3] A. N. Pinto, F. P. Guiomar, **S. B. Amado**, S. Ziaie, A. Shahpari, R. Ferreira, N. Muga and A. L. Teixeira, “Digital Equalization of Optical Nonlinearities in Very High-Speed Optical Communication Systems,” in *Proc. 16th International Conference on Transparent Optical Networks (ICTON)*, invited talk, Graz, Austria, July 2014. (*invited paper*)
- [C2] **S. B. Amado**, F. P. Guiomar and A. N. Pinto, “Clock and Carrier Recovery in High-Speed Coherent Optical Communication Systems,” in *Proc. II International Conference on Applications of Optics and Photonics*, Aveiro, Portugal, May 2014.
- [C1] F. P. Guiomar, **S. B. Amado** and A. N. Pinto, “Reducing the Complexity of Digital Nonlinear Compensation for High-Speed Coherent Optical Communication Systems,” in *Proc. II International Conference on Applications of Optics and Photonics*, Aveiro, Portugal, May 2014.

1.4.3 Patents

- [P1] A. N. Pinto, F. P. Guiomar, **S. B. Amado**, C. S. Sanches, “Filtro Digital de Baixa Complexidade para a Compensação da Dispersão Cromática no Domínio do Tempo,” 20151000062379, July, 2015.

References

- [1] “Cisco visual networking index: Forecast and methodology, 2016-2021,” Cisco Systems, Tech. Rep., 2017.
- [2] J. D. Reis, V. Shukla, D. R. Stauffer, and K. Glass, “Technology options for 400G implementation,” Optical Internetworking Forum, Tech. Rep., 2015.
- [3] “Coherent WDM technologies,” Infinera, Tech. Rep., 2016.

-
- [4] K. Kikuchi, “Fundamentals of coherent optical fiber communications,” *Journal of Lightwave Technology*, vol. 34, no. 1, pp. 157–179, Jan 2016.
 - [5] G. Bennett, “Super-channels DWDM transmission at 100Gb/s and beyond,” Infinera, Tech. Rep., 2012.
 - [6] S. Perrin, “Moving to 100G & beyond,” ZTE, Tech. Rep., 2012.
 - [7] X. Zhou and L. E. Nelson, “400G WDM transmission on the 50 GHz grid for future optical networks,” *J. Lightw. Technol.*, vol. 30, no. 24, pp. 3779–3792, 2012.
 - [8] X. Zhou, L. Nelson, R. Issac, P. Magill, B. Zhu, and D. Peckham, “1200 km transmission of 50 GHz spaced, 5×504 Gb/s PDM-32-64 hybrid QAM using electrical and optical spectral shaping,” in *Proc. Optical Fiber Communication Conf. and Exposition (OFC)*, paper OM2A.2, 2012.
 - [9] A. Amari, O. A. Dobre, R. Venkatesan, O. S. S. Kumar, P. Ciblat, and Y. Jaoun, “A survey on fiber nonlinearity compensation for 400 Gbps and beyond optical communication systems,” *IEEE Communications Surveys Tutorials*, vol. PP, no. 99, pp. 1–1, 2017.
 - [10] “Beyond 100G,” Fujitsu Network Communications inc., Tech. Rep., 2012.
 - [11] G. Bosco, P. Poggiolini, A. Carena, V. Curri, and F. Forghieri, “Analytical results on channel capacity in uncompensated optical links with coherent detection,” *Opt. Express*, vol. 19, no. 26, pp. B440–B451, Dec 2011.
 - [12] G. Bosco, V. Curri, A. Carena, P. Poggiolini, and F. Forghieri, “On the performance of Nyquist-WDM Terabit superchannels based on PM-BPSK, PM-QPSK, PM-8QAM or PM-16QAM subcarriers,” *J. Lightw. Technol.*, vol. 29, no. 1, pp. 53–61, Jan 2011.
 - [13] T. Zeng, “Superchannel transmission system based on multi-channel equalization,” *Opt. Express*, vol. 21, no. 12, pp. 14 799–14 807, Jun 2013.
 - [14] C. Liu, J. Pan, T. Detwiler, A. Stark, Y.-T. Hsueh, G.-K. Chang, and S. E. Ralph, “Joint digital signal processing for superchannel coherent optical communication systems,” *Opt. Express*, vol. 21, no. 7, pp. 8342–8356, Apr 2013.
 - [15] D. Rafique, T. Rahman, A. Napoli, M. Kuschnerov, G. Lehmann, and B. Spinnler, “Flex-grid optical networks: spectrum allocation and nonlinear dynamics of super-channels,” *Opt. Express*, vol. 21, no. 26, pp. 32 184–32 191, Dec 2013.
 - [16] D. Rafique, T. Rahman, A. Napoli, S. Calabro, and B. Spinnler, “Technology options for 400 Gb/s PM-16QAM flex-grid network upgrades,” *Photonics Technology Letters, IEEE*, vol. 26, no. 8, pp. 773–776, April 2014.

- [17] J.-X. Cai, H. G. Batshon, H. Zhang, M. Mazurczyk, O. Sinkin, D. G. Foursa, A. Pilipetskii, G. Mohs, and N. S. Bergano, "30.4 Tb/s transmission over transpacific distance using 200 Gb/s and dual wavelength 400 Gb/s 16QAM at 6.0 b/s/Hz spectral efficiency," *Opt. Express*, vol. 22, no. 8, pp. 9116–9122, Apr 2014.
- [18] D. Rafique, "Fiber nonlinearity compensation: Commercial applications and complexity analysis," *Lightwave Technology, Journal of*, vol. PP, no. 99, pp. 1–1, 2015.
- [19] R. Maher, T. Xu, L. Galdino, M. Sato, A. Alvarado, K. Shi, S. J. Savory, B. C. Thomsen, R. I. Killey, and P. Bayvel, "Spectrally shaped DP-16QAM super-channel transmission with multi-channel digital back-propagation," *Scientific Reports*, vol. 5, no. 8214, February 2015.
- [20] Z. Jia, H. C. Chien, J. Zhang, Y. Cai, and J. Yu, "Performance comparison of dual-carrier 400G with 8/16/32-QAM modulation formats," *IEEE Photonics Technology Letters*, vol. 27, no. 13, pp. 1414–1417, July 2015.
- [21] T. Rahman, D. Rafique, A. Napoli, E. de Man, B. Spinnler, M. Bohn, C. M. Okonkwo, A. M. J. Koonen, and H. de Waardt, "Ultralong haul 1.28 Tb/s PM-16QAM WDM transmission employing hybrid amplification," *J. Lightwave Technol.*, vol. 33, no. 9, pp. 1794–1804, May 2015.
- [22] A. Napoli, M. Bohn, D. Rafique, A. Stavdas, N. Sambo, L. Poti, M. Nlle, J. K. Fischer, E. Riccardi, A. Pagano, A. D. Giglio, M. S. Moreolo, J. M. Fabrega, E. Hugues-Salas, G. Zervas, D. Simeonidou, P. Layec, A. D'Errico, T. Rahman, and J. P. F. P. Gimnez, "Next generation elastic optical networks: The vision of the european research project IDEALIST," *IEEE Communications Magazine*, vol. 53, no. 2, pp. 152–162, Feb 2015.
- [23] "The next generation of coherent optical," Infinera, Tech. Rep., 2016.
- [24] N. Fontaine, X. Liu, S. Chandrasekhar, R. Ryf, S. Randel, P. Winzer, R. Delbue, P. Pupalakis, and A. Sureka, "Fiber nonlinearity compensation by digital backpropagation of an entire 1.2 Tb/s superchannel using a full-field spectrally-sliced receiver," in *Optical Communication (ECOC 2013), 39th European Conference and Exhibition on*, Sept 2013, pp. 1–3.
- [25] P. Poggiolini, A. Nespola, Y. Jiang, G. Bosco, A. Carena, L. Bertignono, S. M. Bilal, S. Abrate, and F. Forghieri, "Analytical and experimental results on system maximum reach increase through symbol rate optimization," *Journal of Lightwave Technology*, vol. 34, no. 8, pp. 1872–1885, April 2016.
- [26] R.-J. Essiambre, G. Kramer, P. J. Winzer, G. J. Foschini, and B. Goebel, "Capacity limits of optical fiber networks," *J. Lightw. Technol.*, vol. 28, no. 4, pp. 662–701, 2010.

-
- [27] E. Ip and J. M. Kahn, "Compensation of dispersion and nonlinear impairments using digital backpropagation," *J. Lightw. Technol.*, vol. 26, no. 20, pp. 3416–3425, 2008.
- [28] X. Li, X. Chen, G. Goldfarb, E. Mateo, I. Kim, F. Yaman, and G. Li, "Electronic post-compensation of WDM transmission impairments using coherent detection and digital signal processing," *Opt. Express*, vol. 16, no. 2, pp. 880–888, Jan 2008.
- [29] D. S. Millar, S. Makovejs, C. Behrens, S. Hellerbrand, R. I. Killey, P. Bayvel, and S. J. Savory, "Mitigation of fiber nonlinearity using a digital coherent receiver," *IEEE J. Sel. Topics Quantum Electron.*, vol. 16, no. 5, pp. 1217–1226, 2010.
- [30] E. Ip, "Nonlinear compensation using backpropagation for polarization-multiplexed transmission," *J. Lightw. Technol.*, vol. 28, no. 6, pp. 939–951, 2010.
- [31] S. J. Savory, G. Gavioli, E. Torrenco, and P. Poggiolini, "Impact of interchannel nonlinearities on a split-step intrachannel nonlinear equalizer," *IEEE Photon. Technol. Lett.*, vol. 22, no. 10, pp. 673–675, 2010.
- [32] G. Goldfarb, M. G. Taylor, and G. Li, "Experimental demonstration of fiber impairment compensation using the split-step finite-impulse-response filtering method," *IEEE Photon. Technol. Lett.*, vol. 20, no. 22, pp. 1887–1889, 2008.
- [33] F. P. Guiomar, J. D. Reis, A. L. Teixeira, and A. N. Pinto, "Digital postcompensation using Volterra series transfer function," *IEEE Photon. Technol. Lett.*, vol. 23, no. 19, pp. 1412–1414, 2011.
- [34] —, "Mitigation of intra-channel nonlinearities using a frequency-domain Volterra series equalizer," *Opt. Express*, vol. 20, no. 2, pp. 1360–1369, Jan 2012.
- [35] F. P. Guiomar, J. D. Reis, A. Carena, G. Bosco, A. L. Teixeira, and A. N. Pinto, "Experimental demonstration of a frequency-domain Volterra series nonlinear equalizer in polarization-multiplexed transmission," *Opt. Express*, vol. 21, no. 1, pp. 276–288, 2013.
- [36] F. P. Guiomar and A. N. Pinto, "Simplified Volterra series nonlinear equalizer for polarization-multiplexed coherent optical systems," *J. Lightw. Technol.*, vol. 31, no. 23, pp. 3879–3891, 2013.
- [37] G. Shulkind and M. Nazarathy, "Nonlinear digital back propagation compensator for coherent optical OFDM based on factorizing the Volterra series transfer function," *Opt. Express*, vol. 21, no. 11, pp. 13 145–13 161, Jun 2013.
- [38] E. Giacomidis, I. Aldaya, M. Jarajreh, A. Tsokanos, S. T. Le, F. Farjady, Y. Jaouen, A. Ellis, and N. Doran, "Volterra-based reconfigurable nonlinear equalizer for coherent OFDM," *IEEE Photon. Technol. Lett.*, vol. 26, no. 14, pp. 1383–1386, July 2014.
-

- [39] F. P. Guiomar, S. B. Amado, and A. N. Pinto, “Reducing the complexity of digital nonlinear compensation for high-speed coherent optical communication systems,” in *Proc. SPIE, Second International Conference on Applications of Optics and Photonics*, vol. 9286, 2014, pp. 92 864L–92 864L–9.
- [40] F. Guiomar, S. Amado, A. Carena, G. Bosco, A. Nespola, A. Teixeira, and A. Pinto, “Fully-blind linear and nonlinear equalization for 100G PM-64QAM optical systems,” *J. Lightw. Technol.*, vol. PP, no. 99, 2015.
- [41] F. P. Guiomar, S. B. Amado, C. S. Martins, and A. N. Pinto, “Time domain Volterra-based digital backpropagation for coherent optical systems,” *J. Lightw. Technol.*, vol. 15, no. 33, pp. 3170–3181, August 2015.
- [42] V. Parahyba, J. Reis, S. Ranzini, E. Schneider, E. Rosa, F. Simões, J. Diniz, L. Carvalho, E. Filho, J. Oliveira, and J. Oliveira, “Performance against implementation of digital backpropagation for high-speed coherent optical systems,” *Electronics Letters*, vol. 51, no. 14, pp. 1094–1096, 2015.

Chapter 2

Coherent Transmission Systems

Optical fibers proved to be the most cost-effective medium to transmit high-speed signals over long-haul terrestrial and transoceanic distances [1]. Their low cost, low attenuation and high bandwidth made optical fibers the preferable transmission system for today's demanding networks. However, the fast average growth of data traffic in the last two decades, 25% per year according to the latest Cisco report, is leveraging the introduction of several innovative technologies that aim to increase even more the bit rate-reach product of existing optical transmission systems [1, 2]. Advanced modulation formats enabled by coherent transmission systems are the two new paradigms in the optical communications field [3]. Today's long-haul optical transmission systems allow the transmission of 100 Gbit/s and 200 Gbit/s channels. The next generation of long-haul WDM transmission systems is expected to operate at rates between 400 Gbit/s (400G) and 1 Tbit/s (1T) per channel. Such transmission rates are achieved with the increase of spectral efficiency (SE), enabled by the use of higher-order modulation formats together with the possible use of higher symbol rates when keeping the same channel spacing or reduced channel spacing for the same symbol rate. For the last couple of years, hybrid modulation formats have been seen as a way to improve the SE of superchannels-based optical transmission systems, by finding a better fit of the delivered bit-rate to the allocated spectral slot. Although single-carrier systems seem to have the lowest cost per bit, superchannels approaches have gained attention since they allow us to overcome the limitations associated to high-speed optoelectronics components required by single-carrier systems. On the other hand, the use of hybrid modulation formats allow us to increase the SE granularity over standard M-ary QAM formats.

In this chapter, we start by introducing the fundamentals of coherent optical transmission systems, section 2.1. Typical post-detection digital signal processing (DSP) algorithms used in high-speed optical transmission systems are then described in section 2.2. After that, we discuss some technology innovations that have been proposed for the next-generation of long-haul WDM transmission systems and which are relevant for our work. Higher-order modulation formats are firstly proposed as a way to increase system SE, in section 2.3. Then, hybrid modulation format techniques which, lately, have been largely used are presented in section 2.4. Section 2.5 introduces the concept of superchannels together with some of the relevant works that have been published. Finally, the main conclusions of this chapter are summarized in section 3.7.

2.1 Digital Coherent Optical System

The first interest in coherent optical fiber transmission systems emerged in the early 80's. At that time, the higher sensitivity of the coherent receivers when compared to direct detection receivers was the main motivation behind the study of such systems that promised an increase of the maximum achievable transmission distance [4]. However, the studies on coherent detection were put aside with the emergence of optical amplification based on erbium-doped fiber amplifier (EDFA), which allowed the direct detection systems to achieve the same reach of coherent systems with less complexity. Furthermore, high capacity WDM systems based on intensity modulation and direct detection systems start to be explored as another way to increase transmission capacity of a single fiber. By 1990s, these two new technologies brought a thousand fold increase in the capacity of optical transmission systems [5], therefore there were no need to focus on coherent transmission systems any longer at that time.

Nowadays, increasingly demanding networks are pushing the need for higher capacity and spectral efficiency (SE) transmission systems. This together with the emergence of higher-speed analog-to-digital converters (ADCs), digital-to-analog converters (DACs) and integrated circuits led to the recent revival of coherent detection systems. The introduction of coherent detection in optical transmission systems allows the use of any kind of modulation format. Moreover, pre- and/or post-DSP techniques can be added to the system, enabling the equalization of the system transmission impairments in the digital domain. Which in turn makes the implementation of the optical networks more flexible and avoids the use of additional complex higher cost optical components [6, 7].

In the following subsections, the fundamentals of coherent optical fiber transmission systems are reviewed. We describe the architecture of the DSP based coherent optical transmitter and receiver.

2.1.1 Coherent receiver

Polarization-diversity coherent receivers are widely used in current ultra-long-haul (ULH) optical transmission systems. By using both polarizations of the optical signal we transmit two times more information in the same optical bandwidth, therefore doubling the SE. The configuration of a coherent receiver employing polarization and phase diversity is schematized in Figure 2.1, where two phase-diversity coherent receivers are combined in a polarization-diversity configuration. This configuration allows us to recover the in-phase and quadrature components of both X and Y polarizations.

The complex electrical field of the received optical signal is given by¹

$$E_s(t) = A_s(t) \exp \left(-i(\omega_s t + \theta_s(t)) \right), \quad (2.1)$$

where $A_s(t)$ is the complex amplitude of the received optical signal, ω_s is the angular frequency and $\theta_s(t)$ is the phase of the received signal. In addition, a continuous-wave

¹The Fourier transform adopted in this thesis is in accordance with the physicists convention, as used in [8] to derive the scalar nonlinear Schrödinger equation (NLSE). Going from physicists convention to the electrical engineering convention is easily achieved by substituting $i = -j$ into the scalar NLSE.

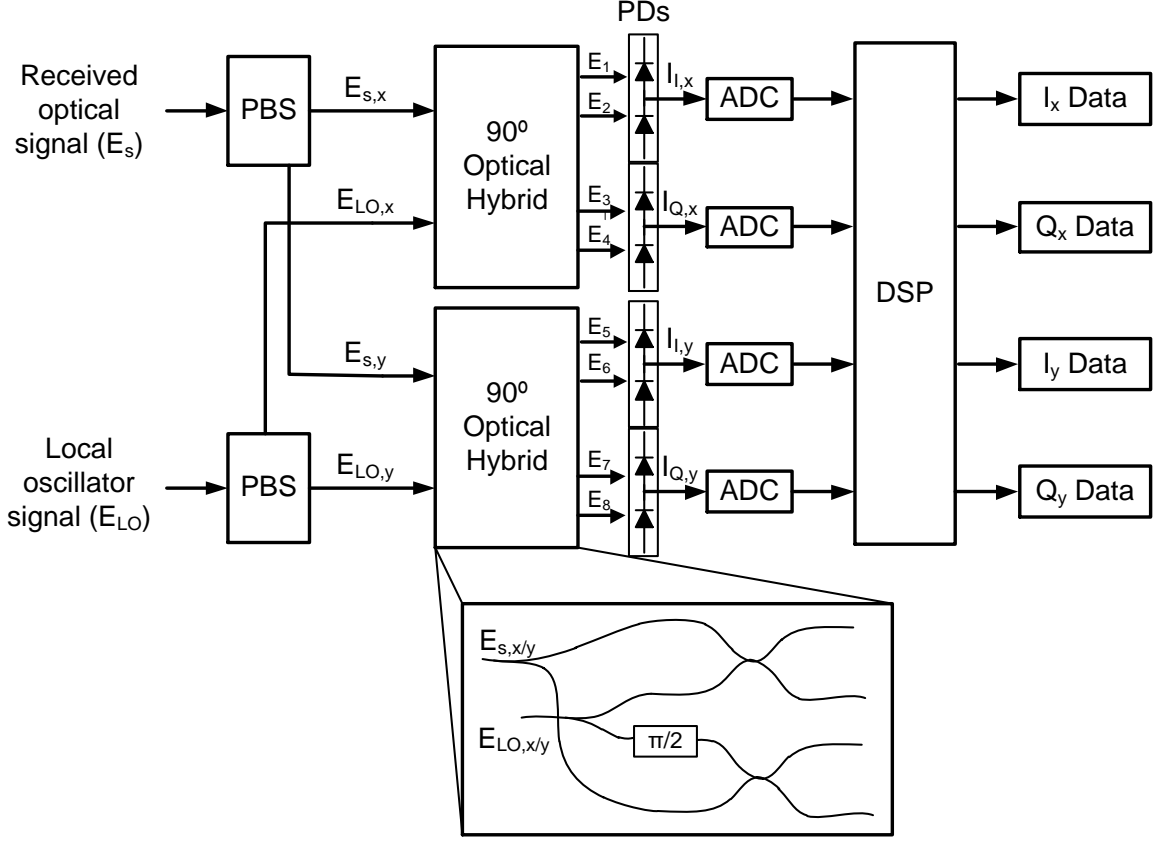


Figure 2.1: Configuration of the coherent receiver employing phase and polarization diversity. PBS: Polarization beam splitter; ADC: Analog-to-digital converter; PDs: Photodiodes.

local oscillator (LO) is needed in order to convert to the baseband the electrical field of the received optical signal. The complex electrical field of the continuous-wave LO is given by

$$E_{LO}(t) = A_{LO}(t) \exp \left(-i(\omega_{LO}t + \theta_{LO}(t)) \right), \quad (2.2)$$

where $A_{LO}(t)$ is the complex amplitude of the continuous-wave LO, ω_{LO} and $\theta_{LO}(t)$ are the angular frequency and the phase of the LO signal, respectively. Note that the LO frequency is adjusted to the frequency of the received signal in order to perform intradyne detection, which means that the signal is converted to a near zero frequency.

The received optical signal and the continuous-wave LO are firstly separated into its two orthogonal polarization signals by a polarization beam splitter (PBS). These two signals, $E_{s,x}$ and $E_{s,y}$ are then mixed with the free-running continuous-wave LO, $E_{LO,x}$ and $E_{LO,y}$, into two 2×4 90° optical hybrids. In the 90° optical hybrid the LO signal is divided in two path with a 90° phase shift between them, see the inset in Figure 2.1. By coupling the two paths with the received signal, the in-phase and quadrature components can be simultaneously retrieved. The optical fields of the two 90° optical hybrids outputs are given by [5]

$$E_{1/5} = \frac{1}{2}(E_{s,x/y} + E_{LO,x/y}), \quad (2.3)$$

$$E_{2/6} = \frac{1}{2}(E_{s,x/y} - E_{LO,x/y}), \quad (2.4)$$

$$E_{3/7} = \frac{1}{2}(E_{s,x/y} - iE_{LO,x/y}), \quad (2.5)$$

$$E_{4/8} = \frac{1}{2}(E_{s,x/y} + iE_{LO,x/y}). \quad (2.6)$$

The outputs of the optical hybrid are then incident into a pair of balanced photodiodes that perform opto-electrical conversion, yielding the in-phase and quadrature photocurrents:

$$I_{I,x/y}(t) = R\sqrt{P_{s,x/y}(t)P_{LO,x/y}} \cos [\omega_{IF} + \theta_{s,x/y}(t) - \theta_{LO,x/y}(t)], \quad (2.7)$$

$$I_{Q,x/y}(t) = R\sqrt{P_{s,x/y}(t)P_{LO,x/y}} \sin [\omega_{IF} + \theta_{s,x/y}(t) - \theta_{LO,x/y}(t)]. \quad (2.8)$$

In the above equations, R corresponds to the responsivity of the photodiode, $\omega_{IF} = |\omega_s - \omega_{LO}|$ is the intermediate frequency of the baseband signal obtained after the beating between the received signal and the LO. P_s and P_{LO} are the received signal and the LO powers, respectively. The output signal phase may present some time varying phase noise, therefore

$$\theta_{s,x/y}(t) - \theta_{LO,x/y}(t) = \theta_{mod,x/y}(t) + \theta_{noise,x/y}(t), \quad (2.9)$$

where $\theta_{mod,x/y}$ is the phase modulation and $\theta_{noise,x/y}$ is the phase noise. Note that balanced detection is used in order to suppress the DC component and maximize the beating between the received and the LO signals.

These signals are then sampled by an ADC, that is typically composed of four integrated ADC channels, sampling in parallel the in-phase and quadrature components of both X and Y polarizations. According to the sampling theorem, the sampling rate must be twice as high as the maximum frequency of the signal, in order to avoid the aliasing effect. Therefore, ADCs sampling at twice the symbol rate are typically used. However, it is possible to use a fractional sampling rate of pR_s , as far as the signal bandwidth is $BW = p/T$, where $1 < p < 2$, while avoiding the aliasing effect. In this case, a posterior digital resampling of the signal will be necessary in order to satisfy the two-times oversampling condition necessary for the adaptive equalizer block [5]. The digitalized samples are then fed to the offline or real-time DSP subsystems, which are applied to undo the transmitter, receiver and optical fiber impairments. Given that post-detection DSP is a relevant topic in our work, the set of DSP algorithms typically used in high-speed ULH transmission systems are analyzed in section 2.2.

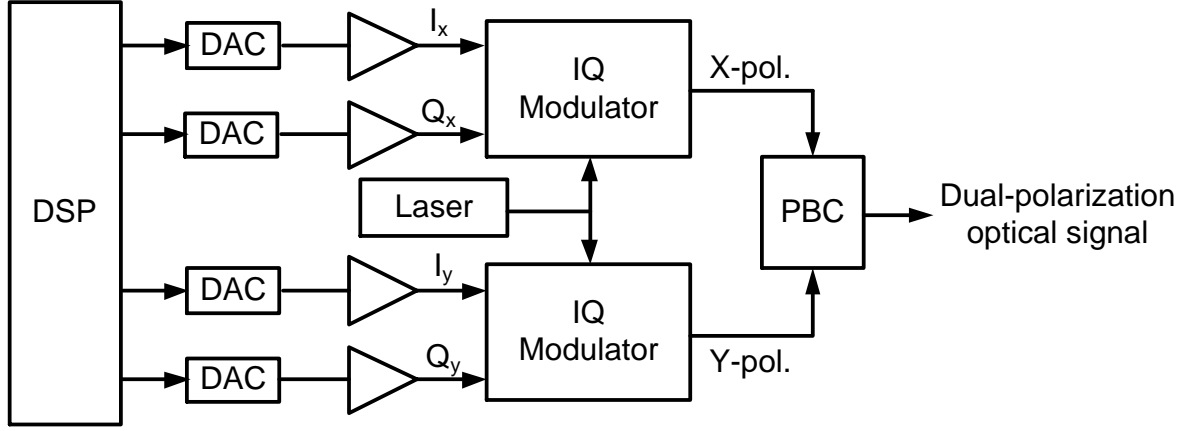


Figure 2.2: Configuration of the a dual-polarization in-phase and quadrature optical modulator. PBC: Polarization beam combiner; DAC: Digital-to-analog converter

2.1.2 Coherent transmitter

The introduction of coherent receivers brought the capability to demodulate higher-order modulation formats. The basic architecture of a coherent transmitter is schematized in Figure 2.2, where both in-phase and quadrature components of two signals with orthogonal states of polarization, X and Y, are modulated.

The bitstream to be transmitted is initially mapped into an M-QAM constellation. Pre-DSP techniques can then be applied for pulse shaping or for pre-distortion and/or compensation of the transmitted signal. Pulse shaping is normally applied to limit the signal bandwidth and control the inter-symbol interference (ISI) caused by the channel. On the other hand, digital pre-emphasis is commonly used to mitigate for the penalties due to transmitter or receiver electrical components limitations. Additionally, FEC coding might also be applied to add redundancy to the signal and consequently reduce the amount of bit errors after recovery at the receiver side.

One kind of pulse shaping that is commonly used in communication systems is the *sinc* shaped filter. Figure 2.3 shows a time-domain waveform of two adjacent *sinc* pulses. From this figure it can be observed that in *sinc* pulses its value is zero for all the sampling instants $t = kT$, except for $k = 0$, where T is the symbol period, $T = 1/R_s$ with R_s being the symbol rate. Besides, its amplitude decays slowly with the time, ($\approx 1/|t|$), which is better from the sampling jitter point of view but is worst when the sampling instant is imperfect, due to the significant ISI arising [9]. On the other hand, its frequency-domain equivalent has a rectangular shape, which is difficult to implement in practical systems, due to the required infinite number of taps.

As an alternative, Nyquist filters with raised-cosine pulse shaping are nowadays typically applied to the symbol stream, since they are practical to implement. Its frequency-domain description is given by

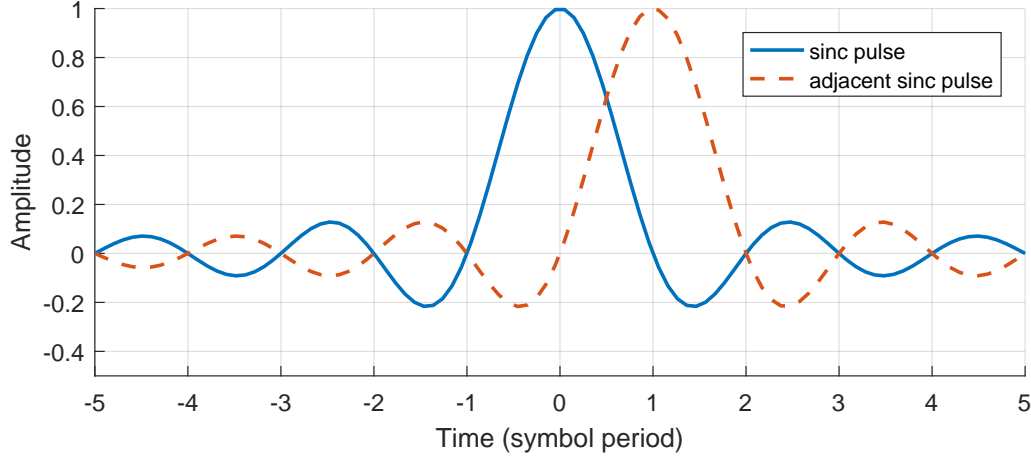


Figure 2.3: Time-domain waveform of two adjacent *sinc* pulse shaping filters.

$$H_{RC}(f) = \begin{cases} 1, & 0 \leq |f| \leq \frac{1-\rho}{2T} \\ \frac{1}{2} \left[1 + \cos \left[\frac{\pi T}{\rho} \left(f - \frac{1-\rho}{2T} \right) \right] \right], & \frac{1-\rho}{2T} \leq |f| \leq \frac{1+\rho}{2T} \\ 0, & \text{otherwise} \end{cases} \quad (2.10)$$

where $0 \leq \rho \leq 1$ is the *roll-off* factor of the raised-cosine filter, with the corresponding impulse response being given by

$$h_{RC}(t) = \begin{cases} \frac{\pi}{4T} \text{sinc}\left(\frac{1}{2\rho}\right), & t = \pm \frac{T}{2\rho} \\ \frac{1}{T} \text{sinc}\left(\frac{t}{T}\right) \frac{\cos\left(\frac{\pi \rho t}{T}\right)}{1 - \left(\frac{2\rho t}{T}\right)^2}, & \text{otherwise} \end{cases} \quad (2.11)$$

Again in this case $h_{RC}(kT) = 0$ for $k \neq 0$, therefore there is no ISI. However in this case, the pulse decay is much faster ($\approx 1/|t|^3$), therefore when the sampling is imperfect the ISI becomes much smaller. The main drawback is that the raised-cosine pulse shaping spectrum has a larger bandwidth than the one of *sinc* pulse shaping. The bandwidth of a raised-cosine filter is defined given by $BW = R_s(\rho + 1)$. Note that by selecting $\rho = 0$ one get the *sinc* pulse.

The digital sequence of samples is then resampled to match the DAC sampling rate and sampled by the DACs. The analog output samples are then fed into the drivers that will condition the signals for driving the in-phase and quadrature modulators (IQMs).

The configuration typically used for the implementation of an IQM is depicted in the Figure 2.4. A laser source is split using a 3 dB polarization maintaining splitter and each output is modulated independently with a Mach-Zehnder modulator (MZM) in a push-pull configuration. The I and Q modulating electrical signals drive the two parallel MZMs, with an optical phase shift of $\pi/2$ between them, achieving in-phase and quadrature modulation after coupling the two branches, Figure 2.4 [5].

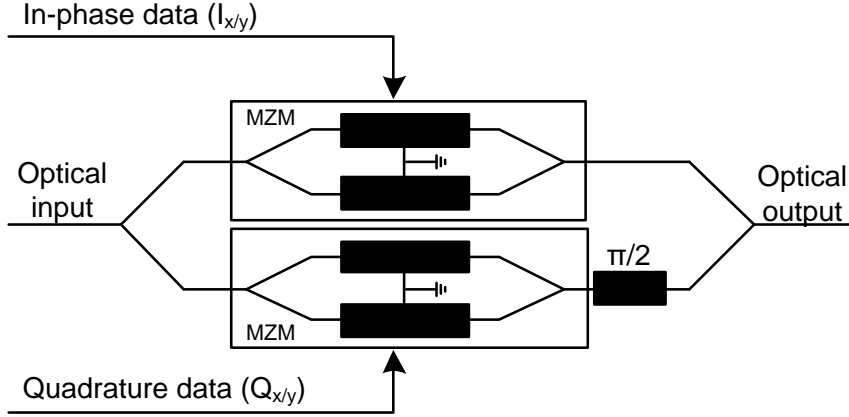


Figure 2.4: Configuration of the in-phase and quadrature modulator. MZM: Mach-Zehnder modulator.

In addition, PM signals are easily generated using two IQMs in a parallel configuration, whose outputs are orthogonally polarized, and combined using a polarization beam combiner (PBC).

2.2 Post-Detection Digital Signal Processing

Another benefit brought by coherent transmission systems is the possibility to perform compensation of the transmission impairments in the digital domain. The performance and reliability improvements of integrated circuits have made DSP a viable solution to recover the transmitted symbols from the received signal. Adaptive signal equalization and fast control response are two advantages of DSP when compared to optical control methods.

The basic post-detection DSP subsystems used to recover PM-QAM signals in high-speed ULH transmission systems are shown in Figure 2.5. Initially, the four digitized signals are compensated against optical front-end imperfections, subsystems within the pre-processing block, followed by the compensation of the fiber transmission impairments, subsystems within channel equalization block in the figure. Afterwards, clock and carrier recovery are applied to adjust the timing, frequency and phase information of the incoming samples. Finally, symbol decoding and hard- or soft-decision FEC are performed.

In the next subsections, we describe DSP algorithms that can be used for compensating the optical signal impairments. Note that, although FEC decoding plays an important role in the DSP subsystems, it is outside the scope of this thesis and consequently we will not elaborate on this topic.

2.2.1 Pre-processing

During modulation and demodulation, the four signals ($I_{x/y}$, $Q_{x/y}$) traverse different optical paths that might have slightly different lengths, consequently the signals might

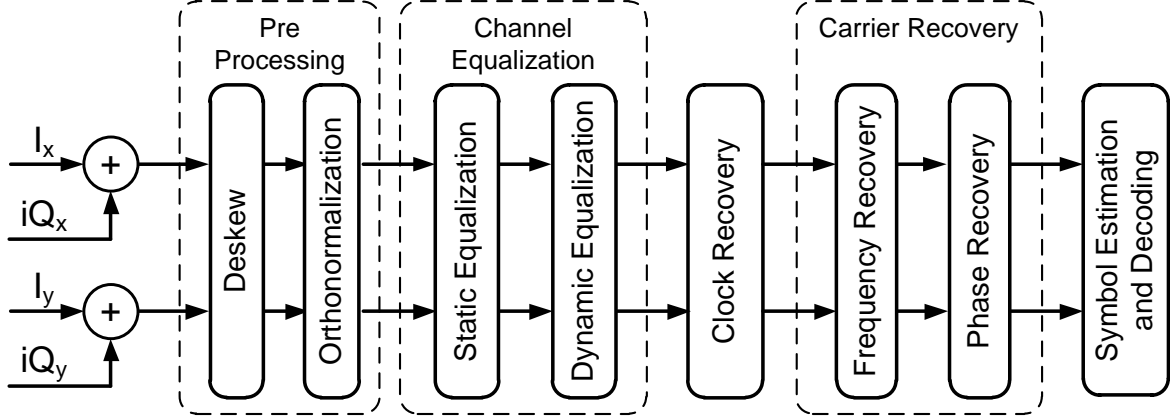


Figure 2.5: Post-detection digital signal processing subsystems used in coherent receivers.

have different delays between them, resulting in a time skew. Besides that, the 90° optical hybrid I and Q output signals might lose their orthogonality due to imperfections in the optical hybrid and responsivity mismatches between the photodiodes, which might introduce quadrature imbalance [10]. It is known that, if not correctly compensated, the non-ideal behavior of the optical demodulator and the down-converters can negatively impact the correct efficiency of the subsequent DSP algorithms and consequently degrade the performance of the system.

The temporal misalignments can be digitally removed using the deskew algorithm proposed in [11]. Alternatively, a blind adaptive 4×4 multiple-input multiple-output (MIMO) equalizer was proposed in [12], which can compensate for the in-phase and quadrature timing skew and relax the requirements on the optical components. A similar structure was proposed in [13] where training sequences and decision-directed (DD) equalization was used. In this last case, frequency offset and phase noise have to be removed prior to equalization.

The orthogonality mismatch can be compensated with the widely used Gram-Schmidt orthogonalization procedure [14, 15] or, alternatively, with the Löwdin algorithm [16]. Note that, the use of such algorithms can be avoided by proper dimensioning of the optical devices.

2.2.2 Channel equalization

The next step in the DSP chain is the compensation of the channel transmission impairments. For low optical power, long-haul high-speed optical transmission systems suffer only from linear impairments. In this situation, the transmitted signal will suffer from frequency dependent distortions, such as ISI resulting from CD and PMD of the link [17]. In addition, polarization components will be mixed together due to the birefringence of the optical fiber. In order to effectively compensate for such effects, fixed and adaptive filters can be digitally implemented. Although such digital filtering could be realized in a single block, it is typically partitioned in two concatenated blocks as illustrated in Figure 2.6.

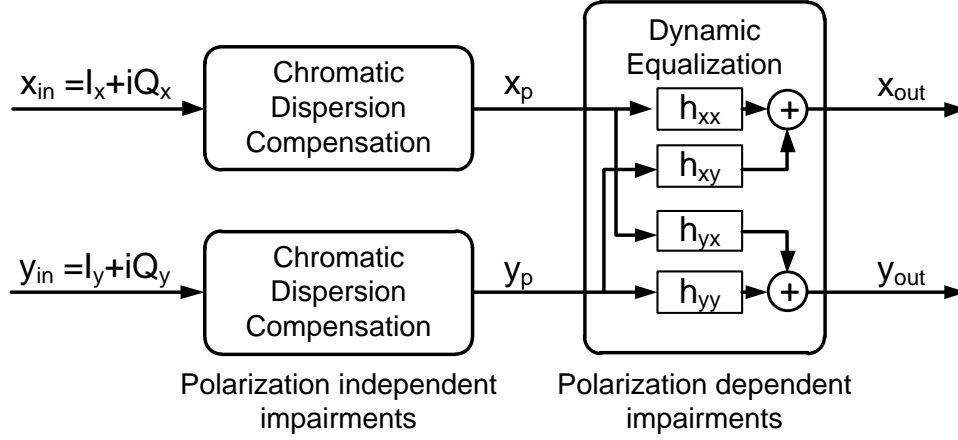


Figure 2.6: Block diagram for the channel impairments equalization, where two concatenated blocks are applied to perform static and adaptive equalization of the signal independently.

The first block compensates for CD of the link, which is also known as group-velocity dispersion (GVD). It is normally called static equalization block since CD value is usually time invariant, therefore a fixed equalizer with predetermined tap coefficients is used. The second block compensates for time varying channel impairments, such as state of polarization and PMD, and therefore it is normally called dynamic equalization. In this case, a set of equalizers with adaptive tap coefficients are used. By controlling the tap coefficients of those filters, we can induce the inverse transfer function of the transmission link and compensate for the transmission impairments.

Static equalization: The received complex signal is initially equalized by a fixed time- or frequency-domain equalizer. The frequency-domain transfer function representing the effect of CD in the optical fiber is given by

$$H_{CD}(\omega) = \exp\left(i\frac{\beta_2}{2}\omega^2 z\right), \quad (2.12)$$

where ω is the angular frequency, β_2 is the group velocity dispersion coefficient and z is the spatial coordinate. Alternatively, the above equation is also frequently described through the dispersion parameter, D , which is related to β_2 by the following equation

$$\beta_2 = -\frac{D\lambda^2}{2\pi c}, \quad (2.13)$$

where λ is the wavelength and c is the speed of the light in vacuum. In order to remove for the CD effects, we need to apply a filter whose transfer functions is given by the inverse transfer function of the transmission fibers.

In [18] it was shown that dispersion can be compensated in the time-domain with the use of an FIR filter, which has a non-recursive structure. This filter can be digitally implemented using a tapped delay line, where the tap weights are given by

$$a_k = \sqrt{\frac{-icT^2}{D\lambda^2 z}} \exp\left(i \frac{\pi cT^2}{D\lambda^2 z} k^2\right), \quad (2.14)$$

with $-\left\lfloor \frac{N}{2} \right\rfloor \leq k \leq \left\lfloor \frac{N}{2} \right\rfloor$ and $N = 2\left\lfloor \frac{|D|\lambda^2 z}{2cT^2} \right\rfloor + 1$, for a odd number of taps, where $\lfloor x \rfloor$ corresponds to the integer part of x rounded towards minus infinity.

Several time-domain (TD) chromatic dispersion equalization (CDE) algorithms have been demonstrated and are being deployed in commercially available 100G transceivers [17–20]. However, it is known, that the amount of accumulated CD increases with the transmission distance, consequently the impulse response of the filter becomes too long, thus requiring an increased number of complex multiplication. This renders in an infeasible hardware implementation for long transmission distances due to the high footprint and power consumption of the DSP ASIC [21–23]. In [24], we have proposed an efficient multiplierless FIR-based filter for CDE. In this algorithm, after quantizing the FIR filter coefficients, we took advantage of the high multiplicity of their real and imaginary parts, by employing the distributed property of multiplication over addition to reduce the number of multiplication operations, obtaining the distributed FIR-CDE. In addition, the remaining multiplication operations were implemented through shifts and additions, aiming to obtain a multiplierless algorithm. The two proposed equalizers were experimentally validated in a 100G PM-QPSK long-haul optical links, demonstrating computational resources savings in terms of required chip area and latency over benchmark FIR-CDE and frequency-domain (FD)-CDE implementations. We have also experimentally demonstrated that the performance penalty imposed by the coefficient quantization tends to decrease with increasing propagation length, rendering it as an attractive solution for efficient and high-performance CDE in long-haul optical fiber links. Alternatively, the static filter can also be realized using a shorter infinite impulse response (IIR) filter, although additional complexity is required in order to make it a stable and causal filter [25, 26]. Besides that, the feedback structure of the IIR filter is a major drawback for real-time implementation.

Static equalizers based on frequency-domain implementation are widely considered in long-haul transmission systems where the amount of CD is high [27–30]. Frequency-domain equalization can be performed aiming to reduce the computational cost via block processing of the digital signal and efficient implementation of the discrete Fourier transform (DFT). The received signals are initially divided into blocks using a serial-to-parallel converter. Each block of samples is then transformed to the frequency-domain using an fast Fourier transform (FFT) and then multiplied with the inverse transfer function of the fiber which is given by $1/H_{CD}(\omega)$. The output block of the transfer function is transformed back to the time-domain using an inverse fast Fourier transform (IFFT) and serialized using a parallel-to-serial converter. In frequency-domain implementations, the interference between blocks is usually addressed by the overlap-save or overlap-add method [31, 32].

For high optical power, the transmission systems are also impaired by nonlinear effects. The compensation for the nonlinear effects can also be performed in the static equalization block using, for example, DBP algorithms. The main idea behind DBP is to jointly compensate for linear and nonlinear impairments by passing the received

signal through the inverse of the NLSE. Although DBP techniques are efficient in the equalization of nonlinear impairments, they normally require very high computational power and complexity, which make its implementation infeasible. For the last couple of years, this has been a topic of high interest within the scientific community, and simplified algorithms have been developed aiming to make DBP implementation more practicable. This topic will be particularly addressed in the next chapters.

Dynamic equalization: The static equalizer removes most of CD, however some hundreds of ps/nm of residual CD may be bypassed. To address the residual CD and the polarization dependent impairments another equalization stage is required. The received signals are composed of a mixture of x_{in} and y_{in} , which will be adaptively equalized. The impact of polarization dependent effects along the optical fiber can be modeled by a Jones matrix [33]

$$\begin{bmatrix} x_p \\ y_p \end{bmatrix} = \begin{bmatrix} \sqrt{\alpha} \exp(i\delta) & -\sqrt{1-\alpha} \\ \sqrt{1-\alpha} & \sqrt{\alpha} \exp(-i\delta) \end{bmatrix} \begin{bmatrix} x_{in} \\ y_{in} \end{bmatrix}, \quad (2.15)$$

where α and δ are the power splitting ratio and the phase difference between the two polarization modes, respectively. The process of extracting the original x_{in} and y_{in} signals from the received x_p and y_p signals is called polarization demultiplexing. We can estimate the Jones matrix and determine its inverse in order to compensate for the impairments incurred by polarization. However, in contrast with CD which might be considered constant along the time, the Jones matrix may evolve in time due to effects such as rapid variations in the polarization state or polarization-mode dispersion. Therefore the most commonly used compensation scheme uses 2×2 FIR filters with adaptive coefficients in a butterfly structure. Its general structure is shown in Figure 2.6, under dynamic equalization block. For inputs x_p and y_p the output x_{out} and y_{out} are described by the following equations

$$\begin{aligned} x_{out} &= h_{xx}^H x_p + h_{xy}^H y_p, \\ y_{out} &= h_{yx}^H x_p + h_{yy}^H y_p, \end{aligned} \quad (2.16)$$

where h_{xx} , h_{xy} , h_{yx} and h_{yy} are adaptive filters each of each have length N taps. There are different methods for adapting the equalizer in MIMO systems. The constant modulus algorithm (CMA) has been extensively used in PM-QPSK signal based transmission systems [7, 33–37], since it allows to exploit the constant modulus of the received signal. In this case, the filter coefficients are adapted based on the following cost function

$$\begin{aligned} \varepsilon_x &= 1 - |x_{out}|^2, \\ \varepsilon_y &= 1 - |y_{out}|^2, \end{aligned} \quad (2.17)$$

which evaluates the distance of the received point to the unit circle. $\varepsilon_{x/y}$ is then used as feedback signal for error control. This adaptation is well suited for QPSK signals, in which all the constellation points should lie on an unitary circle. However, this algorithm proved to be effective even when higher-order modulation formats are considered [38,

39]. Alternatively, radially-directed equalizers (RDEs) might also be used, in which the cost function evaluates the distance of the received point to its closest circle radius [7]. Another alternative is the use of decision-directed (DD) equalization, where the constellation grid is used as a reference, and the cost function evaluates the distance between the received symbol and its closest point in the reference grid. Often CMA or RDE are first used for pre-convergence of the equalizer, after which the DD mode is applied, thus avoiding convergence problems. The following update equations which follow the stochastic gradient descent algorithm, in our case using CMA as a cost function to update the error, are considered for the filter taps

$$\begin{aligned} h_{xx} &= h_{xx} + \mu \varepsilon_x x_{out} x_p^*, \\ h_{xy} &= h_{xy} + \mu \varepsilon_x x_{out} y_p^*, \\ h_{yx} &= h_{yx} + \mu \varepsilon_y y_{out} x_p^*, \\ h_{yy} &= h_{yy} + \mu \varepsilon_y y_{out} y_p^*, \end{aligned} \tag{2.18}$$

where μ defines the convergence rate of the algorithm, x_p^* and y_p^* are the complex conjugate of x_p and y_p respectively.

In CMA singularity might occur, which means that the taps of the adaptive filter might converge to a solution where both recovered signals converge to the same polarization, due to the blinding update of the weight [18, 40]. Given this, the algorithm can be modified so that the two outputs always have states of polarization orthogonal to each other. In [41] three methods were experimentally evaluated, proving to be able to effectively mitigate singularities. Alternatively, a training sequences might also be used to adapt the filter taps, by using least mean square (LMS) algorithms.

Alternatively, a set of algorithms were developed to operate in the Stokes space, namely polarization demultiplexing [42–44], cross polarization modulation compensation [45] and polarization dependent loss (PDL) compensation [46]. Such methods might be advantageous given the non dependency with modulation formats, lower complexity and/or faster convergence.

2.2.3 Clock recovery

Typically, the transmitter and receiver clocks are not perfectly synchronized, leading to deviations relatively to the ideal sampling instant. Therefore, a digital clock recovery block must be applied in order to compensate for the phase and frequency shifts between the transmitter and receiver clocks.

The clock recovery process can be divided in two stages: i) timing error estimation, where the error between the transmitter and receiver clocks is determined; ii) signal equalization, where the sampling instant of the received signal is adjusted to the ideal instant. In the literature, several techniques have been proposed for timing error estimation, such as, early-late gate, Gardner, and Mueller and Muller algorithms [47–49]. Depending on the signal and system characteristics, the most suitable technique should be applied.

The block diagram of the clock recovery algorithm used in our real-time implementation works is shown in Figure 2.7 [50–53]. The received signal is initially sent

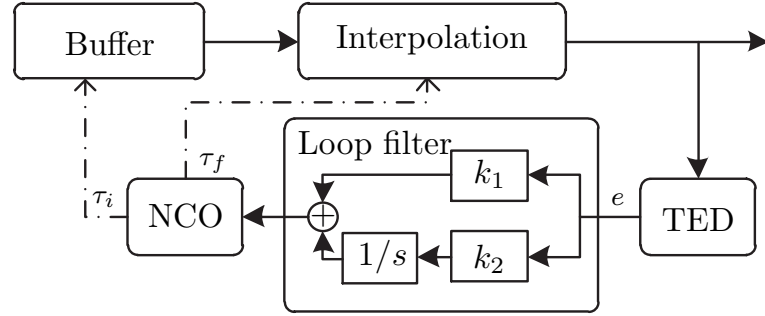


Figure 2.7: Block diagram of the clock recovery algorithm. TED: timing error detector; NCO: numerically controlled oscillator.

to an interpolator block which yields a smoother signal, thus facilitating the adjustment for the ideal sampling instant. The output of the interpolator is then sent to a timing error estimator, where the Gardner algorithm is used to generate the timing error. This was the selected algorithm, since it is simple to be implemented, carrier independent and has a modest oversampling requirement of two samples per symbol [54].

The timing error signal is given by

$$e(n) = (x(n) - x(n-2))x(n-1), \quad (2.19)$$

where $x(n)$ and $x(n-2)$ are the central samples in two consecutive symbols and $x(n-1)$ corresponds to the transition sample [47]. However, the performance of the Gardner algorithm tends to decrease for Nyquist signals with small *roll-off* factor [55], since the signal has a very small eye opening. In order to mitigate for this issue, the timing error signal can be derived from the power of the signal as

$$e(n) = (P(n) - P(n-2))P(n-1). \quad (2.20)$$

The obtained error signal is then sent to a loop filter block, named proportional integrator filter, containing a proportional and an integral section. Its function is given by $(k_1 + k_2/s)$, where the proportional gain k_1 accommodates the variations in clock phase, while the integrator gain k_2/s accommodates the variations in the clock frequency. Since frequency variations are much slower than phase variations and to guarantee the proper convergence of the system, we should have $k_2 \ll k_1$.

Finally, the numerically controlled oscillator block integrates the loop filter output, returning the estimated time delay, τ , which is fed into the interpolator block. The interpolation block is carried out by a 2-taps FIR filter (linear interpolation) updated according to the fractional part of the estimated time delay, τ_f . The integer part of the estimated time delay, τ_i , is used by the input buffer to discard a sample when the accumulated delays are greater than or equal to the sample period. The interpolation output is given by

$$y(n) = (1 - \tau_f)x(n-1) + \tau_fx(n). \quad (2.21)$$

Instead of a linear interpolation, a more robust cubic interpolation can also be applied at the cost of doubling the complexity [52].

To minimize the noise effects in the estimated temporal error, we can calculate the error for the real and imaginary components of the signal and sum them together at the timing error detector output. This presupposes a shared clock between the ADCs for the in-phase and quadrature components, so that the timing errors are very similar. Additionally, for PM systems, we can calculate independent clock timing errors for each polarization, or use only one polarization to estimate the temporal error and use the obtained value to equalize both polarizations. Once again, the last option is a good approach when there is a shared clock between polarizations, since this will allow us to save computational resources.

Note also that, the noise has a significant influence on the performance of this circuit. High noise can lead to errors in τ estimation, causing an incorrect discard of samples or non compensated phase rotations in subsequent algorithms. Small values of k_1 and k_2 provide better noise filtering, but increase the convergence time of the algorithm. On the other hand, high values of k_1 and k_2 allow the tracking of faster clock variations.

2.2.4 Carrier recovery

In current digital coherent receivers there is no laser phase or frequency lock in the optical domain. Thus, the transmitter and receiver lasers do not have exactly the same frequency, yielding a complex rotation of the received signal constellation. Moreover, the laser phase noise (due to nonzero lasers linewidth) also induces phase differences between the received signal and the LO. Therefore, a carrier recovery subsystem has to be implemented aiming to estimate and remove the residual intermediate frequency, ω_{IF} , and laser phase noise from the received signal.

Frequency recovery: Different equalization techniques have been proposed aiming to estimate the frequency deviation between lasers, being the most common ones the differential phase method based on Viterbi-Viterbi algorithm concept [56–58], which is applied in TD, and the spectral method technique, which is applied in FD [59]. The differential phase method estimates the frequency shift between two consecutive symbols, while spectral method is based on the observation of the maximum of the discrete spectrum of received signal raised to the power of four, x_{in}^4 . Alternatively, an iterative method which can be equally applied to QAM formats has been proposed in [60]. Differential phase-based method is the mostly used method due to its hardware-efficient implementation, while avoiding the frequency-time domain transitions [61].

In our previous real-time implementation works [50–53, 62] we have used the 4th-order differential phase-based method, which algorithm block diagram is presented in Figure 2.8. In this algorithm, the phase jump between two consecutive samples is obtained through the complex multiplication of the received symbol with the complex conjugate of the predecessor symbol, $x(n)x^*(n-1)$. For a QPSK signal the received signal will be given by

$$x(n) = \exp \left(i \left(\theta_{noise}(n) + \frac{kn\pi}{2} \right) \right), \quad (2.22)$$

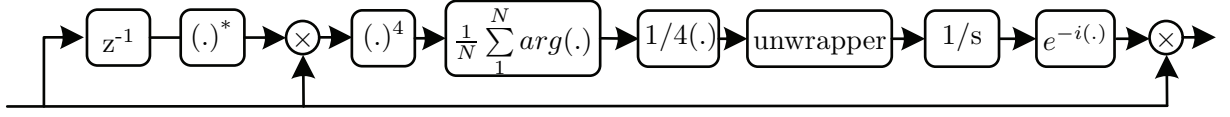


Figure 2.8: Block diagram of the frequency recovery algorithm based on the differential phase-based method.

i.e. the symbols contain a phase component caused by the frequency error, $\exp(i\theta_{noise}(n))$, and the QPSK modulation information, $\exp(i\frac{kn\pi}{2})$, which is undesirable for the frequency estimation. In order to remove this phase modulation, each received symbol must be raised to its fourth power, enabling the frequency estimation using the following expression

$$\begin{aligned} & \left(\exp \left(i \left(\theta_{noise}(n) + \frac{kn\pi}{2} \right) \right) \exp \left(i \left(\theta_{noise}(n-1) + \frac{k(n-1)\pi}{2} \right) \right)^* \right)^4 = \\ & \exp \left(i \left(4\theta_{noise}(n) + 2kn\pi \right) \right) \exp \left(i \left(4\theta_{noise}(n-1) + 2k(n-1)\pi \right) \right)^* = \exp(i4\theta_{noise}). \end{aligned} \quad (2.23)$$

Usually, the received signal does not have unitary amplitude and suffers from phase noise. Thereby to reduce the noise effects in θ_{noise} estimation, the mean of a block of consecutive $\exp(i4\theta_{noise})$ values is used. Finally, the θ_{noise} value is obtained by converting the complex value into an angle and dividing it by 4.

Knowing the phase deviation, θ_{noise} (that should be in the range $[-\pi, \pi]$), the received symbols can be compensated, through

$$x_{eq}(n) = \exp \left(i \left(\theta_{noise}(n) + \frac{kn\pi}{2} \right) \right) \exp \left(-i \left(\theta_{noise}(n) \right) \right) = \exp \left(i \left(\frac{kn\pi}{2} \right) \right). \quad (2.24)$$

However, this value may not be enough to compensate for all the frequency shifts, therefore an “unwrapper” block is required. This block monitors the evolution of the estimated phase and corrects possible phase discontinuities that occur when the phase jumps between symbols exceed $\pi/4$, reducing in this way the probability of cycle-slips.

Phase recovery: After frequency recovery, there is still a random and quick phase rotation of the received signal that has to be compensated. Besides that, there is also some residual frequency deviation that was not compensated due to the imperfect frequency equalization. Many techniques have been proposed aiming to estimate and compensate for the phase noise [63–72]. Blind phase search algorithms have been widely used given their good laser linewidth tolerance and feasibility for parallel implementation. Furthermore, digital phase locked loop has been found to work well for a wide range of M-QAM formats, provided that linewidth requirements are met [73]. Although, feedforward phase estimation techniques, such as the popular Viterbi-Viterbi algorithm [74], are often preferable given their low-complexity implementation.

The Viterbi-Viterbi algorithm was adopted in our real-time implementation works [50–53, 62], and its block diagram is represented in Figure 2.9. This algorithm is

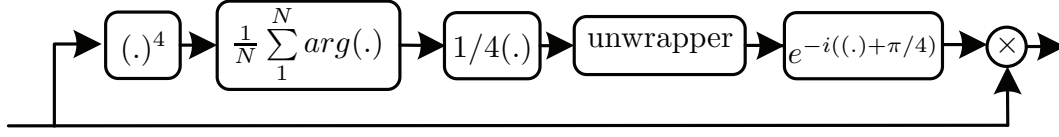


Figure 2.9: Block diagram of the phase recovery algorithm based on the Viterbi-Viterbi algorithm.

conceptually similar to the previous frequency recovery algorithm, although, in this case, we estimate the absolute phase value of the symbols relatively to the orthonormal referential. Once again, the received signal must be raised to the 4th-order power aiming to remove the QPSK modulation information from the phase noise. Thus, the phase error can be simply obtained as follow

$$\frac{1}{4} \arg \left(\exp \left(i4 \left(\theta_{noise,residual}(n) + \frac{kn\pi}{2} \right) \right) \right) = \frac{1}{4} \arg \left(\exp \left(i4\theta_{noise,residual}(n) \right) \right), \quad (2.25)$$

where $\arg(\cdot)$ retrieves the argument of the complex number.

Since the phase alignment is done relatively to the orthonormal referential, to get the constellation centered in $\pm \frac{\sqrt{2}}{2} \pm j \frac{\sqrt{2}}{2}$, a $\pi/4$ phase factor needs to be added to the estimated error phase. Thus, the in-phase and quadrature signal information can be extracted by analyzing the components sign. Once again, an “unwrapper” has to be included to follow the $\theta_{noise,residual}$ variations above $\pi/4$ (or below $-\pi/4$), thus avoiding cycle-slips. As an alternative, differential coding might be considered to minimize the impact of cycle-slips, however this comes at the expense of an increased BER [7, 53].

Once again, the estimated phase is averaged over a number of samples in order to get a better estimation of it. A high number of samples results in a smooth estimated phase, although its low bandwidth limits its tracking capabilities. On the other hand, a small number of samples leads to higher sensitivity of the phase estimator to noise [61].

Note that, the Viterbi-Viterbi algorithm can be easily adapted to M-ary phase-shift keying (PSK) modulation formats by changing the applied 4th-order power to the Mth-order power of the measured complex amplitude. In [75], we proposed an optimized hardware scheme for carrier recovery algorithms based on Mth-order power schemes and showed that the reported architecture saves approximately half of the hardware resources of the frequency recovery stage compared with the fully independent phase and frequency recovery algorithms. However, these algorithms cannot be directly applied to higher-order QAM formats. In [40] a modified version of the Viterbi-Viterbi method was proposed to make it compatible with higher-order modulation formats. Alternatively, two-stage carrier phase estimation (CPE) algorithms were proposed and analyzed for 16QAM and 64QAM signals [76–78], proving to have high tolerance toward laser phase noise.

2.2.5 Symbol demapping

After carrier recovery, the received signal is completely equalized and the modulated information can be extracted using a symbol demapper. The minimum Euclidean distance between the received symbol and a reference symbol can be used as a decision

factor for symbol demapping. In this case, it is assumed that the constellation points are equiprobable, have the same noise distribution and that constellation does not experience any deformation. However, we can not rely always on such assumptions. The noise distribution in the constellation might change with laser phase noise or nonlinear impairments. Consequently constellation point clusters might lose their circular symmetry and the constellation shape might become distorted [79]. To address this problem techniques such as k-means or expectation maximization might be used for symbol demapping [80–82].

After demapping, the incorrect symbol decisions caused by noise, linear and nonlinear impairments can be corrected using FEC techniques. The selection of the FEC code is a matter of tradeoff between SE and coding gain, which is given by the difference between the uncoded and the coded system signal-to-noise ratio (SNR) required to achieve a certain BER. In a hard-decision FEC approach, a firm decision is made on whether a 1 or a 0 has been transmitted. In the latest enhancement of FEC, the soft-decision FEC, a probability factor indicating how likely the demapped bit is correct is considered in the decision process, significantly improving the net coding gain (NCG). When compared to hard-decision FEC, network operators using soft-decision FEC have been reporting gains of 1-2 dB. The use of FEC codes allow us to reduce the error probability, although this comes at the expenses of an overhead increase of 7% for hard-decision FEC and 15%-20% for soft-decision FEC [22, 83–85]. Recently, higher-performance FEC codes suitable for next generation optical networks targeting 100G and above have been proposed aiming to provide an NCG greater than the standard FEC codes at the cost of increased overheads. A detailed survey on the most recent schemes proposed both by academia and industry can be found in [86]. Furthermore, the implementation of FEC comes also at the expense of capacity loss, due to the redundant bits added to the original signal, implementation complexity and power consumption [87, 88].

2.3 High-Order Modulation Formats

The use of digital coherent transmission systems opens the possibility to use higher-order modulation formats and consequently increase the system SE. While the SE of binary modulation formats is limited to 1 bit/s/Hz/polarization, the SE of higher-order modulation formats can reach $\log_2(M)$ bits/s/Hz/polarization, where $\log_2(M)$ is the number of bits encoded in each transmitted symbol. In addition, the use of PM signals allows to double the system SE, by transmitting independent data in the two polarizations of a channel, the symbol-rate is maintained while the bit-rate is doubled. The improvement of SE brought by the use of higher-order modulation formats does not imply an upgrade of the network infrastructures. This means that existing optical amplifiers and ROADMs can still be used, which represents a major cost benefit. On the other hand, for a certain bit-rate, the use of higher-order modulation formats can even relax the requirements of the electronic components due to the reduction of symbol-rate. However, these improvements in terms of SE come at the expense of a higher required OSNR.

Figure 2.10 shows the required analytical SNR as a function of the BER for different

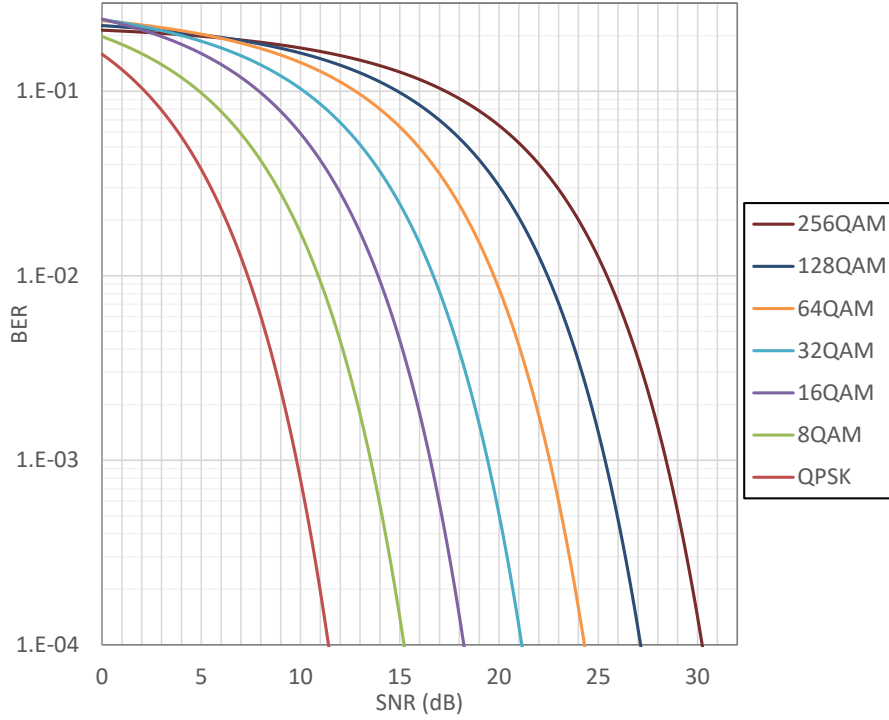


Figure 2.10: Theoretical bit-error ratio as a function of the signal-to-noise ratio for QPSK and M-QAM formats.

M-ary QAM formats. Note that, OSNR can be derived from SNR as follows

$$OSNR = SNR \left(\frac{B_m}{B_r} \right), \quad (2.26)$$

where P_s refers to the signal power, B_m is the equivalent noise bandwidth, N_s is the noise power introduced within B_m , and B_r is the reference optical bandwidth which is usually 0.1 nm (12.5 GHz). From the figure it can be seen that, higher-order modulation formats tend to require higher SNR to achieve the same BER threshold, that in turn can be achieved by increasing the optical input power. Consequently the system sensitivity to fiber nonlinear effects is increased, reducing the maximum achievable transmission distance. Moreover, such modulation formats present higher sensitivity, namely to laser linewidth and quantization error of DACs and ADCs.

Alternatively, for the same spectral bandwidth, the SE can be improved by the increase of symbol-rate. However, it is important to refer that when increasing the symbol-rate, SPM effects become more significant, independently of the considered modulation format [89]. Moreover, the effective number of bits (ENOB) and bandwidth of the ADC are limiting factors to the increase of the symbol-rate. To overcome such limitations, a spectrally-sliced coherent receiver which divides the signal into many narrowband bandwidth spectral slices was proposed in [90]. In this work, each slice is detected with a separate coherent receiver running at a sample-rate lower than the signal bandwidth. The reconstruction of the input waveform is then performed in the

digital domain. Note that, besides stable optical frequency combs and efficient spectral demultiplexers, this technique requires the use of an array of digital coherent receivers.

Over the last years, several transmission systems records have been achieved thanks to the use of higher-order modulation formats. The transmission of 400G Nyquist shaped PM-32QAM signals over 4×100 km of ultra-low-area (ULA) fiber and 50 GHz grid ROADM was first reported in [91]. The transmission distance was then doubled by using a broadband optical spectral shaping technique to counteract the ROADM filtering effects [92]. Also, the transmission of a 400G single-carrier PM-QPSK was demonstrated in [93], where a distance of 4000 km was achieved, using high bandwidth optoelectronic components. A 400G PM-64QAM was also demonstrated using a symbol rate of 43 GBaud, at the expense of a reduced maximum reach of 600 km. In [94], single-carrier modulated 400G transport over transatlantic distances was demonstrated for the first time. Five 64 GBaud PM-16QAM channels were closely packed within 66.7 GHz and 75 GHz channel spacing (owing to the use of Nyquist pulse shaping), resulting in SEs of 6 bits/s/Hz and 5.33 bits/s/Hz, respectively. The achieved maximum reach was of 6600 km and 7200 km, respectively. This solution proved to have a good tradeoff between optoelectronic components bandwidth and transmission distance.

2.4 Hybrid Modulation Formats

Regular M-ary QAM formats have been extensively explored in WDM transmission systems operating at symbol-rates beyond 100G. However, such modulation formats, with fixed number of bits-per-symbol, have the SE limited to discrete values given by [95]

$$SE = BpS\left(\frac{R_s}{\Delta_f}\right), \quad (2.27)$$

where R_s and Δ_f are the symbol-rate and the channel spacing, respectively. In order to provide continuous SE granularity and reduce the SNR gaps given by regular M-ary QAM formats, time-domain hybrid modulation format (TDHMF) was proposed and has been assessed in several numerical and experimental works [95–110].

TDHMF introduce time-dependent modulation, in which two regular M-ary QAM formats of different SE are assigned to different time slots within each frame, thus yielding any desirable transmission bit-rate [95]. Figure 2.11 depicts the transmitted frame of a TDHMF signal, where the hybrid between QPSK and 16QAM is considered.

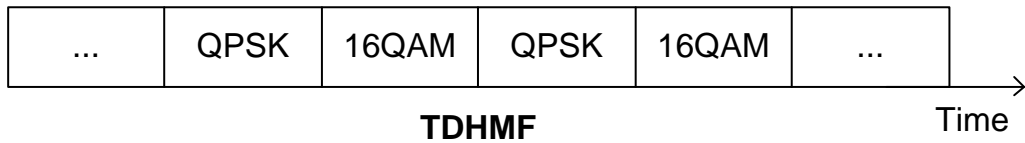


Figure 2.11: Structure of a frame based on time-domain hybrid modulation format between QPSK and 16QAM.

The SE of such formats can be calculated as [101]

$$SE = \left(\frac{M_1}{M_1 + M_2} BpS_1 + \frac{M_2}{M_1 + M_2} BpS_2 \right) \frac{R_s}{\Delta_f}, \quad (2.28)$$

where M_1 and M_2 are the number of symbols corresponding to each modulation format in one frame, and BpS_1 and BpS_2 are the number of bits-per-symbol of each modulation format. By using this technique, we can achieve any SE that falls between the SE of the two considered QAM formats by appropriate adjustment of the frame length and number of time slots attributed to each format. Moreover, from the above equation, it is implicit that different values of M_1 and M_2 can produce the same SE. However, it was shown that by reducing M_1 and M_2 to the minimum values required to get the desired SE, the best system performance is achieved, due to an increased tolerance to fiber nonlinearities [101, 107]. For the implementation of TDHMF based system it is desirable to have format-transparent DSP algorithms to avoid reconfiguration of the receiver, since there is a rapidly switch between modulation formats along the time.

A PM time-domain hybrid 32-64 QAM format, 400 Gbit/s, transmission system was successfully demonstrated in [95]. The proposed format was transmitted over 3200 km of ULA fiber on the standard 50 GHz ITU-T grid, thus achieving a SE of 8 bits/s/Hz. Once again this might be an interesting solution due to the fact that it is compatible with currently installed equipments, thus contributing for the smooth path evolution from existing lower-rate systems based on the 50 GHz grid. In addition, it increases the transport capacity by four times over previous 100 Gbit/s systems. In [108], another TDHMF based on 8-16QAM formats using adaptive symbol-rate was proposed and compared against pure PM-16QAM and PM-8QAM signals. It was experimentally shown that in the presence of strong filtering with cascaded WSS, the TDHMF can reach longer distances when compared to standard PM-16QAM and PM-8QAM formats. In [101] different modulation formats, namely QPSK, 8QAM and 16QAM, together with low-complexity DSP were used in an hybrid way to access the tradeoff between SE and distance. It was shown that the combination of two closer QAM constellation is more desirable, since it gives better performance. The transmission experiments were performed using TDHMF for data rates ranging from 112 Gbit/s to 224 Gbit/s and corresponding distances ranging from 6400 km to 1100 km. Additionally, TDHMF in a superchannel configuration with data rates ranging from 576 Gbits/s and 1.15 Tbit/s and transmission distances ranging from 5600 km to 500 km was also performed.

In [107] an assessment of the optimal transmitter configuration for TDHMF was performed. Curri et al. proposed and tested four transmitter configurations with different PR between modulation formats. It was shown that by changing the PR between modulation formats we can improve the performance of the system when compared to the case where the same power is applied to the different modulation formats. It was also shown that the configuration where the PR is obtained by minimizing the superchannel SNR gives the optimal system performance. The main disadvantage of TDHMF is the extra DSP complexity that is required to process and equalize a time dependent modulation format [111].

In [112], a flexible pulse amplitude modulation (Flex-PAM) was proposed as an alternative to the TDHMF. In Flex-PAM, the hybrid modulation format is based on

four M-ary pulse amplitude modulation (PAM) formats that are independently applied to each in-phase and quadrature axes of the two polarizations. Although, the Flex-PAM presents a granularity that is limited to integer number of bits per symbol with respect to TDHMFs, it brings some advantages in terms of traffic grooming and complexity of transmitter, receiver and DSP [110, 112, 113]. As proposed in [107], a strategy based on forcing all four PAMs to operate at the same BER was shown to be the easiest to be implemented, at the expense of a negligible penalty when compared to the strategy that minimizes the overall Flex-PAM SNR. In [110] both TDHMF and Flex-PAM were assessed in terms of back-to-back (B2B) and signal propagation performance, targeting a flexible low-complexity transponder architecture. Additionally, the impact of fiber nonlinearities was analyzed and two countermeasure techniques, polarization interleaving (PI) and PR tuning, were proposed and numerically assessed in a Nyquist-WDM scenario for bit-rates ranging from 100G up to 300G. It was shown that both techniques provide an improvement in terms of maximum reach, due to the reduction of the nonlinear effects resulting from the power balancing between polarizations.

Alternatively, frequency-domain hybrid modulation format (FDHMF) techniques have also been proposed. In FDHMF, the different regular M-ary QAM formats are attributed to different subcarriers/carriers of the modulated system [111, 114]. Figure 2.12 depicts the transmitted frame of a FDHMF signal, where the hybrid between QPSK and 16QAM is considered. By using this method, it becomes possible to achieve any SE that falls within the two regular QAMs SEs by adjusting the frequency bandwidth occupancy ratio of the two QAMs. In [101], it was shown by simulation that FDHMF is more vulnerable to fiber nonlinearities than TDHMF, due to the fact that in the TDHMF the power of the higher-order modulation format symbols is dispersed to the lower order modulation formats symbols owing to effect of CD during transmission.

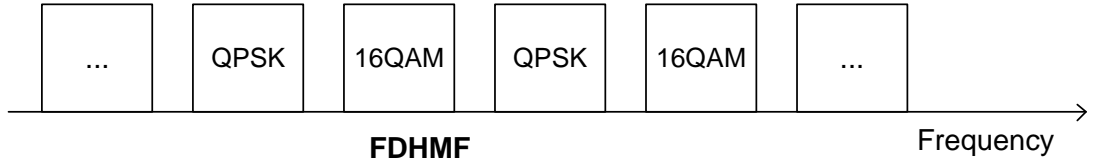


Figure 2.12: Spectrum of a transmitted signal based on frequency-domain hybrid modulation format, the hybrid between QPSK and 16QAM is considered.

Subcarrier multiplexing have been proposed as a solution that optimized the symbol-rate to reduce nonlinear propagation impairments [88, 89, 115, 116], without increasing the number of transceivers in the system. Moreover, subcarrier hybrid systems allows flexibility in data-rate and SE with minimal receiver DSP changes compared to the TDHMF which requires synchronization in time to the modulation. In [114], different configurations of subcarrier multiplexed QAM signals were propagated over a recirculating loop together with 10×100 Gbit/s PM-QPSK channels, in order to quantify performance evolution under tight optical filtering caused by cascade of ROADMs. It was shown that the subcarrier multiplexed hybrid based on PM-QPSK edge subcarriers and PM-16QAM central subcarriers has enhanced filtering tolerance. It was also shown that

subcarrier multiplexed hybrid signals can have a 60% reach improvement over subcarrier multiplexed PM-8QAM signals. In [111], FDHMF based on PM-16QAM and PM-64QAM formats associated with subcarrier multiplexing was proposed and numerically assessed to enable time independent fine bit-rate granularity, ranging from 200G to 300G. Using 8 subcarriers, three FDHMF configurations were considered: i) frequency interleaving of the low- and high-cardinality formats; ii) allocation of the high-cardinality formats to the edge subcarriers and low-cardinality formats to the center subcarriers; and iii) applying the reverse of ii). It was shown that frequency-interleaving of the low and high-cardinality formats is the best approach as it reduces the nonlinear interference between the high-power PM-64QAM subcarriers. PI was also applied for FDHMF. Despite revealing a negligible impact on the average BER performance, it reduces the gap between performing subcarriers, which is beneficial in terms of complexity and effectiveness of FEC. However, by employing PI and optimized format allocation does not improve the system performance relatively to TDHMFs.

A great advantage of higher-order modulation formats based on square grid constellations and equiprobable symbols is its implementation simplicity. However, more recently new techniques have been proposed as an alternative solution for the increase of the bit-rate granularity in flexible networks, while shrinking the gap to the Shannon capacity [85, 117–120]. For example, geometric shaping uses a non-uniformly spaced constellation with equiprobable symbols. Probabilistic shaping uses a uniformly spaced constellation with non-equiprobable symbols. Hybrid shaping combines both geometric and probabilistic shaping. Although the same DSP algorithms can be used for the signal equalization at different spectral efficiencies, the coding and decoding subsystems tends to bring some additional complexity due to the required shaping [85, 118, 119]. This topic is outside the scope of this thesis therefore it will not be extensively addressed here.

2.5 Superchannels

Superchannels have been considered as another promising way of increasing the SE and the network scalability without the replacement of existing network infrastructures, thus being a potential candidate for the next generation high-speed optical systems [94].

A superchannel consists of a group of multiple small bandwidth optical carriers that are aggregated together for improving the overall optical bandwidth occupation and consequently the SE of a transmission system. It was shown that, for the same bit rate, superchannel-based systems provide better performance and higher tolerance to optical filtering when compared to single-carrier systems. This might be due to the fact that single-carrier systems transmit at a higher baud-rate thus requiring higher bandwidth and also higher ENOB from the DACs/ADCs. In [121] it was shown that single-carrier systems based on PM-8QAM, PM-16QAM and PM-32QAM formats present a penalty, when compared to dual-carrier based superchannel systems. Figure 2.13 shows the WDM spectrum of a possible superchannel-based transmission system composed of five carriers each superchannel. The optical carriers are closely packed with a small guard-band between them so that they can be transmitted and routed together as a single entity through the network [88, 122, 123].

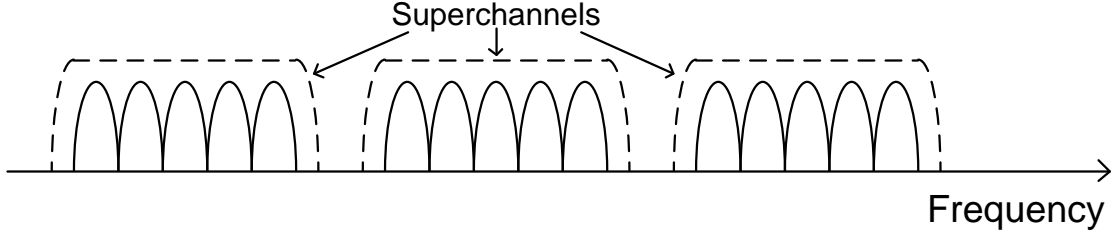


Figure 2.13: WDM spectrum of a superchannel-based system, where each superchannel is made of five carriers separated by a guard-band, in order to allow routing through the network as a single entity.

Two main techniques have been considered in superchannel-based transmission systems: the coherent orthogonal frequency division multiplexing (CO-OFDM) technique [124–127], and the Nyquist-WDM technique [128–130]. In [131] a theoretical comparison between Nyquist-WDM and CO-OFDM techniques was performed, and it was shown that, although the two techniques have potentially the same performance, the Nyquist-WDM technique presents higher robustness to practical implementation constraints. Along this work, we focus only on the Nyquist-WDM superchannel-based transmission systems, given its suitability to high symbol-rate transmission systems [131]. From now on, every mentioning to superchannel refers to the Nyquist-WDM based superchannel, unless otherwise stated.

In the transmitter side of a superchannel systems, each optical carrier is modulated using a dedicated DACs and IQ-modulator, followed by multiplexing and optical transmission stage. At the receiver, a coherent wideband receiver can be used to receive and demodulate all the carriers composing the superchannel, which opens the possibility to do joint processing of all the superchannel carriers at the receiver. Alternatively, when the superchannel bandwidth is too high, multiple LOs can be combined to detect each carrier of the superchannel. In [123], a spectrally-sliced coherent receiver was used to receive the full optical field of a 1.2 Tbit/s PM-16QAM superchannel occupying 176 GHz of optical bandwidth. However, the spectrally-sliced receiver requires a constant phase and amplitude between each LOs. When the phase-coherence between carriers is lost the amount of impairments that can be digital compensated will be significantly reduced [123]. Another coherent receiver architecture which detects and demodulates multiple carriers jointly was also demonstrated in [132]. In [133] a single coherent super-receiver was used to receive a four-carrier 28 GBaud optical superchannel. Also, in [134] and [135] a single digital coherent super-receiver was used to receive a seven-carriers 10 GBaud PM-16QAM and PM-64QAM, respectively.

Several efforts have been made to evaluate the performance of superchannels in high-speed transmission systems. One of the first theoretical works in superchannels can be find in [136], where the performance of Nyquist-WDM terabit superchannels based on four PM M-ary QAM formats was compared through simulations in a B2B configuration and also after nonlinear propagation over uncompensated links for different spectral efficiencies. The purpose of this paper was to determine the maximum transmission distance ensuring a BER below the FEC threshold of 4×10^{-3} , as a function of SE and

total achieved capacity. The maximum transmission distance was derived for different values of subcarrier spacing, starting from the standard 50 GHz grid down to a carrier spacing equal to the baud-rate, which was equal to 27.75 Gbaud for all modulation formats. It was shown that by changing the modulation format from PM-BPSK to PM-16QAM we can increase the net capacity from 4 Tbit/s, for a carrier spacing of 50 GHz, to 27 Tbit/s, for a carrier spacing of 29 GHz (carrier spacing with a penalty lower than 1.5 dB with respect to the single carrier case), in the C-band, although at the expense of a reach reduction from 6480 km to 270 km.

Later on, after demonstrating a single-carrier PM-16QAM at 200 Gbit/s, superchannels systems based on 200G carriers start being proposed. A superchannel composed of two PM-16QAM carriers, within a 87.5 GHz channel spacing, was considered as a likely candidate for the 400G network. In [83] two 200G carriers were combined to achieve 400 Gbit/s and five 200G carriers were combined to achieve 1 Tbit/s superchannels. In [137], it was demonstrated the transmission of five 448 Gbit/s dual-carrier PM-16QAM channels on a 87.5 GHz channel grid, allowing a SE of 4.8 bits/s/Hz over 1230 km of pure silica core fiber (PSCF), where hybrid EDFA-Raman amplification was employed to compensate for span losses. In [87] a 1.28 Tbit/s superchannel transmission system composed of four PM-16QAM carriers within a optical spectrum of 200 GHz and a SE of 5 bits/s/Hz was evaluated over three different kinds of fibers. The transmission performance was improved by employing again hybrid EDFA-Raman amplification (around 50% increase in maximum reach for all the considered scenarios) and by application of single-channel DBP. In [138], Buchali et al. demonstrated 1 Tbit/s dual-carrier PM-64QAM transmission at 64 Gbaud over 320 km of standard single-mode fiber (SSMF) with EDFA only, fully blind offline DSP and a 40% overhead for soft-decision FEC (SD-FEC). In [139], two field trials based on terabit Nyquist superchannels transmission technology over both C- and L-band were reported. In the first trial, each carrier was modulated with 24.8 Gbaud PM-16QAM, transmitting a total of 54.2 Tbit/s over 634 km of field-installed SSFM with hybrid EDFA-Raman amplification and digital coherent detection. In the second trial, the transmission distance was increased to 1822 km by reducing the total capacity to 40.5 Tbit/s, modulating each carrier with PM-8QAM signals and using a rate-adaptive FEC coding. In [140], first time long-haul terabit WDM transmission of PM-16QAM, PM-32QAM and PM-64QAM based superchannels was demonstrated over field deployed SSMF fiber employing hybrid EDFA-Raman amplification over more than ≈ 1571 km, ≈ 1065 km and ≈ 762 km, respectively.

Another advantage of superchannels is its flexibility, carriers can be added or removed from the network to provide the required capacity, thus avoiding the waste of capacity when lower channel capacity is required. The unused carriers might be used by another channel, which would be impossible when using single-carrier systems. This feature together with a flex-grid architecture proposed by the ITU-T will allow the operator to maximize the throughput, given the efficient use of the optical spectrum. In [141] an optical superchannel-based system which uses flexible modulation formats, in order to achieve dynamic transmission distances, was experimentally demonstrated. Different modulation formats were transmitted over a recirculating loop composed of 5 spans of 80 km of SSMF and EDFA-based amplification, demonstrating a flexible system reach

from 800 km to 6000 km, and an SE varying between 6.15 bits/s/Hz to 3.33 bits/s/Hz.

Although superchannel systems are a cost-effective and practical technology, these systems present a high vulnerability to fiber nonlinear effects. In order to reduce the cost per bit, the number of carriers composing a superchannel should be minimum, therefore higher-order modulation formats and higher symbol-rates should be considered. The use of higher-order modulation formats in each carrier will require high OSNR, and consequently, high input power. Besides, the use of smaller guard-bands between carriers hinders the optical demultiplexing of each carrier. It also result in the stronger nonlinear inter-carrier interactions, which significantly decreases the channel performance [122, 123]. Fortunately, superchannel carriers are routed all together through the optical path, enabling us to compensate for the inter-carrier nonlinearities [123]. Note that multi-carrier (MC)-DBP was considered in most of the works above referred, bringing always significant performance improvements. In [142], the performance of a Nyquist-spaced 9-channel 32 Gbaud PM-64QAM WDM superchannel system using the MC-DBP algorithm was evaluated numerically and analytically. It was shown that the performance of MC-DBP in the superchannel improves with the backpropagated bandwidth increase. Single-carrier DBP gives an improvement of approximately 18% in the transmission distance, while the 9-carriers DBP gives more than 100% of reach increase. It was also shown that just a small amount of carriers are mostly contributing for the nonlinear distortions, and carriers far from the carrier of interest contribute significantly less. In [134], MC-DBP for nonlinear mitigation combined with optimized FEC code implementation demonstrated a gain in transmission reach of 85%, increasing the maximum transmission distance from 3190 km to 5890 km. Despite the benefits, MC-DBP faces significant challenges in terms of complexity and the sensitivity to linear channel impairments. As the MC-DBP bandwidth increases, the sensitivity to dispersion also increases, this might limit the performance of DBP in practical system composed of fiber links with non-identical CD parameters. Moreover, as the DBP bandwidth increases, there is a corresponding increase in the number of required nonlinear steps per fiber span.

In the former experiments the entire superchannel was coherently detected and DBP was employed over the total received field as if it were a single-carrier, therefore this technique is sometimes referred as total-field DBP. Despite its straightforward implementation, this total-field DBP technique has been reported as requiring tens of steps per span and very high sampling rate, resulting in unfeasible implementation complexity [123, 134, 135]. As an alternative, in [143] we proposed a MC-DBP technique based on coupled-equations and we compared it against the total-field approach. The couple-equations DBP technique proved to achieve high performance together with lower computational complexity and enhanced robustness to electrical bandwidth limitations. In addition, this approach can also be applied among independent receivers, in contrast with the total-field approach, which requires phase-coherence between all received carriers, thus relaxing the hardware requirements for its implementation. The performance and complexity of this MC-DBP technique was assessed in 400G superchannels based on PM-16QAM, 75 GHz flexigrid, and PM-64QAM, dense 50 GHz grid, achieving 32% and 60% of reach improvement over CDE.

Since superchannels are composed of several carriers that are transmitted together

through the network, we can also make use of an FEC approach, where independent codes are associated to each carrier in order to increase the overall channel performance. The FEC output of all superchannel carriers might be combined in a way that the carriers with better performance can be used to enhance the quality factor of the weaker carriers. Thus, superchannel carriers are placed strategically in the superchannel, so that the carrier with the higher nonlinearity and low quality factor can take advantage of the carrier with the better performance, or even use a higher-order modulation format with higher SE [88]. This technique can also be seen as a nonlinear mitigation strategy for coherent superchannel systems, and this will be explored in detail in Chapter 4.

2.6 Conclusions

In this chapter, we review the architecture of a digital coherent optical transmission system. We describe the current principle of coherent detection and transmission, as well as the DSP algorithms commonly used in high-speed ULH coherent transmission systems. The candidate technologies that have been proposed for the next-generation of high-speed transmission systems were also described.

In optical communication networks, service providers are constantly trying to scale the networks, while lowering capital and operational costs per gigabit per second. Therefore, technologies that offer low cost transceivers but require a line-side upgrade might be rejected for a technologies that present a higher cost transceiver but present compatibility with existing infrastructures [83, 144]. Higher-order modulation formats allow us to scale the capacity of the network without upgrading the network infrastructures. However, using such denser constellation reduce the maximum transmission reach. As an alternative, hybrid modulation formats have been recently proposed and proved to be a promising technique for future high-speed optical transmission systems. Such techniques allow the adjustment of the SE to the system requirements, such as data rate, channel bandwidth and FEC redundancy, thus providing a new degree of freedom in the optimization of the system transmission performance. The use of superchannels-based transmission systems, together with fiber nonlinearity compensation and advanced FEC techniques is seen as a potential candidate for next-generation of optical networks. However, such systems might present a higher power consumption, due to the higher required number of optical components, such as multiple modulators/demodulators, transimpedance and amplifiers. The use of photonic integrated circuits has been pointed out as a possible solution to overcome these limitations [88, 144].

All the above technologies have their pros and cons. Given the circumstances, a given technology might be selected against the other. In the end, multiple technologies might be used together to realize the big picture of scalable high bandwidth networks. Therefore in the following chapters, we focus our attention in the use of superchannel-based systems composed of high-speed higher-order modulation formats. However, since this kind of systems is strongly limited by the nonlinear impairments, we will focus on the study of such systems together with the low-complexity techniques for the compensation and/or mitigation of nonlinear impairments.

References

- [1] A. H. Gnauck, R. W. Tkach, A. R. Chraplyvy, and T. Li, “High-capacity optical transmission systems,” *J. Lightw. Technol.*, vol. 26, no. 9, pp. 1032–1045, 2008.
- [2] M. Birk, P. Gerard, R. Curto, L. E. Nelson, X. Zhou, P. Magill, T. J. Schmidt, C. Malouin, B. Zhang, E. Ibragimov, S. Khatana, M. Glavanovic, R. Lofland, R. Marcoccia, R. Saunders, G. Nicholl, M. Nowell, and F. Forghieri, “Real-time single-carrier coherent 100 Gb/s PM-QPSK field trial,” *J. Lightw. Technol.*, vol. 29, no. 4, pp. 417–425, 2011.
- [3] E. Ip, A. Lau, D. Barros, and J. M. Kahn, “Coherent detection in optical fiber systems,” *Opt. Express*, vol. 16, no. 2, pp. 753–791, 2008.
- [4] A. Leven, N. Kaneda, and S. Corteselli, “Real-time implementation of digital signal processing for coherent optical digital communication systems,” *IEEE J. Sel. Topics Quantum Electron.*, vol. 16, no. 5, pp. 1227–1234, 2010.
- [5] K. Kikuchi, “Fundamentals of coherent optical fiber communications,” *Journal of Lightwave Technology*, vol. 34, no. 1, pp. 157–179, Jan 2016.
- [6] A. Leven, N. Kaneda, U.-V. Koc, and Y.-K. Chen, “Coherent receivers for practical optical communication systems,” in *Optical Fiber Communication and the National Fiber Optic Engineers Conference, 2007. OFC/NFOEC 2007. Conference on*, March 2007, pp. 1–3.
- [7] S. J. Savory, “Digital coherent optical receivers: algorithms and subsystems,” *IEEE J. Sel. Topics Quantum Electron.*, vol. 16, no. 5, pp. 1164–1179, 2010.
- [8] G. P. Agrawal, *Nonlinear Fiber Optics*, 3rd ed. University of Rochester, New York: Academic Press, 2001.
- [9] R. Essiambre and R. W. Tkach, “Capacity trends and limits of optical communication networks,” *Proc. IEEE*, vol. 100, no. 5, pp. 1035–1055, 2012.
- [10] C. S. Petrou, A. Vgenis, I. Roudas, and L. Raptis, “Quadrature imbalance compensation for PDM QPSK coherent optical systems,” *IEEE Photon. Technol. Lett.*, vol. 21, no. 24, pp. 1876–1878, 2009.
- [11] T. Tanimura, S. Oda, T. Tanaka, T. Hoshida, Z. Tao, and J. C. Rasmussen, “A simple digital skew compensator for coherent receiver,” in *Proc. 35th European Conf. Optical Communication (ECOC)*, 2009, pp. 1–2.
- [12] M. Paskov, D. Lavery, and S. Savory, “Blind equalization of receiver in-phase/quadrature skew in the presence of Nyquist filtering,” *IEEE Photon. Technol. Lett.*, vol. 25, no. 24, pp. 2446–2449, 2013.

-
- [13] M. Faruk and K. Kikuchi, "Compensation for in-phase/quadrature imbalance in coherent-receiver front end for optical quadrature amplitude modulation," *Photonics Journal, IEEE*, vol. 5, no. 2, pp. 7 800 110–7 800 110, 2013.
 - [14] I. Fatadin, S. J. Savory, and D. Ives, "Compensation of quadrature imbalance in an optical QPSK coherent receiver," *IEEE Photon. Technol. Lett.*, vol. 20, no. 20, pp. 1733–1735, 2008.
 - [15] S. H. Chang, H. S. Chung, and K. Kim, "Impact of quadrature imbalance in optical coherent QPSK receiver," *IEEE Photonics Technology Letters*, vol. 21, no. 11, pp. 709–711, June 2009.
 - [16] I. Mayer, "On Löwdin's method of symmetric orthogonalization," *International Journal of Quantum Chemistry*, vol. 90, no. 1, pp. 63–65, 2002.
 - [17] M. G. Taylor, "Coherent detection method using DSP for demodulation of signal and subsequent equalization of propagation impairments," *IEEE Photon. Technol. Lett.*, vol. 16, no. 2, pp. 674–676, 2004.
 - [18] S. J. Savory, "Digital filters for coherent optical receivers," *Opt. Express*, vol. 16, no. 2, pp. 804–817, Jan 2008.
 - [19] M. G. Taylor, "Compact digital dispersion compensation algorithms," in *OFC/NFOEC 2008 - 2008 Conference on Optical Fiber Communication/National Fiber Optic Engineers Conference*, Feb 2008, pp. 1–3.
 - [20] T. Xu, G. Jacobsen, S. Popov, J. Li, E. Vanin, K. Wang, A. T. Friberg, and Y. Zhang, "Chromatic dispersion compensation in coherent transmission system using digital filters," *Opt. Express*, vol. 18, no. 15, pp. 16 243–16 257, Jul 2010.
 - [21] B. S. G. Pillai, B. Sedighi, W. Shieh, and R. S. Tucker, "Chromatic dispersion compensation - an energy consumption perspective," in *Optical Fiber Communication Conference*. Optical Society of America, 2012, p. OM3A.8.
 - [22] D. A. Morero, M. A. Castrilln, A. Aguirre, M. R. Hueda, and O. E. Agazzi, "Design tradeoffs and challenges in practical coherent optical transceiver implementations," *Journal of Lightwave Technology*, vol. 34, no. 1, pp. 121–136, Jan 2016.
 - [23] G. Goldfarb, M. G. Taylor, and G. Li, "Experimental demonstration of fiber impairment compensation using the split-step finite-impulse-response filtering method," *IEEE Photon. Technol. Lett.*, vol. 20, no. 22, pp. 1887–1889, 2008.
 - [24] C. S. Martins, F. P. Guiomar, S. B. Amado, R. M. Ferreira, S. Ziaie, A. Shahpari, A. L. Teixeira, and A. N. Pinto, "Distributive FIR-based chromatic dispersion equalization for coherent receivers," *J. Lightwave Technol.*, vol. 34, no. 21, pp. 5023–5032, Nov 2016.

- [25] G. Goldfarb and G. Li, "Chromatic dispersion compensation using digital IIR filtering with coherent detection," *IEEE Photon. Technol. Lett.*, vol. 19, no. 13, pp. 969–971, 2007.
- [26] —, "Demonstration of fibre impairment compensation using split-step infinite-impulse-response filtering method," *Electron. Lett.*, vol. 44, no. 13, pp. 814–816, 2008.
- [27] J. Leibrich and W. Rosenkranz, "Frequency domain equalization with minimum complexity in coherent optical transmission systems," in *Proc. Optical Fiber Communication Conf. and Exposition (OFC)*, paper OWV1. Optical Society of America, 2010.
- [28] T. Xu, G. Jacobsen, S. Popov, M. Forzati, J. Mrtensson, M. Mussolin, J. Li, K. Wang, Y. Zhang, and A. T. Friberg, "Frequency-domain chromatic dispersion equalization using overlap-add methods in coherent optical system," vol. 32, pp. 131–135, 06 2011.
- [29] P. Poggiolini, A. Carena, V. Curri, and F. Forghieri, "Evaluation of the computational effort for chromatic dispersion compensation in coherent optical PM-OFDM and PM-QAM systems," *Opt. Express*, vol. 17, no. 3, pp. 1385–1403, Feb 2009.
- [30] B. Spinnler, "Equalizer design and complexity for digital coherent receivers," *IEEE J. Sel. Topics Quantum Electron.*, vol. 16, no. 5, pp. 1180–1192, 2010.
- [31] M. Kuschnerov, F. N. Hauske, K. Piyawanno, B. Spinnler, M. S. Alfiad, A. Napoli, and B. Lankl, "DSP for coherent single-carrier receivers," *J. Lightw. Technol.*, vol. 27, no. 16, pp. 3614–3622, 2009.
- [32] R. Kudo, T. Kobayashi, K. Ishihara, Y. Takatori, A. Sano, and Y. Miyamoto, "Coherent optical single carrier transmission using overlap frequency domain equalization for long-haul optical systems," *Journal of Lightwave Technology*, vol. 27, no. 16, pp. 3721–3728, 2009.
- [33] K. Kikuchi, "Polarization-demultiplexing algorithm in the digital coherent receiver," in *Proc. Digest of the IEEE/LEOS Summer Topical Meetings*, paper MC2.2, 2008, pp. 101–102.
- [34] C. R. S. Fludger, T. Duthel, D. van den Borne, C. Schulien, E.-D. Schmidt, T. Wuth, J. Geyer, E. De Man, K. Giok-Djan, and H. de Waardt, "Coherent equalization and POLMUX-RZ-DQPSK for robust 100GE transmission," *J. Lightw. Technol.*, vol. 26, no. 1, pp. 64–72, 2008.
- [35] C. Laperle, B. Villeneuve, Z. Zhang, D. McGhan, H. Sun, and M. O'Sullivan, "WDM performance and PMD tolerance of a coherent 40-Gbit/s dual-polarization QPSK transceiver," *J. Lightw. Technol.*, vol. 26, no. 1, pp. 168–175, 2008.

-
- [36] E. Ip and J. M. Kahn, "Digital equalization of chromatic dispersion and polarization mode dispersion," *J. Lightw. Technol.*, vol. 25, no. 8, pp. 2033–2043, 2007.
 - [37] O. Bertran-Pardo, J. Renaudier, G. Charlet, P. Tran, H. Mardoyan, M. Salsi, and S. Bigo, "Experimental assessment of interactions between nonlinear impairments and polarization-mode dispersion in 100-Gb/s coherent systems versus receiver complexity," *IEEE Photonics Technology Letters*, vol. 21, no. 1, pp. 51–53, Jan 2009.
 - [38] D. Godard, "Self-recovering equalization and carrier tracking in two-dimensional data communication systems," *Communications, IEEE Transactions on*, vol. 28, no. 11, pp. 1867 – 1875, 1980.
 - [39] J. Johnson, R., P. Schniter, T. J. Endres, J. D. Behm, D. R. Brown, and R. A. Casas, "Blind equalization using the constant modulus criterion: a review," *Proc. IEEE*, vol. 86, no. 10, pp. 1927–1950, 1998.
 - [40] I. Fatadin, D. Ives, and S. Savory, "Blind equalization and carrier phase recovery in a 16-QAM optical coherent system," *J. Lightw. Technol.*, vol. 27, no. 15, pp. 3042–3049, 2009.
 - [41] V. N. Rozental, T. F. Portela, D. V. Souto, H. B. Ferreira, and D. A. A. Mello, "Experimental analysis of singularity-avoidance techniques for CMA equalization in DP-QPSK 112-Gb/s optical systems," *Opt. Express*, vol. 19, no. 19, pp. 18 655–18 664, Sep 2011.
 - [42] B. Szafraniec, B. Nebendahl, and T. Marshall, "Polarization demultiplexing in Stokes space," *Opt. Express*, vol. 18, no. 17, pp. 17 928–17 939, 2010.
 - [43] Z. Yu, X. Yi, J. Zhang, M. Deng, H. Zhang, and K. Qiu, "Modified constant modulus algorithm with polarization demultiplexing in Stokes space in optical coherent receiver," *J. Lightw. Technol.*, vol. 31, no. 19, pp. 3203–3209, Oct 2013.
 - [44] N. J. Muga and A. N. Pinto, "Adaptive 3-D Stokes space-based polarization demultiplexing algorithm," *J. Lightw. Technol.*, vol. 32, no. 19, pp. 3290–3298, 2014.
 - [45] P. Serena, A. Ghazisaeidi, and A. Bononi, "A new fast and blind cross-polarization modulation digital compensator," in *2012 38th European Conference and Exhibition on Optical Communications*, Sept 2012, pp. 1–3.
 - [46] N. J. Muga and A. N. Pinto, "Digital PDL compensation in 3D Stokes space," *J. Lightw. Technol.*, vol. 31, no. 13, pp. 2122–2130, 2013.
 - [47] F. Gardner, "A BPSK/QPSK timing-error detector for sampled receivers," *IEEE Transactions on Communications*, vol. 34, no. 5, pp. 423–429, May 1986.
 - [48] L. Litwin, "Matched filtering and timing recovery in digital receivers," *RF design*, vol. 24, no. 9, pp. 32–49, 2001.
-

- [49] N. Stojanovic, F. N. Hauske, C. Xie, and M. Chen, "Clock recovery in coherent optical receivers," in *Photonic Networks; 12. ITG Symposium; Proceedings of*, May 2011, pp. 1–4.
- [50] R. M. Ferreira, A. Shahpari, S. B. Amado, P. Costa, F. P. Guiomar, A. N. Pinto, and A. L. Teixeira, "Impact of TWDM on optional real-time QPSK WDM channels," in *40th European Conference on Optical Communication (ECOC)*, no. P.7.19, Sept 2014, pp. 1–3.
- [51] R. M. Ferreira, J. D. Reis, S. M. Rossi, S. B. Amado, A. Shahpari, N. G. Gonzalez, J. R. F. Oliveira, A. N. Pinto, and A. L. Teixeira, "Demonstration of Nyquist UDWDM-PON with digital signal processing in real-time," in *Proc. Optical Fiber Communication Conf. and Exposition (OFC)*, 2015.
- [52] R. M. Ferreira, J. D. Reis, S. B. Amado, A. Shahpari, F. P. Guiomar, J. R. F. Oliveira, A. N. Pinto, and A. L. Teixeira, "Performance and complexity of digital clock recovery for Nyquist UDWDM-PON in real time," *IEEE Photonics Technology Letters*, vol. 27, no. 21, pp. 2230–2233, Nov 2015.
- [53] R. M. Ferreira, J. D. Reis, S. M. Rossi, S. B. Amado, F. P. Guiomar, A. Shahpari, J. R. F. Oliveira, A. N. Pinto, and A. L. Teixeira, "Coherent Nyquist UDWDM-PON with digital signal processing in real time," *Journal of Lightwave Technology*, vol. 34, no. 2, pp. 826–833, Jan 2016.
- [54] X. Zhou and X. Chen, "Parallel implementation of all-digital timing recovery for high-speed and real-time optical coherent receivers," *Opt. Express*, vol. 19, no. 10, pp. 9282–9295, May 2011.
- [55] M. Yan, Z. Tao, L. Dou, L. Li, Y. Zhao, T. Hoshida, and J. C. Rasmussen, "Digital clock recovery algorithm for Nyquist signal," in *2013 Optical Fiber Communication Conference and Exposition and the National Fiber Optic Engineers Conference (OFC/NFOEC)*, March 2013, pp. 1–3.
- [56] A. Leven, N. Kaneda, U.-V. Koc, and Y.-K. Chen, "Frequency estimation in intradyne reception," *IEEE Photon. Technol. Lett.*, vol. 19, no. 6, pp. 366–368, 2007.
- [57] L. Li, Z. Tao, S. Oda, T. Hoshida, and J. C. Rasmussen, "Wide-range, accurate and simple digital frequency offset compensator for optical coherent receivers," in *Proc. Optical Fiber Communication Conf. and Exposition (OFC)*, paper OWT4, 2008.
- [58] M. Taylor, "Phase estimation methods for optical coherent detection using digital signal processing," *J. Lightw. Technol.*, vol. 27, no. 7, pp. 901–914, april, 2009.
- [59] M. Morelli and U. Mengali, "Feedforward frequency estimation for PSK: a tutorial review," *European Transactions on Telecommunications*, vol. 9, pp. 103–116, 1998.

-
- [60] M. Selmi, Y. Jaouen, and P. Ciblat, "Accurate digital frequency offset estimator for coherent PolMux QAM transmission systems," in *Proc. 35th European Conf. Optical Communication (ECOC)*, paper P3.08, 2009.
- [61] S. Hoffmann, S. Bhandare, T. Pfau, O. Adamczyk, C. Wordehoff, R. Peveling, M. Porrmann, and R. Noe, "Frequency and phase estimation for coherent QPSK transmission with unlocked DFB lasers," *IEEE Photon. Technol. Lett.*, vol. 20, no. 18, pp. 1569–1571, 2008.
- [62] S. B. Amado, R. Ferreira, P. S. Costa, F. P. Guiomar, S. Ziaie, A. L. Teixeira, N. J. Muga, and A. N. Pinto, "Clock and carrier recovery in high-speed coherent optical communication systems," in *Proc. SPIE, Second International Conference on Applications of Optics and Photonics*, vol. 9286, 2014, pp. 92 864M–92 864M–7.
- [63] X. Zhou, "An improved feed-forward carrier recovery algorithm for coherent receivers with M-QAM modulation format," *IEEE Photon. Technol. Lett.*, vol. 22, no. 14, pp. 1051–1053, 2010.
- [64] Y. Gao, A. P. T. Lau, C. Lu, J. Wu, Y. Li, K. Xu, W. Li, and J. Lin, "Low-complexity two-stage carrier phase estimation for 16QAM systems using QPSK partitioning and maximum likelihood detection," in *Proc. Optical Fiber Communication Conf. and Exposition (OFC)*, March 2011, pp. 1–3.
- [65] S. Zhang, L. Xu, P. Y. Kam, C. Yu, J. Chen, and T. Wang, "A performance investigation of adaptive phase estimations in coherent optical communications," *IEEE Photonics Technology Letters*, vol. 23, no. 8, pp. 462–464, April 2011.
- [66] T. Pfau, S. Hoffmann, and R. Noé, "Hardware-efficient coherent digital receiver concept with feedforward carrier recovery for M-QAM constellations," *J. Lightw. Technol.*, vol. 27, no. 8, pp. 989–999, Apr 2009.
- [67] M. Seimetz, "Laser linewidth limitations for optical systems with high-order modulation employing feed forward digital carrier phase estimation," in *Proc. Optical Fiber Communication Conf. and Exposition (OFC)*, 2008.
- [68] E. Ip and J. M. Kahn, "Feedforward carrier recovery for coherent optical communications," *J. Lightw. Technol.*, vol. 25, no. 9, pp. 2675–2692, 2007.
- [69] I. Fatadin, D. Ives, and S. J. Savory, "Laser linewidth tolerance for 16QAM coherent optical systems using QPSK partitioning," *IEEE Photon. Technol. Lett.*, vol. 22, no. 9, pp. 631–633, 2010.
- [70] R. Noe, "Phase noise-tolerant synchronous QPSK/BPSK baseband-type intradyne receiver concept with feedforward carrier recovery," *J. Lightw. Technol.*, vol. 23, no. 2, pp. 802–808, 2005.
- [71] J. H. Ke, K. P. Zhong, Y. Gao, J. Cartledge, A. Karar, and M. Rezaia, "Linewidth-tolerant and low-complexity two-stage carrier phase estimation for

- dual-polarization 16QAM coherent optical fiber communications,” *J. Lightw. Technol.*, vol. 30, no. 24, pp. 3987–3992, 2012.
- [72] S. M. Bilal, G. Bosco, J. Cheng, A. P. T. Lau, and C. Lu, “Carrier phase estimation through the rotation algorithm for 64-QAM optical systems,” *Journal of Lightwave Technology*, vol. 33, no. 9, pp. 1766–1773, May 2015.
- [73] S. Zhang, P. Y. Kam, C. Yu, and J. Chen, “Laser linewidth tolerance of decision-aided maximum likelihood phase estimation in coherent optical M-ary PSK and QAM systems,” *IEEE Photon. Technol. Lett.*, vol. 21, no. 15, pp. 1075–1077, 2009.
- [74] A. Viterbi, “Nonlinear estimation of PSK-modulated carrier phase with application to burst digital transmission,” *IEEE Trans. Inf. Theory*, vol. 29, no. 4, pp. 543–551, 1983.
- [75] R. M. Ferreira, A. Shahpari, S. B. Amado, M. Drummond, J. D. Reis, A. N. Pinto, and A. L. Teixeira, “Optimized carrier frequency and phase recovery based on blind M-th power schemes,” *IEEE Photonics Technology Letters*, vol. 28, no. 21, pp. 2439–2442, Nov 2016.
- [76] S. M. Bilal and G. Bosco, “Dual stage carrier phase estimation for 16-QAM systems based on a modified QPSK-partitioning algorithm,” in *2013 15th International Conference on Transparent Optical Networks (ICTON)*, June 2013, pp. 1–4.
- [77] S. Bilal, A. Carena, C. Fludger, and G. Bosco, “Dual stage CPE for 64QAM optical systems based on a modified QPSK-partitioning algorithm,” *IEEE Photon. Technol. Lett.*, vol. 26, no. 3, pp. 267–270, Feb 2014.
- [78] K. P. Zhong, J. H. Ke, Y. Gao, J. C. Cartledge, A. P. T. Lau, and C. Lu, “Carrier phase estimation for DP-16QAM using QPSK partitioning and quasi-multiplier-free algorithms,” in *OFC 2014*, March 2014, pp. 1–3.
- [79] R. Borkowski, D. Zibar, and I. T. Monroy, “Anatomy of a digital coherent receiver,” *IEICE Transactions*, vol. 97-B, pp. 1528–1536, 2014.
- [80] S. Makovejs, D. S. Millar, D. Lavery, C. Behrens, R. I. Killey, S. J. Savory, and P. Bayvel, “Characterization of long-haul 112Gbit/s PDM-QAM-16 transmission with and without digital nonlinearity compensation,” *Opt. Express*, vol. 18, no. 12, pp. 12 939–12 947, Jun 2010.
- [81] D. Zibar, O. Winther, N. Franceschi, R. Borkowski, A. Caballero, V. Arlunno, M. N. Schmidt, N. G. Gonzales, B. Mao, Y. Ye, K. J. Larsen, and I. T. Monroy, “Nonlinear impairment compensation using expectation maximization for dispersion managed and unmanaged PDM 16-QAM transmission,” *Opt. Express*, vol. 20, no. 26, pp. B181–B196, Dec 2012.
- [82] Y. Chen, C. Ruprecht, W. Rosenkranz, and N. Hanik, “Fiber nonlinearity compensation for dispersion unmanaged PDM 8-QAM CO-OFDM using

- expectation maximization,” in *2013 18th OptoElectronics and Communications Conference held jointly with 2013 International Conference on Photonics in Switching (OECC/PS)*, June 2013, pp. 1–2.
- [83] S. Perrin, “Moving to 100G & beyond,” ZTE, Tech. Rep., 2012.
- [84] “Soft-decision forward error correction for coherent super-channels,” Infinera, Tech. Rep., 2016.
- [85] K. Roberts, Q. Zhuge, I. Monga, S. Gareau, and C. Laperle, “Beyond 100 Gb/s: capacity, flexibility, and network optimization,” *J. Opt. Commun. Netw.*, vol. 9, no. 4, pp. C12–C24, Apr 2017.
- [86] G. Tzimpragos, C. Kachris, I. B. Djordjevic, M. Cvijetic, D. Soudris, and I. Tomkos, “A survey on FEC codes for 100G and beyond optical networks,” *IEEE Communications Surveys Tutorials*, vol. 18, no. 1, pp. 209–221, Firstquarter 2016.
- [87] T. Rahman, D. Rafique, A. Napoli, E. de Man, B. Spinnler, M. Bohn, C. M. Okonkwo, A. M. J. Koonen, and H. de Waardt, “Ultralong haul 1.28 Tb/s PM-16QAM WDM transmission employing hybrid amplification,” *J. Lightwave Technol.*, vol. 33, no. 9, pp. 1794–1804, May 2015.
- [88] “The next generation of coherent optical,” Infinera, Tech. Rep., 2016.
- [89] P. Poggiolini, A. Nespola, Y. Jiang, G. Bosco, A. Carena, L. Bertignono, S. M. Bilal, S. Abrate, and F. Forghieri, “Analytical and experimental results on system maximum reach increase through symbol rate optimization,” *Journal of Lightwave Technology*, vol. 34, no. 8, pp. 1872–1885, April 2016.
- [90] N. Fontaine, “Spectrally-sliced coherent receivers for THz bandwidth optical communications,” in *Proc. 39th European Conf. Optical Communication (ECOC)*, paper Mo.3.C.1, Sept 2013, pp. 1–3.
- [91] X. Zhou, L. Nelson, P. Magill, R. Isaac, B. Zhu, D. W. Peckham, P. Borel, and K. Carlson, “8 450 Gb/s, 50 GHz spaced, PDM-32QAM transmission over 400 km and one 50 GHz-grid ROADM,” in *Proc. Optical Fiber Communication Conf. and Exposition (OFC)*, paper PDPB3, 2011.
- [92] X. Zhou, L. Nelson, R. Isaac, P. Magill, B. Zhu, D. Peckham, P. Borel, and K. Carlson, “800 km transmission of 5×450 Gb/s PDM-32QAM on the 50 GHz grid using electrical and optical spectral shaping,” in *Proc. 37th European Conf. Optical Communication (ECOC)*, paper We.8.B.2, 2011.
- [93] G. Raybon, A. Adamiecki, P. Winzer, C. Xie, A. Konczykowska, F. Jorge, J.-Y. Dupuy, L. Buhl, S. Chandrashekhara, S. Draving, M. Grove, and K. Rush, “Single-carrier 400G interface and 10-channel WDM transmission over 4,800 km using all-ETDM 107-Gbaud PDM-QPSK,” in *Proc. Optical Fiber Communication Conf. and Exposition (OFC)*, 2013, pp. 1–4.

- [94] R. Rios-Müller, J. Renaudier, P. Brindel, A. Ghazisaeidi, I. Fernandez, P. Tran, C. Simonneau, L. Schmalen, and G. Charlet, "Spectrally-efficient 400 Gb/s single carrier transport over 7 200 km," *J. Lightwave Technol.*, vol. 33, no. 7, pp. 1402–1407, Apr 2015.
- [95] X. Zhou, L. E. Nelson, P. Magill, R. Isaac, B. Zhu, D. W. Peckham, P. I. Borel, and K. Carlson, "High spectral efficiency 400 Gb/s transmission using PDM time-domain hybrid 32-64QAM and training-assisted carrier recovery," *J. Lightw. Technol.*, vol. 31, no. 7, pp. 999–1005, 2013.
- [96] W.-R. Peng, I. Morita, and H. Tanaka, "Hybrid QAM transmission techniques for single-carrier ultra-dense WDM systems," in *Opto Electronics and Communications Conference (OECC)*, 2011, pp. 824–825.
- [97] Q. Zhuge, M. Morsy-Osman, X. Xu, M. E. Mousa-Pasandi, M. Chagnon, Z. A. El-Sahn, and D. V. Plant, "Pilot-aided carrier phase recovery for M-QAM using superscalar parallelization based PLL," *Opt. Express*, vol. 20, no. 17, pp. 19 599–19 609, Aug 2012.
- [98] X. Zhou and L. E. Nelson, "400G WDM transmission on the 50 GHz grid for future optical networks," *J. Lightw. Technol.*, vol. 30, no. 24, pp. 3779 –3792, 2012.
- [99] X. Zhou, L. Nelson, R. Issac, P. Magill, B. Zhu, and D. Peckham, "1200 km transmission of 50 GHz spaced, 5×504 Gb/s PDM-32-64 hybrid QAM using electrical and optical spectral shaping," in *Proc. Optical Fiber Communication Conf. and Exposition (OFC)*, paper OM2A.2, 2012.
- [100] X. Zhou, L. E. Nelson, R. Isaac, P. D. Magill, B. Zhu, D. W. Peckham, P. Borel, and K. Carlson, "4000 km transmission of 50 GHz spaced, 10×494.85 Gb/s hybrid 32-64QAM using cascaded equalization and training-assisted phase recovery," in *Proc. Optical Fiber Communication Conf. and Exposition (OFC)*, paper PDP5C.6, 2012.
- [101] Q. Zhuge, M. Morsy-Osman, X. Xu, M. Chagnon, M. Qiu, and D. Plant, "Spectral efficiency-adaptive optical transmission using time domain hybrid QAM for agile optical networks," *J. Lightw. Technol.*, vol. 31, no. 15, pp. 2621–2628, 2013.
- [102] Q. Zhuge, X. Xu, M. Morsy-Osman, M. Chagnon, M. Qiu, and D. Plant, "Time domain hybrid QAM based rate-adaptive optical transmissions using high speed DACs," in *Proc. Optical Fiber Communication Conf. and Exposition (OFC)*, paper OTh4E.6, 2013.
- [103] X. Zhou, L. Nelson, and P. Magill, "Rate-adaptable optics for next generation long-haul transport networks," *IEEE Commun. Mag.*, vol. 51, no. 3, pp. 41–49, 2013.
- [104] X. Zhou, L. Nelson, R. Isaac, P. Magill, B. Zhu, P. Borel, K. Carlson, and D. Peckham, "12,000 km transmission of 100 GHz spaced, 8×495 Gb/s PDM

- time-domain hybrid QPSK-8QAM signals,” in *Proc. Optical Fiber Communication Conf. and Exposition (OFC)*, paper OTu2B.4, March 2013.
- [105] R. Rios-Muller, J. Renaudier, O. Bertran-Pardo, A. Ghazisaeidi, P. Tran, G. Charlet, and S. Bigo, “Experimental comparison between Hybrid-QPSK/8QAM and 4D-32SP-16QAM formats at 31.2 GBaud using Nyquist pulse shaping,” in *Proc. 39th European Conf. Optical Communication (ECOC)*, paper Th.2.D.2, 2013, pp. 1–3.
- [106] Y. Gao, Q. Zhuge, D. V. Plant, C. Lu, and A. P. tao Lau, “Blind and universal DSP for arbitrary modulation formats and time domain hybrid QAM transmissions,” in *Proc. Optical Fiber Communication Conf. and Exposition (OFC)*. Optical Society of America, 2014, p. Th3E.5.
- [107] V. Curri, A. Carena, P. Poggiolini, R. Cigliutti, F. Forghieri, C. R. Fludger, and T. Kupfer, “Time-division hybrid modulation formats: Tx operation strategies and countermeasures to nonlinear propagation,” in *Proc. Optical Fiber Communication Conf. and Exposition (OFC)*, paper Tu3A.2, 2014.
- [108] W. Idler, F. Buchali, L. Schmalen, K. Schuh, and H. Buelow, “Hybrid modulation formats outperforming 16QAM and 8QAM in transmission distance and filtering with cascaded WSS,” in *2015 Optical Fiber Communications Conference and Exhibition (OFC)*, March 2015, pp. 1–3.
- [109] F. Buchali, W. Idler, L. Schmalen, and K. Schuh, “Performance and advantages of 100 Gb/s QPSK/8QAM hybrid modulation formats,” in *Optical Fiber Communication Conference*. Optical Society of America, 2015, p. Th2A.16.
- [110] F. P. Guiomar, R. Li, C. R. S. Fludger, A. Carena, and V. Curri, “Hybrid modulation formats enabling elastic fixed-grid optical networks,” *IEEE/OSA Journal of Optical Communications and Networking*, vol. 8, no. 7, pp. A92–A100, July 2016.
- [111] F. Guiomar and A. Carena, “Achieving fine bit-rate granularity with hybrid subcarrier modulation,” in *Advanced Photonics 2016 (IPR, NOMA, Sensors, Networks, SPCom, SOF)*. Optical Society of America, 2016, p. SpW3F.2.
- [112] R. Li, P. Cortada, V. Curri, and A. Carena, “Flex-PAM modulation formats for future optical transmission system,” in *2015 Fotonica AEIT Italian Conference on Photonics Technologies*, May 2015, pp. 1–3.
- [113] R. Li, A. Carena, and V. Curri, “Bit-rate maximization for elastic transponders operating in WDM uncompensated amplified links,” in *2016 Optical Fiber Communications Conference and Exhibition (OFC)*, March 2016, pp. 1–3.
- [114] T. Rahman, D. Rafique, B. Spinnler, A. Napoli, M. Bohn, T. Koonen, C. Okonkwo, and H. de Waardt, “Digital subcarrier multiplexed hybrid QAM for data-rate

- flexibility and ROADM filtering tolerance,” in *Optical Fiber Communication Conference*. Optical Society of America, 2016, p. Tu3K.5.
- [115] M. Qiu, Q. Zhuge, X. Xu, M. Chagnon, M. Morsy-Osman, and D. V. Plant, “Subcarrier multiplexing using dacs for fiber nonlinearity mitigation in coherent optical communication systems,” in *OFC 2014*, March 2014, pp. 1–3.
 - [116] A. Nespola, L. Bertignono, G. Bosco, A. Carena, Y. Jiang, S. M. Bilal, P. Poggiolini, S. Abrate, and F. Forghieri, “Experimental demonstration of fiber nonlinearity mitigation in a WDM multi-subcarrier coherent optical system,” in *2015 European Conference on Optical Communication (ECOC)*, Sept 2015, pp. 1–3.
 - [117] G. Bcherer, F. Steiner, and P. Schulte, “Bandwidth efficient and rate-matched low-density parity-check coded modulation,” *IEEE Transactions on Communications*, vol. 63, no. 12, pp. 4651–4665, Dec 2015.
 - [118] F. Buchali, F. Steiner, G. Bcherer, L. Schmalen, P. Schulte, and W. Idler, “Rate adaptation and reach increase by probabilistically shaped 64QAM: an experimental demonstration,” *Journal of Lightwave Technology*, vol. 34, no. 7, pp. 1599–1609, April 2016.
 - [119] J. Cho, S. Chandrasekhar, X. Chen, G. Raybon, and P. Winzer, “Probabilistic constellation shaping and coding: essential elements for capacity-approaching optical communications,” in *Asia Communications and Photonics Conference*. Optical Society of America, 2017, p. Su3B.1.
 - [120] F. P. Guiomar, L. Bertignono, D. Piori, A. Nespola, G. Bosco, A. Carena, and F. Forghieri, “Comparing different options for flexible networking: probabilistic shaping vs. hybrid subcarrier modulation,” in *2017 European Conference on Optical Communication (ECOC)*, Sept 2017, pp. 1–3.
 - [121] Z. Jia, H. C. Chien, J. Zhang, Y. Cai, and J. Yu, “Performance comparison of dual-carrier 400G with 8/16/32-QAM modulation formats,” *IEEE Photonics Technology Letters*, vol. 27, no. 13, pp. 1414–1417, July 2015.
 - [122] A. Amari, O. A. Dobre, R. Venkatesan, O. S. S. Kumar, P. Ciblat, and Y. Jaoun, “A survey on fiber nonlinearity compensation for 400 Gbps and beyond optical communication systems,” *IEEE Communications Surveys Tutorials*, vol. PP, no. 99, pp. 1–1, 2017.
 - [123] N. Fontaine, X. Liu, S. Chandrasekhar, R. Ryf, S. Randel, P. Winzer, R. Delbue, P. Pupalais, and A. Sureka, “Fiber nonlinearity compensation by digital backpropagation of an entire 1.2 Tb/s superchannel using a full-field spectrally-sliced receiver,” in *Optical Communication (ECOC 2013), 39th European Conference and Exhibition on*, Sept 2013, pp. 1–3.
 - [124] Y. Ma, Q. Yang, Y. Tang, S. Chen, and W. Shieh, “1 Tb/s per channel coherent optical OFDM transmission with subwavelength bandwidth access,” in *Proc. Optical Fiber Communication Conf. and Exposition (OFC)*, 2009.

-
- [125] R. Dischler and F. Buchali, "Transmission of 1.2 Tb/s continuous waveband PDM-OFDM-FDM signal with spectral efficiency of 3.3 bit/s/Hz over 400 km of SSF,," in *Proc. Optical Fiber Communication Conf. and Exposition (OFC)*, March 2009, pp. 1–3.
- [126] S. Chandrasekhar, X. Liu, B. Zhu, and D. W. Peckham, "Transmission of a 1.2 Tb/s 24 carrier no-guard-interval coherent OFDM superchannel over 7200 km of ultra-large-area fiber," in *Proc. 35th European Conf. Optical Communication (ECOC)*, 2009.
- [127] L. Zhu, F. Yaman, and G. Li, "Experimental demonstration of XPM compensation for WDM fibre transmission," *Electron. Lett.*, vol. 46, no. 16, pp. 1140–1141, 2010.
- [128] G. Gavioli, E. Torrenco, G. Bosco, A. Carena, V. Curri, V. Miot, P. Poggiolini, F. Forghieri, S. Savory, L. Molle, and R. Freund, "NRZ-PM-QPSK 16×100 Gb/s transmission over installed fiber with different dispersion maps," *IEEE Photon. Technol. Lett.*, vol. 22, no. 6, pp. 371–373, march15, 2010.
- [129] E. Torrenco, R. Cigliutti, G. Bosco, G. Gavioli, A. Alaimo, A. Carena, V. Curri, F. Forghieri, S. Piciaccia, M. Belmonte, A. Brinciotti, A. L. Porta, S. Abrate, and P. Poggiolini, "Transoceanic PM-QPSK terabit superchannel transmission experiments at baud-rate subcarrier spacing," in *Proc. 36th European Conf. Optical Communication (ECOC)*, paper We.7.C.2, 2010.
- [130] J.-X. Cai, Y. Cai, C. R. Davidson, D. G. Foursa, A. Lucero, O. Sinkin, W. Patterson, A. Pilipetskii, G. Mohs, and N. S. Bergano, "Transmission of 96×100G pre-filtered PDM-RZ-QPSK channels with 300% spectral efficiency over 10,608 km and 400% spectral efficiency over 4,368 km," in *Proc. Optical Fiber Communication Conf. and Exposition (OFC)*, paper PDPB10, 2010.
- [131] G. Bosco, A. Carena, V. Curri, P. Poggiolini, and F. Forghieri, "Performance limits of Nyquist-WDM and CO-OFDM in high-speed PM-QPSK systems," *IEEE Photon. Technol. Lett.*, vol. 22, no. 15, pp. 1129–1131, 2010.
- [132] C. Liu, J. Pan, T. Detwiler, A. Stark, Y.-T. Hsueh, G.-K. Chang, and S. E. Ralph, "Joint digital signal processing for superchannel coherent optical communication systems," *Opt. Express*, vol. 21, no. 7, pp. 8342–8356, Apr 2013.
- [133] T. Tanimura, T. Kato, R. Okabe, S. Oda, T. Richter, R. Elschner, C. Schmidt-Langhorst, C. Schubert, J. Rasmussen, and S. Watanabe, "Coherent reception and 126 GHz bandwidth digital signal processing of CO-OFDM superchannel generated by fiber frequency conversion," in *Optical Fiber Communication Conference, OSA Technical Digest (online) (Optical Society of America, 2014)*, 2014.
- [134] R. Maher, T. Xu, L. Galdino, M. Sato, A. Alvarado, K. Shi, S. J. Savory, B. C. Thomsen, R. I. Killey, and P. Bayvel, "Spectrally shaped DP-16QAM super-channel transmission with multi-channel digital back-propagation," *Scientific Reports*, vol. 5, no. 8214, February 2015.

- [135] R. Maher, D. Lavery, D. Millar, A. Alvarado, K. Parsons, R. Killey, and P. Bayvel, "Reach enhancement of 100% for a DP-64QAM super-channel using MC-DBP," in *2015 Optical Fiber Communications Conference and Exhibition (OFC)*, March 2015, pp. 1–3.
- [136] G. Bosco, V. Curri, A. Carena, P. Poggiolini, and F. Forghieri, "On the performance of Nyquist-WDM Terabit superchannels based on PM-BPSK, PM-QPSK, PM-8QAM or PM-16QAM subcarriers," *J. Lightw. Technol.*, vol. 29, no. 1, pp. 53–61, Jan 2011.
- [137] V. A. J. M. Sleiffer, D. van den Borne, V. Veljanovski, M. Kuschnerov, M. Hirano, Y. Yamamoto, T. Sasaki, S. L. Jansen, and H. de Waardt, "Transmission of 448 Gb/s dual-carrier POLMUX-16QAM over 1230 km with 5 flexi-grid roadm passes," in *OFC/NFOEC*, March 2012, pp. 1–3.
- [138] F. Buchali, K. Schuh, L. Schmalen, W. Idler, E. Lach, and A. Leven, "1 Tbit/s dual-carrier DP 64QAM transmission at 64 Gbaud with 40% overhead soft-FEC over 320 km SSMF," in *2013 Optical Fiber Communication Conference and Exposition and the National Fiber Optic Engineers Conference (OFC/NFOEC)*, March 2013, pp. 1–3.
- [139] M. F. Huang, A. Tanaka, E. Ip, Y. K. Huang, D. Qian, Y. Zhang, S. Zhang, P. N. Ji, I. B. Djordjevic, T. Wang, Y. Aono, S. Murakami, T. Tajima, T. J. Xia, and G. A. Wellbrock, "Terabit/s Nyquist superchannels in high capacity fiber field trials using DP-16QAM and DP-8QAM modulation formats," *Journal of Lightwave Technology*, vol. 32, no. 4, pp. 776–782, Feb 2014.
- [140] T. Rahman, D. Rafique, B. Spinnler, S. Calabr, E. de Man, U. Feiste, A. Napoli, M. Bohn, G. Khanna, N. Hanik, E. Pincemin, C. L. Boutt, J. Jauffrit, S. Bordaïs, C. Andr, C. Dourthe, B. Raguns, C. M. Okonkwo, A. M. J. Koonen, and H. de Waardt, "Long-haul transmission of PM-16QAM-, PM-32QAM-, and PM-64QAM-based terabit superchannels over a field deployed legacy fiber," *Journal of Lightwave Technology*, vol. 34, no. 13, pp. 3071–3079, July 2016.
- [141] Y. K. Huang, E. Ip, P. N. Ji, Y. Shao, T. Wang, Y. Aono, Y. Yano, and T. Tajima, "Terabit/s optical superchannel with flexible modulation format for dynamic distance/route transmission," in *OFC/NFOEC*, March 2012, pp. 1–3.
- [142] T. Xu, G. Liga, D. Lavery, B. C. Thomsen, S. J. Savory, R. I. Killey, and P. Bayvel, "Equalization enhanced phase noise in Nyquist-spaced superchannel transmission systems using multi-channel digital back-propagation," *Scientific Reports*, vol. 5, no. 13990, 2015.
- [143] F. P. Guimar, S. B. Amado, R. M. Ferreira, J. D. Reis, S. M. Rossi, A. Chiuchiarelli, J. R. F. de Oliveira, A. L. Teixeira, and A. N. Pinto, "Multicarrier digital backpropagation for 400G optical superchannels," *Journal of Lightwave Technology*, vol. 34, no. 8, pp. 1896–1907, April 2016.

- [144] G. Bennett, “Super-channels DWDM transmission at 100Gb/s and beyond,” Infinera, Tech. Rep., 2012.

Chapter 3

Low-Complexity DBP Algorithms

The capacity and transmission distance of actual coherent optical transmission systems are strongly limited by the fiber nonlinear effects [1–3]. In the last decade, several digital backpropagation (DBP) techniques based on split-step Fourier method (SSFM) [4–7] and Volterra series nonlinear equalizer (VSNE) [8–11] have been proposed aiming to counteract the detrimental impact caused by fiber nonlinearities. Despite of their demonstrated efficiency in mitigating nonlinear impairments [10, 12–14], DBP-based nonlinear equalization (NLE) techniques have been regarded as an highly iterative technique, which frequently makes its practical real-time implementation difficult or even impossible, due to power and size constraints of the target platform. For this reason, several low-complexity DBP algorithms have been also emerging aiming to optimize the tradeoff between achieved performance and computational effort [8, 11, 15–21]. The DBP-based weighted SSFM (W-SSFM) proposed in [18] has been attracting considerable attention. This algorithm includes a finite length memory in the nonlinear branch, enabling up to 80% less DBP steps when compared to the standard SSFM [18]. A new VSNE, the weighted VSNE (W-VSNE), which exploit this time-domain correlation was also proposed in [21]. In this algorithm an adjustable power weighting time-window is introduced in the nonlinear branch in order to reduce the complexity of the standard VSNEs [19, 21].

In this chapter, we propose a dual-carrier PM-16QAM 400G superchannel solution and we evaluate its performance through the application of different low-complexity DBP algorithms [22, 23]. The proposed superchannel is experimental assessment in an ultra-long-haul (ULH) wavelength-division multiplexing (WDM) transmission system composed of five 400G superchannels, placed in a 75 GHz flexigrid. The DBP-based W-SSFM and W-VSNE are experimentally evaluated and compared against the standard and widely used SSFM. The DBP step-size, number of real multiplications and latency requirements of the mentioned DBP techniques, as well as the corresponding reach extension over chromatic dispersion equalization (CDE) are also investigated.

The remaining of this chapter is organized as follow. The concept of DBP is introduced in section 3.1. In section 3.2, we introduce the mathematical formulation of the standard and the weighted versions of the SSFM, as well as the recently proposed time-domain (TD)-VSNE and its weighted version, W-VSNE. The laboratorial setup of the 400G WDM transmission system and the required digital signal processing (DSP) subsystems

are presented in section 3.3. The experimental results are then presented and discussed in sections 3.4, 3.5 and 3.6. Where section 3.4 is devoted to the multi-variable optimization, while sections 3.5 and 3.6 are devoted to the performance evaluation and complexity comparison of the different DBP-based NLE algorithms. Finally, the main conclusions drawn from this chapter are summarized in section 3.7.

3.1 Digital Backpropagation Concept

The optical fiber is known to be a nonlinear propagation channel, where, when considering that all the WDM channels have an invariant polarization along the transmission path, the signal propagation can be described by the scalar nonlinear Schrödinger equation (NLSE) [24], as follows

$$\frac{\partial E(t, z)}{\partial z} + \frac{\alpha}{2} E(t, z) + i \frac{\beta_2}{2} \frac{\partial^2 E(t, z)}{\partial t^2} = i \gamma |E(t, z)|^2 E(t, z). \quad (3.1)$$

In equation (3.1), E is the complex electrical field envelope, z and t are the propagation direction and time, respectively. The fiber characteristic parameters are α , β_2 and γ , corresponding to the fiber attenuation coefficient, second-order dispersion parameter (also known as group-velocity dispersion (GVD) coefficient) and fiber nonlinear coefficient, respectively. However, the Schrödinger equation (3.1) is only valid for single-polarization systems. In the case of polarization-division multiplexing (PDM) or polarization-interleaving systems, the optical signal will be propagated through the fiber in two polarizations x and y . In these cases, the signal propagation can be modeled by the Manakov equation, as follow

$$\frac{\partial E_{x,y}(t, z)}{\partial z} + \frac{\alpha}{2} E_{x,y}(t, z) + i \frac{\beta_2}{2} \frac{\partial^2 E_{x,y}(t, z)}{\partial t^2} = i \frac{8}{9} \gamma \left(|E_x(t, z)|^2 + |E_y(t, z)|^2 \right) E_{x,y}(t, z), \quad (3.2)$$

where E_x and E_y denote the complex electrical fields envelopes in both x and y polarizations, respectively. This equation can be considered when it is assumed that the bandwidth of the total field is narrow, such that polarization-mode dispersion (PMD) can be ignored. The factor 8/9, in the right side of the equation, accounts for PDM systems. From equations (3.1) and (3.2) one can see that signal transmission over optical fibers suffers from several linear and nonlinear distortions, namely fiber attenuation (α), signal dispersion (β_2) and also nonlinear effects (γ).

The attenuation of the optical power, caused by the fiber losses, is modeled as follow

$$\alpha = \frac{10}{L} \log_{10} \left(\frac{P_{in}}{P_{out}} \right), \quad (3.3)$$

where L is the fiber length, P_{in} and P_{out} are the input and output optical powers, respectively. In order to compensate for the optical power attenuation, optical amplifiers are placed along the optical path, these, beside increasing the optical power they also introduce amplified spontaneous emission (ASE) noise. The accumulation of ASE noise might in turn reduce the transmission performance of the optical signal.

Dispersion refers to the pulse broadening, which occurs due to the fact that, within a fiber, different spectral components of the optical signal travel at slightly different group velocities [25]. Since the different spectral components travel at different velocities, they do not arrive simultaneously at the receiver, therefore causing inter-symbol interference (ISI). From β_2 we can determine the value of CD, which is characterized by the coefficient of chromatic dispersion D , through the following expression

$$D = -\frac{2\pi c}{\lambda^2}\beta_2. \quad (3.4)$$

Moreover, due to non ideal manufacturing processes, the optical fiber is not perfectly circular and homogeneous. This leads to modal birefringence that causes differences in the refraction index of both polarizations, consequently the signals being propagated in the two polarizations present different velocities, which contribute to differential-group delay (DGD). It must be mentioned that this delay is not deterministic and it varies with the wavelength and the time, due to deployment conditions such as thermal and mechanical stress. DGD is a potential source of pulse broadening that leads to strong ISI, increasing linearly with the data rate.

In addition, at high data rate transmission, nonlinear effects become very important and their compensation becomes necessary in order to maintain long transmission distances. Nonlinearities occur due to the Kerr effect, which arises from the dependence of the optical fiber refractive index with the intensity of the transmitted signal as [1, 2, 26]

$$n(P) = n_0 + n_2 I(t) = n_0 + n_2 \frac{P(t)}{A_{eff}}, \quad (3.5)$$

where n_0 and n_2 are the linear and nonlinear refractive index, respectively. $I(t)$ is the signal intensity, $P(t)$ is the signal power and A_{eff} is the effective core area. The increase of the optical power or the decrease of the effective core area lead to the increase of nonlinear effects in the fiber. Nonlinear effects are represented in equations (3.1) and (3.2) by the nonlinear coefficient which is given by

$$\gamma = \frac{2\pi n_2}{\lambda A_{eff}}. \quad (3.6)$$

The Kerr effect will cause different kinds of signal distortion depending on the optical power and channel spacing, but also on the fiber dispersion and state of polarization [24]. In an WDM transmission system, each optical channel suffers from self-phase modulation (SPM) due to its own presence, but also from cross-phase modulation (XPM) and four-wave mixing (FWM) due to the presence of neighboring channels in the system, and from cross-polarization modulation (XPoLM) due to the use of both polarizations in the optical fiber. Self- and cross-phase modulation induce nonlinear phase noise, while four-wave mixing causes power transfer between copropagating channels.

In recent years, the equalization of nonlinear effects has been a hot research topic for approaching the achievable rate information. Several digital NLE techniques have been proposed to compensate the optical transmission impairments. This can be implemented in the optical or in the digital domains, either at the transmitter or receiver side, or

even split between the two sides [27]. DBP techniques have been reported as the most effective way to compensate for deterministic linear and nonlinear distortions in the digital domain [3, 12–14, 26], while enabling for higher launched power and longer transmission distances in dense WDM transmission systems. Moreover, it has been proving to be a flexible method since it does not require any symmetry on the link, and the system parameters can be arbitrary adapted [24].

The concept of DBP is based on the propagation of the received signal through a virtual fiber and amplifiers, whose parameters have the opposite sign of those of the transmission link, i.e., $-\alpha$, $-\beta_2$, $-\gamma$. Figure 3.1 depicts the schematic of the DBP concept. Note that, unlike the transmission link, in the virtual fiber the distributed gain is given by the fiber, while the lumped loss is given by the amplifiers.

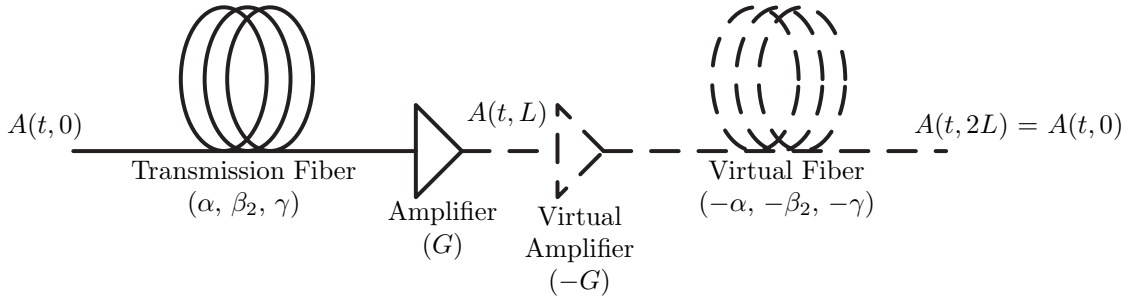


Figure 3.1: Schematic representation of the digital backpropagation concept, where the optical field at the output of the transmission fiber is sent through a virtual fiber whose parameters have opposite sign of those of the transmission fiber.

Along this work, we focus only in PDM optical systems, therefore in the following we present the DBP equation which can be modeled by the inverse Manakov equation [24],

$$\begin{aligned} -\frac{\partial E_x(t, z)}{\partial z} &= \frac{\alpha}{2} E_x(t, z) + i \frac{\beta_2}{2} \frac{\partial^2 E_x(t, z)}{\partial t^2} - i \frac{8}{9} \gamma \left(|E_x(t, z)|^2 + |E_y(t, z)|^2 \right) E_x(t, z), \\ -\frac{\partial E_y(t, z)}{\partial z} &= \frac{\alpha}{2} E_y(t, z) + i \frac{\beta_2}{2} \frac{\partial^2 E_y(t, z)}{\partial t^2} - i \frac{8}{9} \gamma \left(|E_x(t, z)|^2 + |E_y(t, z)|^2 \right) E_y(t, z). \end{aligned} \quad (3.7)$$

The application of DBP techniques opens the possibility to compensate for SPM, which accounts for the auto nonlinear interference induced by the electrical field of the own channel in a single-channel system. Besides, it also allows us to compensate for both XPM and FWM, which accounts for the multi-channel nonlinear interference of a channel induced by the electrical field of the adjacent WDM channels [28].

In the absence of noise and provided that a sufficient number of steps (N_{steps}) is considered, DBP should be able to fully compensate for all the previous deterministic linear and nonlinear fiber impairments. Consequently, this technique would normally require a high number of processing steps, making the complexity of the DBP techniques too high. Thereby, the development of low-complexity DBP algorithms which present a good compromise between efficiency and complexity becomes important, in order to make its real-time implementation and commercial deployment possible [18, 21, 29]. Note however that, the total reconstruction of the transmitted signal is not possible, due to the interaction between the signal and ASE noise, as well as other stochastic effects [7, 28].

3.2 Digital Backpropagation Algorithms

In this section, we start by introducing the standard SSFM, since this is the most used method to numerically solve the nonlinear partial differential Manakov equation. However, it is well known that the computational complexity of the SSFM is high, therefore simplified algorithms that can provide efficient compensation at relatively low computational cost are later on presented. The performance and complexity of the different algorithms used to solve the Manakov equation are, in subsequent chapters, evaluated and compared against the standard DBP-based SSFM.

3.2.1 Split-step Fourier method

The SSFM has been widely used to efficiently solve the Manakov equation [24]. In this technique, the linear and nonlinear elements of equation (3.7) are iteratively solved in the backward direction. The fiber link is divided into a number of small steps, such that in each step the Kerr effects in the spectrum and the dispersion effects in the signal power are minimal. In this work, we consider the computationally less expensive asymmetric SSFM, where the fiber is modeled as a concatenation of the linear and nonlinear sections, evaluated in frequency- and time-domain, respectively [4]. The linear branch, which compensates for CD, is firstly applied, since in backpropagation the nonlinear effects are considered to be stronger at the end of the virtual fiber, where the signal power is higher [4, 26]. The block diagram depicting the implementation of the SSFM is presented in Figure 3.2.

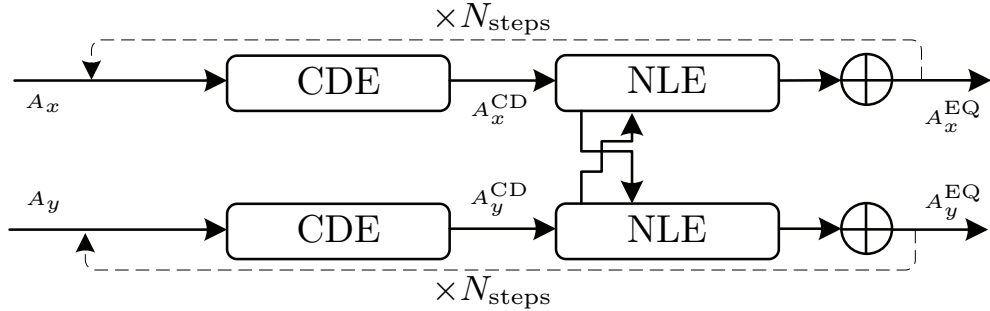


Figure 3.2: Block diagram depicting the implementation of the SSFM, where the linear and nonlinear steps are implemented in a serial configuration. The nonlinear step is applied as the second step since it is assumed that nonlinear effects are stronger at the end of the virtual fiber. The final equalized signal is obtained after applying it over a given number of iterations, N_{steps} .

Considering the asymmetric SSFM, the linear operator performing CDE in frequency-domain is mathematically described as

$$A_{x/y}^{\text{CD}}(t_n, z - h) = \mathcal{F}^{-1} \left\{ \mathcal{F} \{ A_{x/y}(t_n, z) \} H_{\text{CD}}(\omega_n, h) \right\}, \quad (3.8)$$

which represents the multiplication of the received signal by an exponential term. In equation (3.8), $A_{x/y}^{\text{CD}}$ corresponds to the linear equalized signal in the x/y polarization

components, defined at the discrete time instant, t_n . The $\mathcal{F}\{\cdot\}$ and $\mathcal{F}^{-1}\{\cdot\}$ operators represent the direct and inverse Fourier transforms of (\cdot) . An FFT and its inverse, IFFT, are used to convert a signal from its time-domain representation to a frequency-domain representation and vice-versa. H_{CD} is the frequency-domain transfer function for CDE, defined as

$$H_{CD}(\omega_n, h) = \begin{cases} \exp\left(\frac{\alpha}{2}h - i\frac{\beta_2}{2}\omega_n^2 h\right), & h < L_{\text{span}} \\ \exp\left(-i\frac{\beta_2}{2}\omega_n^2 h\right), & h \geq L_{\text{span}} \end{cases}, \quad (3.9)$$

where ω_n represents the discrete angular frequency, L_{span} is the fiber span length and $h = (N_{\text{spans}}/N_{\text{steps}})L_{\text{span}}$ defines the considered DBP step-size, with N_{spans} being the total number of fiber spans. Note that the first condition of equation (3.9) refers to the application of DBP using a subspan step-size, where h must be a divisor of the L_{span} . While the second condition refers to the application of DBP with a multispan step-size, where h must be a multiple of the L_{span} .

After linear equalization, the nonlinear operator, which is responsible for the nonlinear phase shift compensation, is applied in time-domain to deal with the induced nonlinear Kerr effects, as follows

$$A_{x/y}^{\text{EQ}}(t_n, z - h) = A_{x/y}^{\text{CD}}(t_n, z - h) \exp\left[\kappa\left(|A_x^{\text{CD}}(t_n, z - h)|^2 + |A_y^{\text{CD}}(t_n, z - h)|^2\right)\right]. \quad (3.10)$$

In the above equation, $A_{x/y}^{\text{EQ}}$ represents the totally equalized signal in the x/y polarization components and κ is an imaginary constant, defined as follow

$$\kappa = -i\frac{8}{9}\xi\gamma h_{\text{eff}}, \quad (3.11)$$

wherein $0 < \xi \leq 1$ is an optimization parameter that controls the amount of nonlinearities digitally backpropagated. This value depends on the SNR of the received signal and will be chosen to provide the minimum mean square error (MSE) between the equalized and transmitted signals. Lower number of steps leads to coarser field estimation and consequently lower ξ values. This parameter is also dependent on the number of SSFM steps, since it controls the accuracy of optical field estimation at each step.

Finally, h_{eff} corresponds to the effective step-size, which is analytically described by [30]

$$h_{\text{eff}} = \begin{cases} \frac{\exp(\alpha h) - 1}{\alpha}, & h < L_{\text{span}} \\ \frac{h}{L_{\text{span}}} \frac{\exp(\alpha L_{\text{span}}) - 1}{\alpha}, & h \geq L_{\text{span}} \end{cases}. \quad (3.12)$$

The SSFM algorithm was originally developed to accurately simulate the signal propagation over optical fibers [31]. The applied step-size is an important parameter to achieve the intended precision. The considered step-size should be small enough so

that the linear and nonlinear effects are accurately modeled, although this comes at the expenses of high complexity, which can lead to violations of space and power constraints. On the other hand, when large step-sizes are considered, the model loses its precision. The SSFM can be seen as a very precise DBP technique, at the cost of high computational load [18, 26, 29]. In terms of hardware implementation, this technique can be easily implemented due to its independent treatment of linear and nonlinear impairments. But it presents some disadvantages due to its highly iterative structure and hybrid time-/frequency-domain structure. Along this work, the SSFM-based DBP will be considered as a benchmark for comparison with the subsequent reduced-complexity DBP techniques.

3.2.2 Weighted split-step Fourier method

Rafique et. al have recently proposed the W-SSFM, a low-complexity SSFM-based DBP technique, that aims to relax the step-size requirements of the standard SSFM [18]. Unlike the SSFM, in this new method the nonlinear phase shift in one symbol is determined with the power of several consecutive symbols, thus accounting for the pulse broadening that occurs due to CD. Therefore, the W-SSFM includes a finite length memory in the nonlinear step for taking into account the correlation between neighboring symbols. Consequently, this algorithm enables the increase of the DBP step-size, thus enabling the reduction of the number of DBP steps without implying additional complexity, since the power weighting can be efficiently implemented as a simple moving average [18]. The reduction of DBP steps translates in a complexity and latency reduction when compared to the standard SSFM.

The mathematical formulation of the W-SSFM is identical to the above described SSFM, except for the power-weighting average added in the nonlinear step. The nonlinear operator for the W-SSFM, when considering a rectangular time-domain window, is defined as

$$A_{x/y}^{\text{EQ}}(t_n, z - h) = A_{x/y}^{\text{CD}}(t_n, z - h) \exp \left[\frac{\kappa}{N_{\text{NL}}} \sum_{j \in J(n)} \left(|A_x^{\text{CD}}(t_j, z - h)|^2 + |A_y^{\text{CD}}(t_j, z - h)|^2 \right) \right], \quad (3.13)$$

where $J(n) = \{j : n - \lceil \frac{N_{\text{NL}}}{2} \rceil + 1 \leq j \leq n + \lfloor \frac{N_{\text{NL}}}{2} \rfloor\}$, wherein N_{NL} defines the number of samples (window length) to be considered for the power-weighted average. Note that, N_{NL} has to be adjusted for each transmission system in order to obtain the algorithm best performance, this will be analyzed in the following sections.

3.2.3 Time-domain Volterra series nonlinear equalizer

In alternative to the SSFM-based DBP, several VSNE-based DBP approaches based on an third-order Volterra series transfer function (VSTF) have been recently proposed to solve the Manakov equation (3.7) [9, 10, 32]. Although, such approaches provide a nonlinear compensation technique with lower latency, its associated complexity is still very high. This has motivated the development of several low-complexity VSNEs, such as the symmetric Volterra series nonlinear equalizer (symVSNE) and the simplified

Volterra series nonlinear equalizer (simVSNE) proposed in [14, 19]. In these algorithms a symmetric reconstruction of the third-order Volterra Kernel, together with a frequency-flat approximation, are employed in order to reduce the overall complexity of the full VSNE. More recently, a TD formulation for the simVSNE was proposed, enabling to implement a fully TD Volterra-based NLE using closed-form analytical expressions [21]. Additionally, a set of new approximations were employed, emphasizing the insertion of an adjustable power weighting time-window in the nonlinear branch, which was inspired from the above described W-SSFM and which will be addressed in the following subsection.

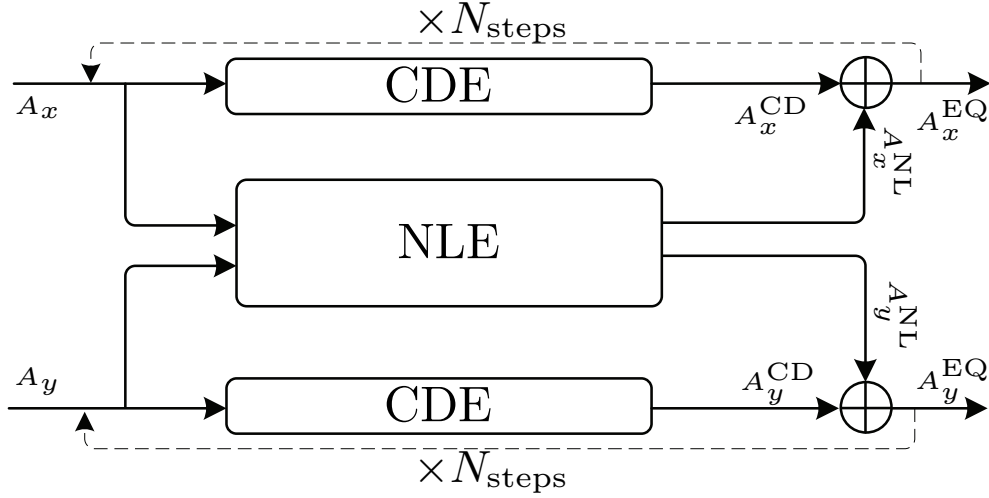


Figure 3.3: Block diagram depicting the implementation of the VSNE-based DBP techniques, where DBP is achieved when the CDE is employed in parallel with the NLE step. The final equalized signal is obtained after applying it a given number of iterations, N_{steps} .

In VSNE-based DBP techniques, DBP is obtained by employing the linear, CDE, in parallel with the nonlinear step, NLE, as can be observed from Figure 3.3. In this case, the NLE is based on a VSNE composed by a set of N_k parallel filters, wherein N_k is an adjustable parameter that defines the filter array dimension, Figure 3.4. The VSNE-based DBP equalized signal is then perturbatively obtained by adding the linear equalized field, $A_{x/y}^{\text{CD}}$, with the nonlinear equalized field, $A_{x/y}^{\text{NL},(K)}$, as follow

$$A_{x/y}^{\text{EQ}}(t_n) = A_{x/y}^{\text{CD}}(t_n) + \sum_{K=-N_k}^{N_k} A_{x/y}^{\text{NL},(K)}(t_n). \quad (3.14)$$

Although, the VSNE can be implemented either in time- or frequency-domain, here we will focus only on our recently proposed TD-VSNE [21]. This novel TD-VSNE was derived from the inverse Fourier analysis of the previously proposed simVSNE algorithm, where a frequency-flat approximation is applied together with a symmetric reconstruction of the Volterra kernel [19]. Additionally, new TD simplifications were implemented in order to avoid the complexity associated with the additional convolution operations, thus giving rise to the simplified TD-VSNE. For simplicity, henceforward each simplified TD-VSNE individual filter will be denoted as TD-VSNE{K} with K being the filter branch order, while the full simplified TD-VSNE filter array will be denoted as TD-VSNE[N_k].

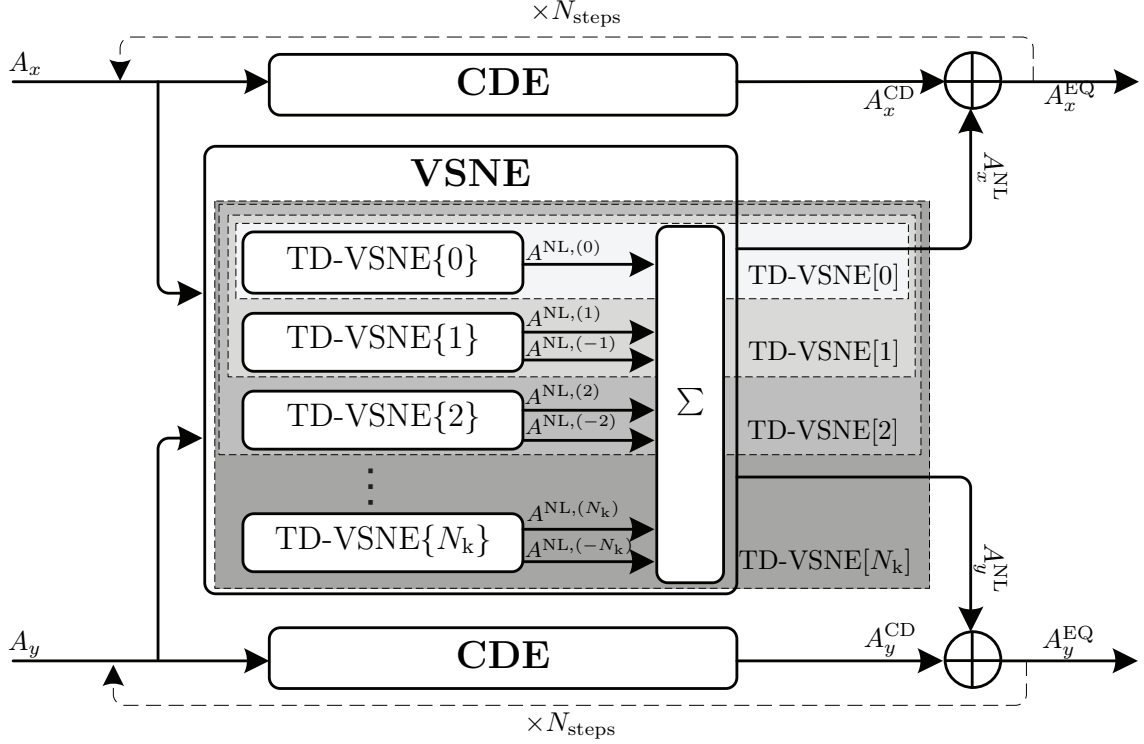


Figure 3.4: Block diagram depicting the implementation of the time-domain VSNE-based DBP approach, where DBP is achieved when the CDE is employed in parallel with the time-domain VSNE. The final equalized signal is obtained after applying it a given number of iterations, N_{steps} .

Regarding the nonlinear equalized fields, the TD-VSNE[0] nonlinear equalized signal in the x/y polarization is mathematically represented as

$$A_{x/y}^{NL,(0)}(t_n) = \kappa \left[A_{x/y}^{CD}(t_n) \left(2P_{xx/yy}(t_n) + P_{yy/xx}(t_n) \right) + A_{y/x}^{CD}(t_n) P_{xy/yx}(t_n) \right], \quad (3.15)$$

where $P_{xx/yy}$ accounts for the optical power in the x/y polarizations

$$P_{xx/yy}(t_n) = \frac{1}{N} \sum_{j \in J_0(n)} |A_{x/y}(t_j)|^2. \quad (3.16)$$

$P_{xy/yx}$ accounts for the coherent inter-polarization nonlinear crosstalk and is given by

$$P_{xy/yx}(t_n) = \frac{1}{N} \sum_{j \in J_0(n)} A_{x/y}(t_j) A_{y/x}^*(t_j), \quad (3.17)$$

where $(\cdot)^*$ represents the complex conjugate of (\cdot) . $J_0(n) = \{j : n - \lceil \frac{N}{2} \rceil + 1 \leq k \leq n + \lfloor \frac{N}{2} \rfloor\}$ defines the moving average interval, which is composed of N taps, with N being the FFT block-size of the corresponding simVSNE.

The remaining N_k parallel TD-VSNE filters are mathematical formulated as follow

$$A_{x/y}^{\text{NL},(\text{K})}(t_n) = \kappa \left[A_{x/y}^{\text{CD},(\text{K})}(t_n) \left(2P_{xx/yy}^{(\text{K})}(t_n) + P_{yy/xx}^{(\text{K})}(t_n) \right) + A_{y/x}^{\text{CD},(\text{K})}(t_n) P_{xy/yx}^{(\text{K})}(t_n) \right], \quad (3.18)$$

and

$$A_{x/y}^{\text{NL},(-\text{K})}(t_n) = \kappa \left[A_{x/y}^{\text{CD},(-\text{K})}(t_n) \left(2P_{xx/yy}^{*(\text{K})}(t_n) + P_{yy/xx}^{*(\text{K})}(t_n) \right) + A_{y/x}^{\text{CD},(-\text{K})}(t_n) P_{yx/xy}^{*(\text{K})}(t_n) \right], \quad (3.19)$$

where

$$A_{x/y}^{\text{CD},(\text{K})}(t_n) = \mathcal{F}^{-1} \left\{ \mathcal{F} \left\{ A_{x/y}(t_n) \exp \left(i2\pi \frac{n}{N} K \right) \right\} H_{\text{CD}}(\omega_n) \right\}, \quad (3.20)$$

with $A_{x/y}^{\text{CD},(0)}(t_n) = A_{x/y}^{\text{CD}}(t_n)$. Note that $A_{x/y}^{\text{CD},(\text{K})}$ can be directly obtained from $A_{x/y}^{\text{CD}}$ using the approximation proposed in section III.c of [21], thus avoiding the additional CD transfer functions and IFFTs computations. Finally, the $P_{xx/yy}^{(\text{K})}$, $P_{xy/yx}^{(\text{K})}$ terms accounting for the cross power between the x and y polarization terms with a $K\Delta\omega$ frequency-shift, where $\Delta\omega$ is the digital frequency resolution, can be obtained as follow

$$P_{xx/yy}^{(\text{K})}(t_n) = \frac{1}{N} \sum_{j \in J_0(n)} |A_{x/y}(t_j)|^2 \exp \left(-i2\pi \frac{j}{N} K \right), \quad (3.21)$$

and

$$P_{xy/yx}^{(\text{K})}(t_n) = \frac{1}{N} \sum_{j \in J_0(n)} A_{x/y}(t_j) A_{y/x}^*(t_j) \exp \left(-i2\pi \frac{j}{N} K \right). \quad (3.22)$$

The final DBP equalized signal is obtained after applying a given number of iterations, N_{steps} , from the output to the input of the filter, Figure 3.4. The parallel structure of the VSNE-based DBP algorithms provide a higher granularity to these equalizers, since it enables to control the overall complexity of the algorithm simply by adjusting the filter dimension parameter, N_k .

3.2.4 Weighted Volterra series nonlinear equalizer

The previous TD-VSNE filters maintain a fixed power weighting time window of N samples, thus guaranteeing the equivalency between the simVSNE formulations in time- and frequency-domains [21]. Nevertheless, it has been shown that the power weighting time-window can be adjusted to provide optimum performance, similarly to W-SSFM. Thereby, the fixed power weighting time-window in the TD-VSNE was substituted by an adjustable power weighting time-window, yielding the W-VSNE. The W-VSNE can be directly obtained from the TD-VSNE by simply redefining the $J_0(n)$ by the $J'_0(n) = \{j : n - \lceil \frac{N_{\text{NL}}}{2} \rceil + 1 \leq j \leq n + \lfloor \frac{N_{\text{NL}}}{2} \rfloor\}$ interval and replacing N by N_{NL} of the exponential factors in equations (3.16), (3.17), (3.20) and (3.22) [21]. This adaptation provides to

the W-VSNE a faster convergence for its maximum performance, allowing the use of less parallel filters, when compared to the TD-VSNE.

Figure 3.5 depicts the block diagram of the W-VSNE-based DBP technique, where in this case the NLE step consists of a step of N_k parallel W-VSNE filters. Like in the previous case, henceforward each W-VSNE individual filter is denoted as $\text{W-VSNE}\{K\}$, while the full W-VSNE filter array will be denoted as $\text{W-VSNE}[N_k]$.

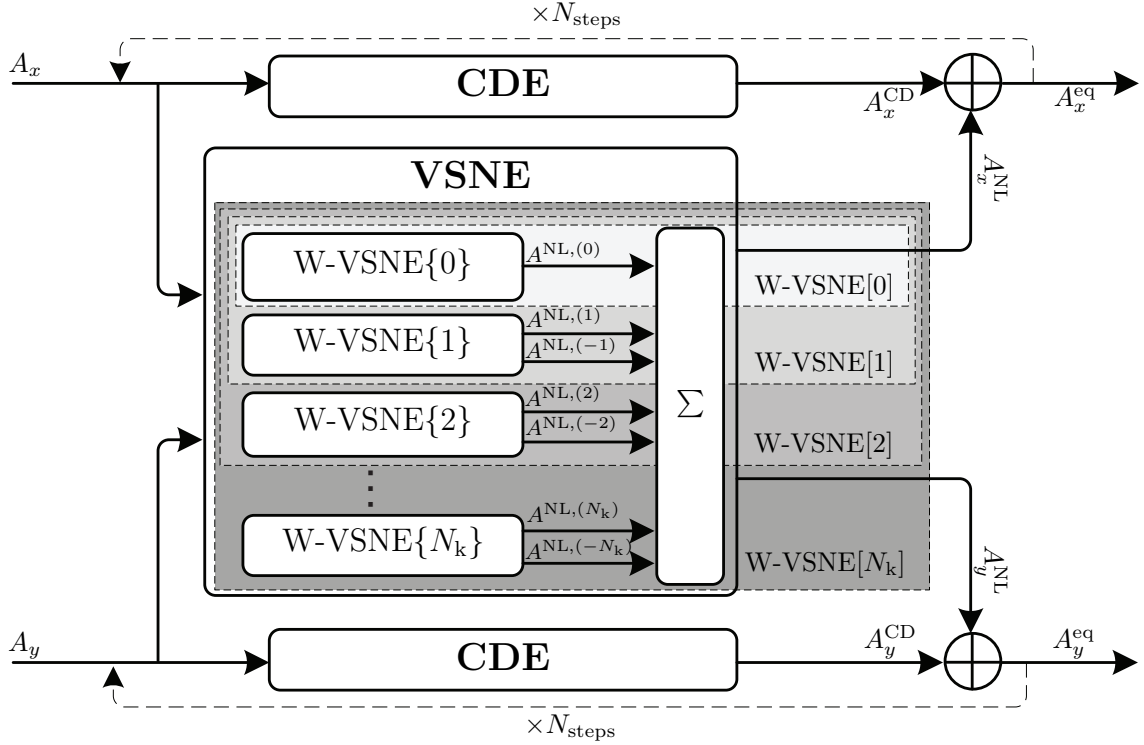


Figure 3.5: Block diagram depicting the implementation of the W-VSNE-based DBP approach. The final equalized signal is obtained after applying it a given number of iterations, N_{steps} .

Finally, it is important to point that the P-SSFM, proposed in [33] and experimentally validated in [22], matches a simplification of the W-VSNE-based DBP technique, where the CDE is applied in parallel with a single nonlinear branch, i.e., the $\text{W-VSNE}[0]$ filter. The P-SSFM name was attributed due to the fact that, similarly to the SSFM, the P-SSFM is based on the separate application of the linear and nonlinear steps, being in this case implemented in a parallel structure, contrary to the SSFM where the linear and nonlinear steps are implemented in a serial structure.

Note that the $\text{W-VSNE}[0]$ complexity per step is approximately equivalent to the standard and weighted SSFM. The inclusion of an adjustable power weighting time window does not imply any additional complexity. However, each K -th TD filter brings additional complexity relatively to the zeroth-order filter, due to the fact that each filter is composed by two individual filters and also the exponential function presented in equation (3.22) [21]. However, the W-VSNE can be advantageous from an hardware implementation point of view, since it avoids the use of the exponential operator in the

nonlinear branch, reducing its complexity. Moreover, since it is based on a perturbative approach, where the linear and nonlinear steps are partially applied in parallel, it provides a reduction of the algorithm latency [21].

The W-VSNE was numerically assessed for a 224 Gbit/s PM-16QAM transmission system, showing an improved performance/complexity tradeoff over SSFM [21]. In the following section we experimentally evaluate the performance of the W-VSNE algorithm in a 400G superchannel-based transmission system, against the above mentioned SSFM-based DBP techniques.

3.3 400G WDM Transmission System

In this section, we describe the experimental setup and the set of DSP algorithms used in the experimental validation of the SSFM, W-SSFM and W-VSNE-based DBP techniques. This work was carried out in collaboration with Centro de Pesquisa e Desenvolvimento em Telecomunicações (CPqD), Campinas, São Paulo, Brazil. The raw experimental data presented here was collected in the laboratorial facilities of CPqD, while the DSP implementation was performed offline in Matlab, at Instituto de Telecomunicações, in Aveiro, Portugal.

3.3.1 Experimental setup

A simplified scheme of the laboratorial setup implemented in this work is shown in Figure 3.6. At the transmitter side, each WDM optical subcarrier is generated by 10 external cavity lasers (ECLs) with a linewidth of 100 kHz, and modulated by a dual-polarization MZM. The WDM comb centered at 1550 nm is composed of five 400G superchannels consisting of two PM-16QAM carriers modulated at 31.5 Gbaud, thus generating a total data-rate of 504 Gbit/s. Each superchannel is assigned to a 75 GHz flexgrid slot, yielding a net SE of 5.33 bits/s/Hz. The bit data stream is coded in 16QAM symbols, upsampled to match the digital-to-analog converter (DAC) sampling rate and filtered by a raised-cosine filter with a roll-off factor of 0.1, for Nyquist pulse shaping. Additionally, a digital pre-emphasis filter is applied aiming to partially compensate for the analog bandwidth limitations. The analog I and Q components for both x and y polarizations are then generated by a 4-channel 8-bit DAC operating at 63 Gsamp/s and with an electrical bandwidth of 14 GHz. The DAC electrical outputs are finally fed into the dual-polarization in-phase and quadrature modulator (DP-IQM) for optical modulation.

The generated 400G superchannels are then sent to an optical recirculating loop, composed of 5×50 km spans of fiber, erbium-doped fiber amplifiers (EDFAs) and controlled by two acousto-optical switches (AOS). To decrease the amount of fiber nonlinearities and improve the system OSNR, fibers with a higher effective area or reduced attenuation factor are used. In this setup, we use the ultra-low-loss (ULL) fibers Corning EX2000, characterized by an α of 0.162 dB/km, dispersion slope (D) of 20.4 ps/(nm·km) and effective area (A_{eff}) of 112 μm^2 . The fiber losses are compensated by EDFAs with a noise figure of 6 dB, placed at the end of each fiber span. Before the coherent receiver,

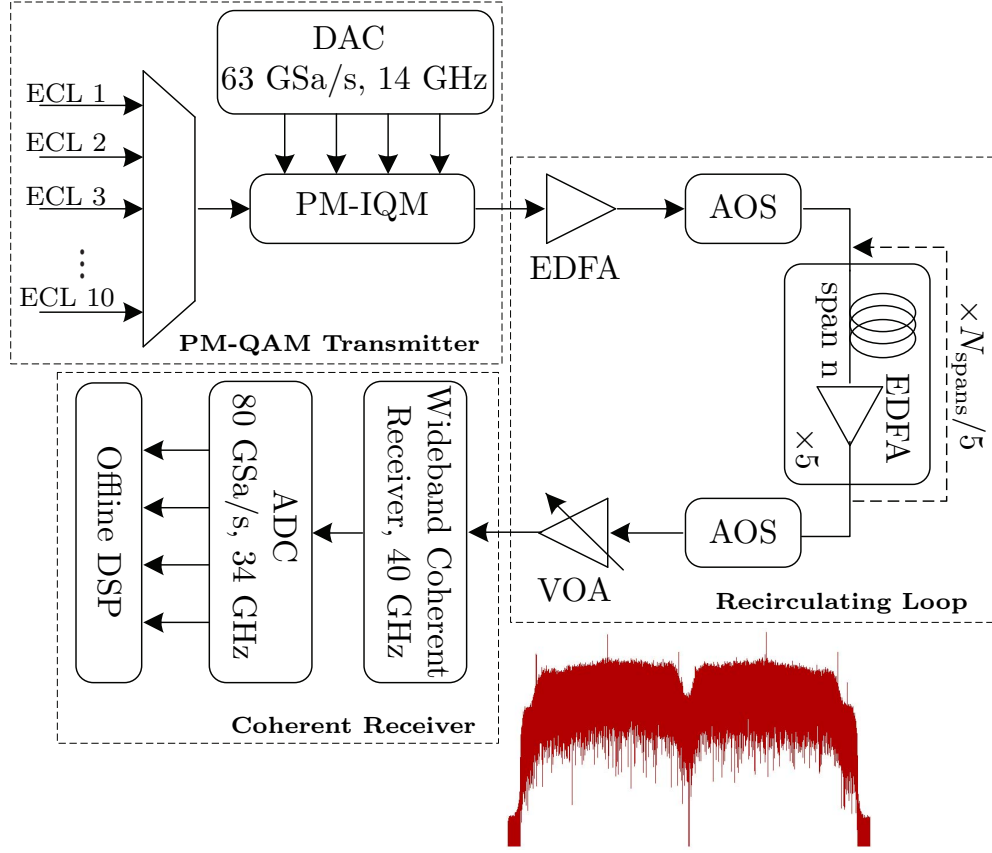


Figure 3.6: Laboratorial setup of an ultra-long-haul WDM transmission system composed of 5 dual-carrier PM-16QAM 400G superchannels (2×31.5 Gbaud). The spectrum of the received dual-carrier superchannel signal is shown in the inset figure.

an optical pre-amplifier and a variable optical attenuator (VOA) are used to control the optical power of the photodiodes.

At the receiver side, a wideband polarization and phase diversity coherent receiver with an electrical bandwidth of 40 GHz is used to detect the dual-carrier superchannel signal. The spectrum of the received signal is shown in the inset figure. Initially, the signal is separated into two orthogonal polarizations via a polarization beam splitter (PBS). Each polarization is mixed with a free-running LO in a 2×4 90° optical hybrid, to obtain the signal in a near zero frequency. The output signals of the optical hybrid for each polarization are then sent to a pair of balanced photodiodes for optical-electrical conversion. The electrical I and Q signals are afterwards digitized by a 80 Gsmp/s real-time sampling LeCroy oscilloscope with an analog bandwidth of 34 GHz, and saved for posterior offline processing in MATLAB. The DSP algorithms used for offline processing are described in the following section.

3.3.2 Digital signal processing

The sequence of post-detection DSP algorithms used in this work is depicted in Figure 3.7.

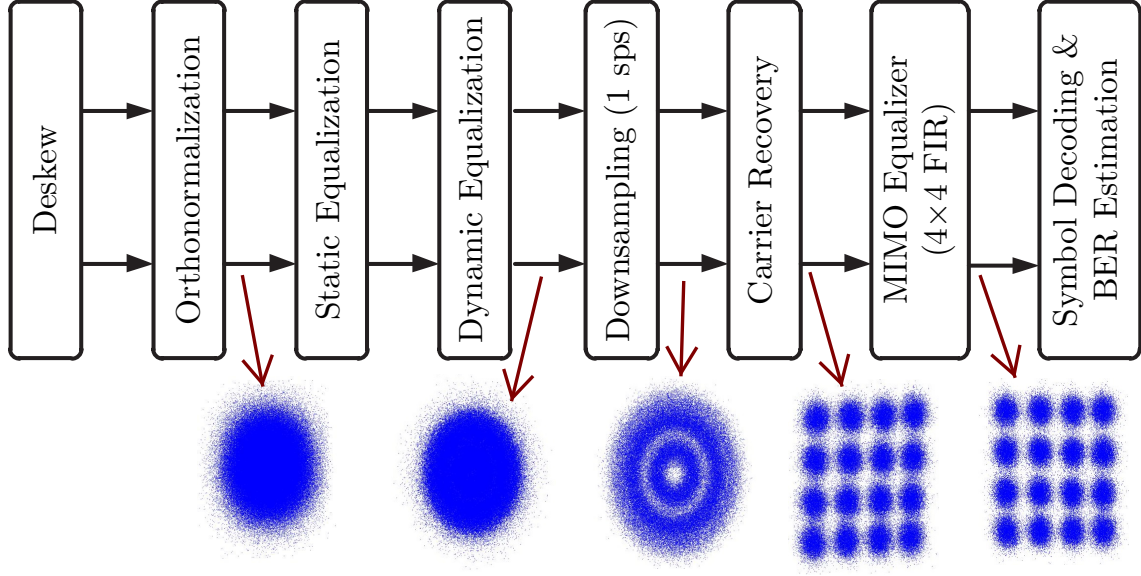


Figure 3.7: Sequence of post-detection DSP algorithms employed in this work for processing of the dual-carrier PM-16QAM 400G superchannels. The constellations along the optical path for one of the signal polarizations are also depicted, where the effect of the DSP algorithms is clearly visible.

Post-detection DSP starts with the correction of the optical front-end imperfections, such as the I and Q output signals time skew and quadrature imbalance between them. Such imperfections are removed by using the deskew algorithm proposed in [34] and the Gram-Schmidt orthonormalization procedure proposed in [36], respectively. Afterwards, each individual superchannel carrier is selected by means of band-pass filtering and downconverted to baseband, followed by resampling which is applied to adjust the sampling rate to 2 samples per symbol.

As mentioned before, coherent receivers enable the equalization of the fiber transmission impairments in the digital domain. Therefore, a static equalization block can be applied in order to compensate for deterministic effects, such as CD and nonlinear effects. The remaining non-deterministic and randomly evolving effects, such as PMD, PDL and residual amounts of deterministic effects, can be compensated in a dynamic equalization block which uses MIMO-based FIR filters. In this chapter, the static equalization block comprises linear CDE or intra-channel NLE. Where the linear CDE is applied in time-domain by means of a finite impulse response (FIR) filter, while the intra-channel NLE is achieved by means of the SSFM, W-SSFM or W-VSNE-based DBP. The dynamic equalization and polarization demultiplexing is achieved with a bank of complex 2×2 FIR filters with 31 taps, driven by a multi-radii constant modulus algorithm (CMA) for the feedback error function [14, 37].

After downsampling to 1 sps, the signal is fed into the carrier recovery subsystem, which aims to compensate for the frequency offset and phase noise between the received signal and the free-running LO laser that might be present due to the lack of phase/frequency lock between the transmitter and receiver lasers. In this work, the

carrier recovery subsystem is based on a 4th-order spectral-based frequency estimation [38, 39] and a modified Viterbi-Viterbi phase estimation [37, 40].

At the end of the DSP chain an additional 25-taps decision-directed 4×4 equalizer, with separate treatment of I and Q components of the signal is applied to fine tune the linear adaptive equalizer and compensate for residual IQ skew [41]. Finally, symbol demapping followed by bit-error rate (BER) calculation is performed. The BER was individually calculated for each superchannel carrier over 2¹⁹ received bits. The final BER values presented in the following sections refer to the centered superchannel BER, obtained by averaging the individual superchannel carriers BERs.

3.4 Digital Backpropagation Optimization

Before going through the analysis of the algorithms performance, each DBP-based NLE algorithm was optimized in order to achieve the respective best point of operation. In this section, we evaluate the performance of the SSFM, W-SSFM and W-VSNE algorithms as a function of the N_{NL} , which defines the number of samples used for the power-weighted average, and ξ , which is the nonlinear DBP optimization parameter. The parameters optimization procedure can be divided in two stages:

1. In the first step, a wide range of N_{NL} values is tested, while considering an empirical value for the ξ parameter;
2. In the second step, the N_{NL} values that yield the maximum NLE performance of each algorithm is retained, while the ξ parameter is optimized by varying it between 0 and 1, in steps of 0.1.

Figure 3.8 shows an example of the N_{NL} and ξ optimization procedure for the W-VSNE, when propagating with an optical power of -1 dBm through 5000 km of optical fiber. In this figure, we show the results for the zeroth order branch of the W-VSNE, i.e. W-VSNE{0}, for different considered step-sizes. The minimum considered DBP step-size is of 50 km, corresponding to 1 step per span, while the maximum considered DBP step-size is of 5000 km, corresponding to 1 step for the total fiber length. Initially ξ is set to 0.5, and after determining the optimum N_{NL} (left-hand side of the figure), this optimal N_{NL} value is considered for the ξ optimization (right-hand side of the figure). The obtained results show that the optimization of the N_{NL} enables a significant enhancement of the nonlinear equalization performance. It can be observed that the optimum N_{NL} tends to increase with the DBP step-sizes, which is expected due to the higher accumulated CD that has to be compensated in each step, and which is causing a significant spread in time of the interaction between linear and nonlinear effects. On the other hand, smaller step-sizes lead to a reduced amount of accumulated CD that has to be compensated in each step. Consequently, the interaction between dispersive linear and instantaneous nonlinear effects is less significant, and hence the optimum N_{NL} is also reduced. However, we can also see that when the N_{NL} is significantly increased, the performance of the algorithms is degraded since we are averaging the optical power, and therefore the nonlinear interactions are lost. After performing the N_{NL} optimization,

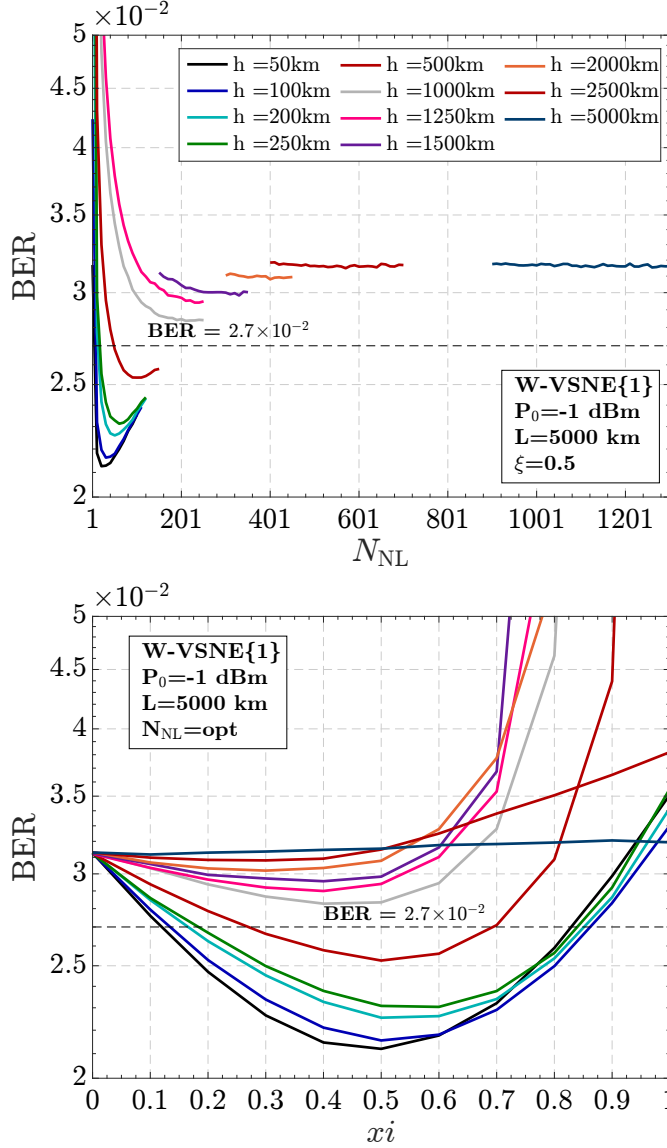


Figure 3.8: Two stages N_{NL} and ξ parameters optimization for W-VSNE{0} algorithm, when considering an input power of -1 dBm, a propagation distance of 5000 km and the set of step-sizes considered in the evaluation of the algorithm.

we proceed to the ξ optimization. It can be observed that the optimum ξ values tend to decrease for higher step-sizes, due to the DBP inaccuracy that arises with large step-sizes. Note that, although not shown here for simplicity, similar N_{NL} and ξ optimizations were individually carried out for each of the input optical powers considered in this work (ranging from -4 dB to 1 dB, in steps of 1 dB).

The above procedure was repeated for the remaining DBP-based NLE algorithms considered in this work, and a comparison between algorithms is performed in Figure 3.9 and 3.10. We must refer that, in contrast with the W-SSFM and the W-VSNE approaches, the SSFM requires only the ξ optimization procedure, since it inherently

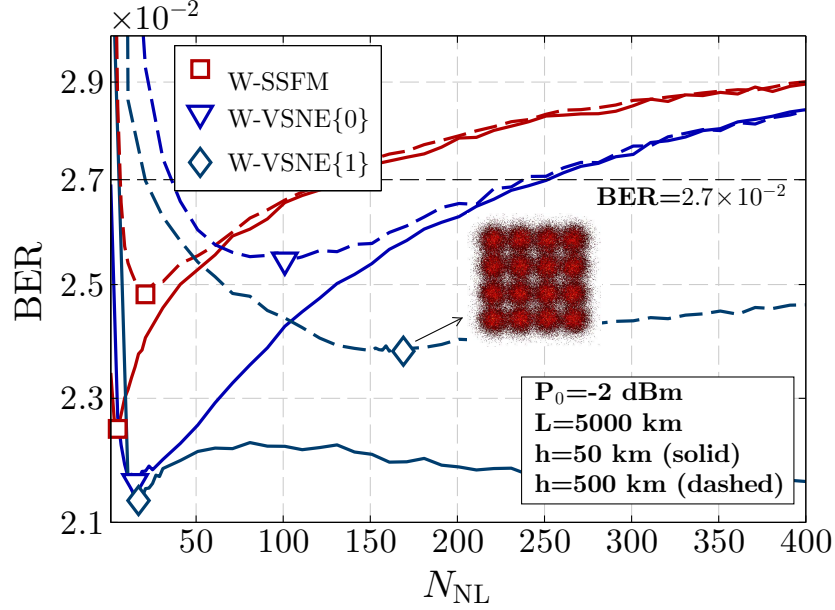


Figure 3.9: N_{NL} optimization for W-SSFM and W-VSNE algorithms, considering an input power of -2 dBm, a propagation distance of 5000 km and a DBP step-size of 50 km (solid curve) and 500 km (dashed curve).

implies $N_{NL}=1$. The SSFM accounts only for the instantaneous signal power, therefore it does not include any memory in the nonlinear step of the algorithm. On the opposite side, in the case of the W-VSNE, the two optimization stages have to be repeatedly executed for the set of N_k W-VSNE parallel filters being considered. For each implemented parallel filter the ξ and N_{NL} are optimized and the optimal values are retained for the experimental performance evaluation. As an example, the N_{NL} optimization for the W-VSNE{1} filter is obtained considering the overall BER performance for the W-VSNE[1] filter. This means that we optimize the W-VSNE{0} branch and then we retain the optimum N_{NL} and ξ parameters to performed the N_{NL} optimization for the W-VSNE{1} branch. It must also be referred that along this work, we consider a rectangular window profile for the power weighting of both W-SSFM and W-VSNE.

Figure 3.9 presents the N_{NL} optimization for the W-SSFM and W-VSNE algorithms, for an input power of -2 dBm, a total fiber length of 5000 km and a DBP step-size (h) of 50 km (solid line) and 500 km (dotted line), corresponding to 1 and 10 spans per DBP steps, respectively. Initially, we have considered $\xi = 0.5$ for the W-SSFM and W-VSNE{0}, and $\xi = 0.2$ for the W-VSNE{1}, since it is known that the benefits associated with the added W-VSNE{K} filters tend to vanish for small values of K [21]. The optimum N_{NL} obtained for each step-size and NLE method is marked in Figure 3.9. From the figure we can see that the W-VSNE tends to require larger memory values than the W-SSFM, which is due to the fact that the first is derived from a Volterra series model, which inherently consider the existence of a memory in the linear/nonlinear steps. On the other hand, the W-SSFM is originally obtained from a memoryless nonlinear operator, thereby it tends to required a smaller depth for the memory. In addition, the introduction

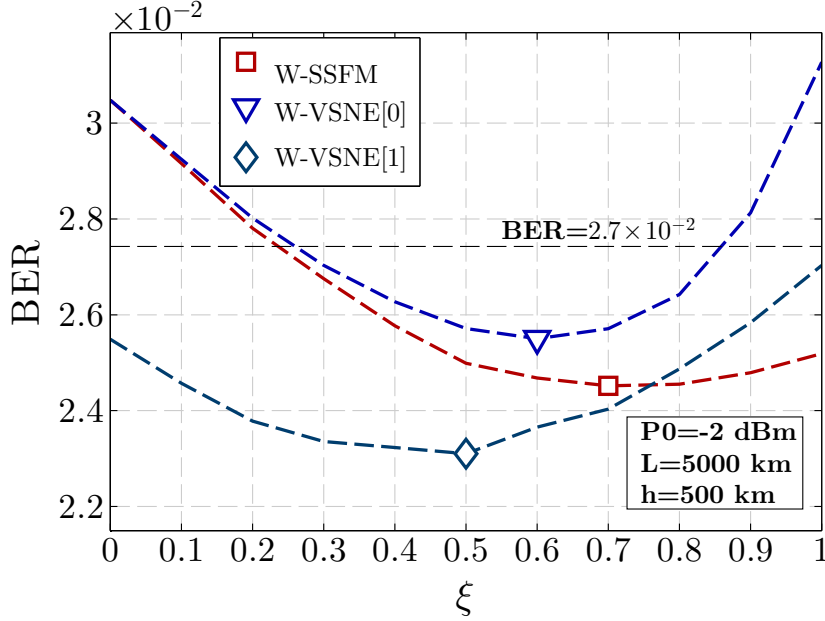


Figure 3.10: ξ optimization for W-SSFM and W-VSNE algorithms, considering an input power of -2 dBm, a propagation distance of 5000 km and a DBP step-size 500 km.

of an additional W-VSNE $\{K\}$ filter, for larger step-sizes, tend to significantly improve the W-VSNE $\{0\}$ performance, confirming its capability to capture longer-term nonlinear effects.

Retaining the optimum N_{NL} for each DBP method, we proceed to the ξ optimization. Figure 3.10 presents the ξ optimization for the W-SSFM and W-VSNE algorithms, for an input power of -2 dBm, a total fiber length of 5000 km and a DBP step-size of 500 km. We can see that the optimum ξ value for the W-VSNE $\{0\}$ is lower than that of W-SSFM, this might be due to the fact that it is a single filter from an array of N_k complementary filters, whose outputs are summed together. Moreover, the optimum ξ value drops for increasing K -th filters, showing that the added benefit of W-VSNE $\{K\}$ filters tends to vanish for relative small values of K .

The previous results confirm that the optimization of N_{NL} and ξ strongly benefit the system performance. After, N_{NL} and ξ optimizations and for a step-size of 500 km, the optimum BER values obtained for W-SSFM, W-VSNE $\{0\}$ and W-VSNE $\{1\}$ are $\sim 2.44 \times 10^{-2}$, $\sim 2.53 \times 10^{-2}$ and $\sim 2.33 \times 10^{-2}$, respectively. Finally, we can conclude that the results presented in this section are in accordance with the previous numerical results reported in [21].

3.5 Experimental Performance Analysis

After N_{NL} and ξ parameters optimization, we proceed to the performance assessment of the DBP algorithms employing the previously mentioned numerical methods. In this section, we focus our analysis on the DBP-based on SSFM, W-SSFM and W-VSNE,

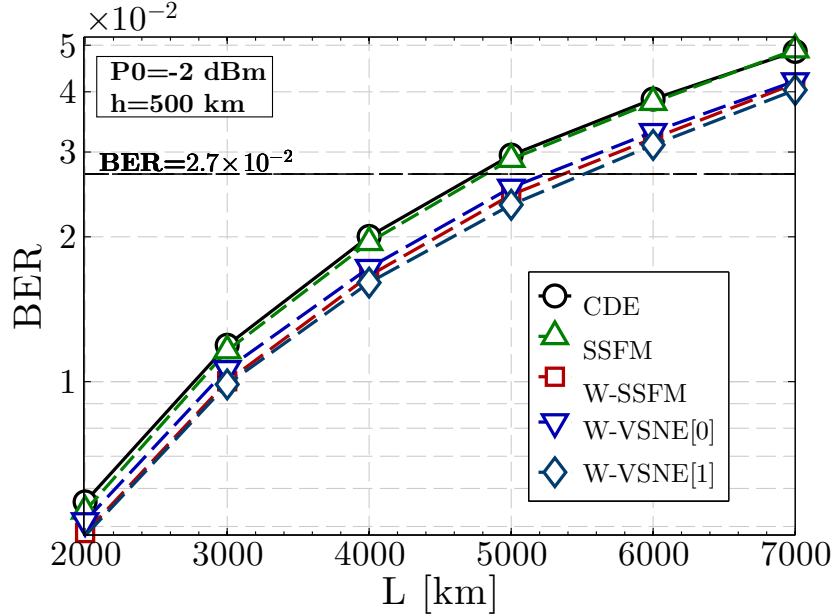


Figure 3.11: Performance of the linear and nonlinear equalization algorithms: BER as a function of the transmission distance, when considering a fixed DBP step-size of 500 km and an input power of -2 dBm.

aiming to experimentally assess and identify the potential benefits of each algorithm.

We start our analysis by evaluating the performance of each algorithm, in terms of BER as a function of the transmission distance. In Figure 3.11 we show the results obtained for an input power of -2 dBm, a fixed DBP step-size of 500 km and transmission distances ranging from 2000 km up to 7000 km, in steps of 1000 km. Note that, we consider the optimized parameters obtained for a transmission distance of 5000 km as the optimum values for all the other transmission distances considered in this chapter. Considering a BER threshold of 2.7×10^{-2} for a typical 20% overhead SD-FEC, we can see that the transmission distance of 5000 km can only be achieved using the W-SSFM or W-VSNE algorithms, since the system performance after CDE and SSFM is limited to a BER of $\sim 3 \times 10^{-2}$, which is above the FEC limit considered here. Under this scenario, the standard SSFM brings only a marginal gain over CDE, owing to the large step-size being considered ($h = 500$ km). In contrast, the W-SSFM algorithm shows a significant gain over CDE, enabling an extended reach of approximately 600 km. On the other hand, the system performance of W-VSNE[0] and W-VSNE[1] proves to be comparable to the W-SSFM. Despite W-VSNE[0] shows to be slightly worse than W-SSFM, the W-VSNE[1] provides the best performance for all the propagation distances considered in Figure 3.11. The same analysis was carried out for optical input powers ranging from -4 dBm up to 1 dBm, in steps of 1 dBm, from where similar conclusions were observed.

From the previous results, we can determine the maximum reach for each equalization method as a function of the input power, which is depicted in Figure 3.12. The estimated maximum reach was obtained by performing a spline interpolation of the measured BER versus transmission distance results (see Figure 3.11) into multiples of

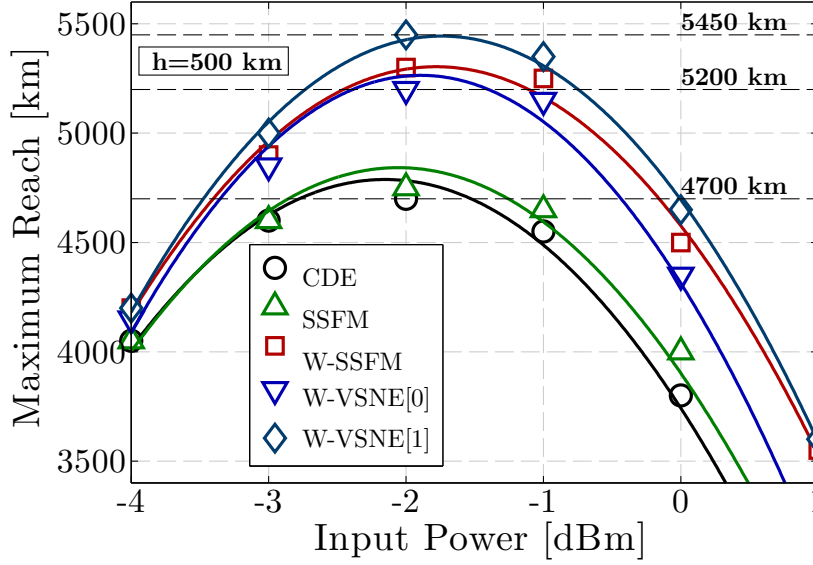


Figure 3.12: Estimated maximum reach as a function of the input power, considering a fixed step-size of 500 km, for the different static equalization algorithms.

the span length (50 km). For the optimum input power of -2 dBm and an DBP step-size of 500 km, corresponding to a total of 10 spans per step, the maximum reach enabled by CDE is 4700 km. When intra-channel NLE is considered this distance can be increased up to 5200 km with the W-VSNE[0], 5300 km with the W-SSFM, and 5450 km with the W-VSNE[1], corresponding to a gain of $\sim 11\%$, $\sim 13\%$ and $\sim 16\%$ over CDE, respectively.

The previous analysis was extended for several DBP step-sizes, ranging from 12.5 km (i.e. 4 steps per span) up to 5000 km (i.e. 100 spans per step), aiming to determine the best tradeoff between performance and computational effort for each NLE method. The obtained results showing the estimated maximum reach as a function of the DBP step-size are presented in Figure 3.13. From the observation of this figure, three main regions of operation can be defined:

- a high complexity region, where the system reach can be increased around 1000 km, at the cost of a large number of DBP steps required and therefore high complexity ($h \leq 100$ km);
- a medium complexity region, where a significant reach gain, between 1000 km and 500 km, can be achieved while using DBP step-sizes of several spans per step ($100 < h \leq 1000$ km);
- a low complexity region, where the reach improvement is lower than 500 km, although DBP is applied with a lower complexity using very large step-sizes ($h > 1000$ km).

As expected, the results of Figure 3.13 show that the standard SSFM algorithm is not adequate for low-complexity DBP, since its performance tends to quickly degrade

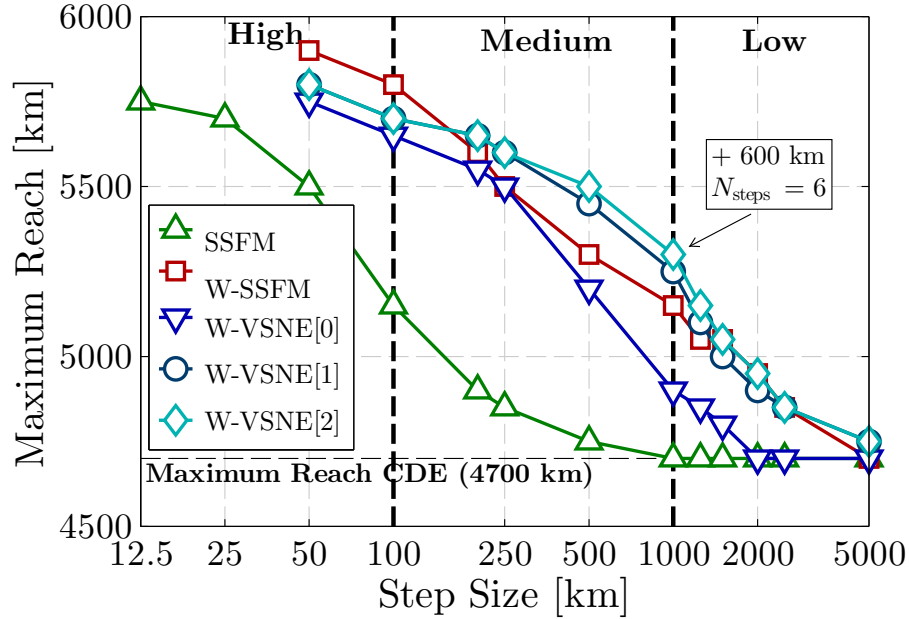


Figure 3.13: Estimated maximum reach as a function of the DBP step-size, for CDE, SSFM, W-SSFM and W-VSNE methods.

for step-sizes larger than the fiber span length. This occurs due to the fact that this algorithm was originally developed for high accuracy modeling of signal propagation in fiber. Contrarily, it is shown that both the W-VSNE and the W-SSFM algorithms are able to tolerate much longer step-sizes without severely compromising the system performance. In the high complexity region, these algorithms are able to reach approximately the same performance as the SSFM while using about $4\times$ fewer DBP steps, demonstrating its capability to work at high performance with significantly lower complexity than the standard SSFM. In addition, note that the additional reach provided by the W-VSNE[1] over W-VSNE[0] is only 50 km in the high performance region, not justifying the additional complexity. The reach enhancement of the W-VSNE over the SSFM is further increased within the medium complexity region, enabling up to 750 km of extended reach (more $\sim 15\%$) for a DBP step-size between 200 km and 500 km, which corresponds to approximately 25 and 10 DBP steps in total, respectively. In this region, the W-VSNE[1] always surpasses the W-SSFM achieving a maximum reach gain of 150 km for a DBP step-size of 500 km. The benefit of the additional W-VSNE{1} filters starts to be worthwhile for step-sizes larger than 250 km. For $h=1000$ km (20 spans per step), the extended reach provided by the W-VSNE[1] over W-VSNE[0] is of 350 km, which may justify the added complexity of the W-VSNE{1} parallel filter. Furthermore, when using only 6 DBP steps for the entire link, the W-VSNE[1] yields 550 km and 150 km of added reach over CDE and W-SSFM respectively, whereas the standard SSFM gain converges already to zero. To achieve the same reach gain using the SSFM, a total of 50 DBP steps will be required, increasing the system complexity in $\sim 90\%$. Finally, in the low-complexity region, an extended reach of 400 km over CDE can be obtained with a low-complexity 5-steps W-VSNE[1], enabling a $10\times$ reduction in the computational effort comparing to

SSFM. In the limit of a 2-steps NLE the estimated extended reach is of 150 km, while the complexity is only approximately $2\times$ larger than that of the simple CDE. Finally, is important to refer that the addition of the W-VSNE{2} filter is not worthwhile, since it provides a small improvement of only 50 km in the maximum extended reach. This results are in accordance with the numerical results reported in [21], where it is shown that the system performance for the W-VSNE saturates for $K \geq 2$.

3.6 Computational Effort

Besides performance, another factor that must be taken into account when selecting an algorithm is the associated computational effort. In this section, we analyze the complexity and latency of the NLE algorithms considered in this work, which are calculated based on the expressions derived in the subsection II.D and III.C of [21]. The complexity is here defined in terms of required number of real multiplications (RMs) per sample, N_{RMs} , while the latency is defined in terms of number of serial real multiplications, τ_{RM} . Note that, it is considered that each complex multiplication can be decomposed into four RMs.

From the analyze of equation (3.15), (3.16) and (3.17), we can conclude that the W-VSNE{0} filter branch requires a total of 20 RMs per step. The power weighting terms require a total of 8 RMs per processed sample: $P_{xx/yy}$ requires 2 RMs per polarization; P_{xy} requires 4 RMs, while P_{yx} is obtained from the complex conjugate of P_{xy} . To compute the multiplication of the power weighting terms with the linear term, $A_{x/y}^{\text{CD}}$, a total of 12 RMs per sample are required ($A_{x/y}^{\text{CD}}[2P_{xx/yy} + P_{yy/xx}]$ requires 2 RMs per polarization, while $A_{x/y}^{\text{CD}}P_{xy/yx}$ requires 4 RMs per polarization). The remaining W-VSNE{K} filter branches require a total of 52 RMs per processed sample, from which 20 RMs are required for the calculation of the power weighting terms and 32 RMs are due to the multiplication by $A_{x/y}^{\text{CD},(\pm K)}$. Note that, each W-VSNE{K} filter is composed of two individual filters. The extra complexity of W-VSNE{K} over W-VSNE{0} is due to the exponential function present in expressions (3.21) and (3.22), this added complexity can be avoided by decomposing the exponential factor into a simple power-of-two approximation. With such approach all the multiplications can be decomposed into efficient shift-and-add operations and the W-VSNE{K} filter branches complexity can be reduced to 40 RMs, where all RMs required by the exponential factor were eliminated. Thus, in each iteration, the number of RMs per sample required by the W-VSNE[N_k] filter array is given by

$$N_{\text{RM}_{\text{W-VSNE}}}^{\text{NL}}(N_k) = 20 + 4 + 40N_k, \quad (3.23)$$

where the extra 4 RMs per iteration are due to the multiplication by κ . In order to avoid replication of operations, we have moved the κ coefficient out from the individual filters, so that it multiplies by the entire W-VSNE[N_k] output, $A_{x/y}^{\text{NL},(N_k)}$.

The complexity required by the parallel CDE will depend on the method considered for equalization. Assuming a frequency-domain implementation, a contributor for the complexity increase is the calculation of the $A_{x/y}^{\text{CD},(\pm K)}$ terms in frequency-domain.

3.6. Computational Effort

To avoid the additional CD transfer functions and IFFTs, the following time-domain approximation is applied [21]

$$A_{x/y}^{\text{CD},K}(t_n) = A_{x/y}^{\text{CD}}(t_{n+d_{\text{opt}}}) \exp(i(2\pi t K + \phi_{\text{opt}})), \quad (3.24)$$

where d_{opt} and ϕ_{opt} are scalar optimization parameters. This together with the power-of-two approximation for the exponential factor enables us to obtain $A_{x/y}^{\text{CD},\pm K}(t_n)$ directly from $A_{x/y}^{\text{CD}}(t_{n\pm d_{\text{opt}}})$, avoiding the use of extra RM operations. In [21] it was shown that these two approximations have a negligible impact on the W-VSNE system performance. Therefore after disregarding the overlap-and-save operation, the CDE complexity per step is given by

$$N_{RM_{W-VSNE}^{\text{CDE}}}(N, N_k) = N_{RM_{W-VSNE}^{\text{CDE}}}(N, 0) = 2[4 + N_{RM_{FFT}}(N)], \quad (3.25)$$

where $N_{RM_{FFT}}(N) = 2 \log_2(N_{FFT})$ accounts for the FFT/IFFT complexity and the factor 4 accounts for the multiplication of the signal by the CD transfer function. The factor of 2 accounts for the two polarizations, which are independently processed.

The overall complexity of the optimized W-VSNE algorithm is given by

$$N_{RM_{W-VSNE}^{\text{DBP}}}(N_k, N) = N_{\text{steps}}[N_{RM_{W-VSNE}^{\text{NL}}}(N_k) + N_{RM_{W-VSNE}^{\text{CDE}}}(N, 0)]. \quad (3.26)$$

In terms of latency, the W-VSNE benefits from the fact that the linear and nonlinear branches are partially applied in parallel. Only 2 RM blocks are applied after obtaining the CDE output (1 RM in the W-VSNE{K} and 1 RM to multiply by κ). Given this, the latency of the W-VSNE algorithm is quantified as

$$\tau_{RM_{W-VSNE}^{\text{DBP}}} = N_{\text{steps}}(\tau_{RM_{CDE}} + 2), \quad (3.27)$$

where $\tau_{RM_{CDE}} = 2 \log_2(N_{FFT}) + 1$ corresponds to the latency associated with each CDE step, with $2 \log_2(N_{FFT})$ accounting for the latency of the FFT and IFFT. Note that, we assumed that the latency of the CDE step is always larger than the latency of the NLE filter branches.

Focusing now in the SSFM analysis, the implementation complexity associated with its nonlinear step can be determined from equation (3.10). The power of two terms, $A_{x/y}^{\text{CD}}$, require 2 RMs per polarization, the multiplication by κ requires 1 RM and the complex multiplication of $A_{x/y}^{\text{CD}}$ by the exponential function requires 4 RMs also per polarization. The exponential function brings some additional complexity. It can be based on a fourth order Taylor expansion, implying 6 RMs, or alternatively it can be implemented using look-up-tables (LUTs), which does not require any RM. Since we are looking for the less complex implementation, the LUT-based SSFM is considered. Given this, the overall complexity required by the nonlinear operator in each iteration is $N_{RM_{SSFM}^{\text{NL}}} = 13$. Finally, considering again a frequency-domain implementation of the linear step, the total number of RMs required by the SSFM algorithm is given by

$$N_{RM_{SSFM}^{\text{DBP}}}(N) = N_{\text{steps}}[N_{RM_{SSFM}^{\text{NL}}} + N_{RM_{SSFM}^{\text{CDE}}}(N, 0)]. \quad (3.28)$$

Table 3.1: Complexity and latency of DBP based on the SSFM, W-SSFM and W-VSNE as function of the transmission distance.

Distance (km)		5700	5500	5150	4900
SSFM	N_{FFT}	512	512	1024	1024
	N_{steps}	228	110	52	25
	N_{RMs}	21204	10230	5252	2525
	τ_{RM}	5244	2530	1300	625
W-SSFM	N_{FFT}	1024	1024	2048	8192
	N_{steps}	38	22	6	3
	N_{RMs}	3838 (-82%)	2222 (-78%)	654 (-88%)	375 (-85%)
	τ_{RM}	950 (-82%)	550 (-78%)	162 (-88%)	93 (-85%)
W-VSNE[0]	N_{FFT}	512	1024	2048	2048
	N_{steps}	82	22	9	5
	N_{RMs}	8528 (-60%)	2464 (-76%)	1080 (-80%)	600 (-76%)
	τ_{RM}	1722 (-67%)	506 (-80%)	225 (-83%)	125 (-80%)
W-VSNE[1]	N_{FFT}	1024	2048	2048	8192
	N_{steps}	57	14	5	3
	N_{RMs}	8664 (-60%)	2240 (-80%)	800 (-85%)	528 (-80%)
	τ_{RM}	1311 (-75%)	350 (-86%)	125 (-90%)	87 (-86%)

From the above equation we can conclude that the W-VSNE[0] and W-SSFM algorithms are approximately equivalent from the complexity point of view.

Regarding latency, since the linear and nonlinear operators are implemented in a serial configuration, the SSFM algorithm latency can be defined as

$$\tau_{\text{RM}_{\text{SSFM}}^{\text{DBP}}} = N_{\text{steps}}(\tau_{\text{RM}_{\text{CDE}}} + \tau_{\text{RM}_{\text{exp}}}), \quad (3.29)$$

with $\tau_{\text{RM}_{\text{exp}}} = 4$ being the latency required by the nonlinear phase rotation, where it is considered that the latency associated with the LUT implementation is similar to a RM implementation. The complexity and latency of the W-SSFM is also given by equations (3.28) and (3.29). Since we are using a rectangular window for the nonlinear step memory the length of the time window can be easily manipulated in hardware using an accumulator block, therefore not implying any additional complexity.

Table 3.1 presents the complexity and latency associated to the SSFM, W-SSFM, W-VSNE[0] and W-VSNE[1] algorithms as a function of the transmission distance. In the table, N_{FFT} represents the minimum FFT block length required for the implementation of the linear step without inter-block interference [19]. The number of steps, N_{steps} , is obtained from the quotient between the transmission distance and the DBP step-size, obtained from Figure 3.13. The values required for the implementation of the SSFM method are used as a benchmark for the calculation of the complexity and latency gains of the remaining algorithms. In accordance with the previous numerical results, Table 3.1 shows that the SSFM typically requires high N_{steps} , consequently imposing a high N_{RMs} and τ_{RM} , diffculting its hardware implementation. On the other hand, both W-VSNE and W-SSFM algorithms allow significant complexity savings, e.g., for a transmission distance of 5700 km (1000 km over the CDE limit), the W-VSNE enables

a complexity reduction of $\sim 60\%$ and $\sim 70\%$ in terms of N_{RMs} and τ_{RM} , respectively, when compared with the SSFM. The complexity reduction enabled by the W-VSNE is further enhanced up to $\sim 90\%$ as we reduce the required extended reach provided by DBP, moving to regions of medium and low complexity where practical implementation becomes more feasible. Similarly to the W-VSNE, the W-SSFM enables a complexity reduction of $\sim 80 - 90\%$. Note that, although the W-VSNE tends to require a slightly higher N_{RMs} than W-SSFM, its latency will be typically lower, since the W-VSNE is based on the parallel application of the linear and nonlinear steps. Regarding the single step implementation of CDE, the minimum FFT block length is 8192. Taking this into account, the application of CDE in the frequency-domain requires 112 N_{RMs} per sample with $\tau_{\text{RM}} = 27$ [21]. Analyzing the table we can verify that, the added complexity of the SSFM, W-VSNE and W-SSFM over CDE tends to increase proportionally with the number of DBP steps.

In addition to this results, the W-VSNE-based DBP presents other interesting advantages over SSFM-based DBP in terms of hardware implementation. The W-VSNE avoids the use of an exponential function on the nonlinear step and its inherent complexity. Moreover, since the W-VSNE is composed by a set of N_k parallel filters, the tradeoff between performance and computational complexity can be handled in an easier way.

3.7 Conclusions

Along this chapter, we experimentally evaluate the performance of reduced complexity versions of split-step and Volterra-based DBP techniques. These techniques are evaluated over an WDM ultra-long-haul (ULH) transmission system composed of 5 dual-carrier PM-16QAM 400G superchannels, spaced in a 75 GHz grid slot. We demonstrate that such intra-channel nonlinear equalization techniques can bring significant benefits in terms of optical reach, even when applied with a low number of DBP steps.

The performance, complexity and latency of the different algorithms is evaluated, aiming to determine the best tradeoff between them. Taking into account the complexity reduction metric, we determine operation regions of high, medium and low complexity. We demonstrate that if properly optimized, the W-SSFM and W-VSNE techniques can be applied with large step-sizes, while still providing a significant extended reach over CDE. On the other hand, the standard SSFM is shown to be inadequate for the application of DBP using large step-sizes. The recently proposed W-VSNE is found to be the most advantageous technique in the medium and low-complexity operation regions. It can, for example, enable a reach extension of 600 km over CDE, while requiring only 6 DBP steps for a total transmission reach of 5300 km. Besides, it allows a reduction of the total number of DBP steps up to 90%, a maximum reduction of 85% for the number of real multiplications, and up to 90% for the total latency comparing to the standard SSFM technique without significant performance loss.

Additionally, the W-VSNE-based DBP can bring some advantages over DBP-based on SSFM and W-SSFM from a hardware implementation point of view. The parallel application of the linear and nonlinear steps allows the reduction of the total latency

of the algorithm. Moreover, it avoids the exponential operator in the nonlinear branch and its associated complexity. In addition, since the W-VSNE is composed by a set of N_k parallel filter, the tradeoff between performance and computational complexity can be handled more easily. These advantages together with the obtained results shows the potential of the W-VSNE to be applied as an alternative low-complexity DBP technique.

References

- [1] R.-J. Essiambre, G. Kramer, P. J. Winzer, G. J. Foschini, and B. Goebel, "Capacity limits of optical fiber networks," *J. Lightw. Technol.*, vol. 28, no. 4, pp. 662–701, 2010.
- [2] R. Dar and P. J. Winzer, "On the limits of digital back-propagation in fully loaded WDM systems," *IEEE Photonics Technology Letters*, vol. 28, no. 11, pp. 1253–1256, June 2016.
- [3] K. Kikuchi, "Fundamentals of coherent optical fiber communications," *Journal of Lightwave Technology*, vol. 34, no. 1, pp. 157–179, Jan 2016.
- [4] E. Ip and J. M. Kahn, "Compensation of dispersion and nonlinear impairments using digital backpropagation," *J. Lightw. Technol.*, vol. 26, no. 20, pp. 3416–3425, 2008.
- [5] X. Li, X. Chen, G. Goldfarb, E. Mateo, I. Kim, F. Yaman, and G. Li, "Electronic post-compensation of WDM transmission impairments using coherent detection and digital signal processing," *Opt. Express*, vol. 16, no. 2, pp. 880–888, Jan 2008.
- [6] D. S. Millar, S. Makovejs, C. Behrens, S. Hellerbrand, R. I. Killey, P. Bayvel, and S. J. Savory, "Mitigation of fiber nonlinearity using a digital coherent receiver," *IEEE J. Sel. Topics Quantum Electron.*, vol. 16, no. 5, pp. 1217–1226, 2010.
- [7] E. Ip, "Nonlinear compensation using backpropagation for polarization-multiplexed transmission," *J. Lightw. Technol.*, vol. 28, no. 6, pp. 939–951, 2010.
- [8] G. Shulkind and M. Nazarathy, "Nonlinear digital back propagation compensator for coherent optical OFDM based on factorizing the Volterra series transfer function," *Opt. Express*, vol. 21, no. 11, pp. 13 145–13 161, Jun 2013.
- [9] F. P. Guiomar, J. D. Reis, A. L. Teixeira, and A. N. Pinto, "Mitigation of intra-channel nonlinearities using a frequency-domain Volterra series equalizer," *Opt. Express*, vol. 20, no. 2, pp. 1360–1369, Jan 2012.
- [10] F. P. Guiomar, J. D. Reis, A. Carena, G. Bosco, A. L. Teixeira, and A. N. Pinto, "Experimental demonstration of a frequency-domain Volterra series nonlinear equalizer in polarization-multiplexed transmission," *Opt. Express*, vol. 21, no. 1, pp. 276–288, 2013.

- [11] E. Giacomidis, I. Aldaya, M. Jarajreh, A. Tsokanos, S. T. Le, F. Farjady, Y. Jaouen, A. Ellis, and N. Doran, "Volterra-based reconfigurable nonlinear equalizer for coherent OFDM," *IEEE Photon. Technol. Lett.*, vol. 26, no. 14, pp. 1383–1386, July 2014.
- [12] S. J. Savory, G. Gavioli, E. Torrenco, and P. Poggiolini, "Impact of interchannel nonlinearities on a split-step intrachannel nonlinear equalizer," *IEEE Photon. Technol. Lett.*, vol. 22, no. 10, pp. 673–675, 2010.
- [13] G. Goldfarb, M. G. Taylor, and G. Li, "Experimental demonstration of fiber impairment compensation using the split-step finite-impulse-response filtering method," *IEEE Photon. Technol. Lett.*, vol. 20, no. 22, pp. 1887–1889, 2008.
- [14] F. Guiomar, S. Amado, A. Carena, G. Bosco, A. Nespola, A. Teixeira, and A. Pinto, "Fully-blind linear and nonlinear equalization for 100G PM-64QAM optical systems," *J. Lightw. Technol.*, vol. PP, no. 99, 2015.
- [15] E. Ip, N. Bai, and T. Wang, "Complexity versus performance tradeoff in fiber nonlinearity compensation using frequency-shaped, multi-subband backpropagation," in *Proc. Optical Fiber Communication Conf. and Exposition (OFC)*. Optical Society of America, 2011, p. OThF4.
- [16] A. Napoli, Z. Maalej, V. Sleiffer, M. Kushnerov, D. Rafique, E. Timmers, B. Spinnler, T. Rahman, L. Coelho, and N. Hanik, "Reduced complexity digital back-propagation methods for optical communication systems," *J. Lightw. Technol.*, vol. 32, no. 7, pp. 1351–1362, April 2014.
- [17] L. B. Du and A. J. Lowery, "Improved single channel backpropagation for intra-channel fiber nonlinearity compensation in long-haul optical communication systems," *Opt. Express*, vol. 18, no. 16, pp. 17 075–17 088, Aug 2010.
- [18] D. Rafique, M. Mussolin, M. Forzati, J. Mårtensson, M. N. Chugtai, and A. D. Ellis, "Compensation of intra-channel nonlinear fibre impairments using simplified digital back-propagation algorithm," *Opt. Express*, vol. 19, no. 10, pp. 9453–9460, May 2011.
- [19] F. P. Guiomar and A. N. Pinto, "Simplified Volterra series nonlinear equalizer for polarization-multiplexed coherent optical systems," *J. Lightw. Technol.*, vol. 31, no. 23, pp. 3879–3891, 2013.
- [20] J. D. Reis and A. L. Teixeira, "Unveiling nonlinear effects in dense coherent optical WDM systems with Volterra series," *Opt. Express*, vol. 18, no. 8, pp. 8660–8670, Apr 2010.
- [21] F. P. Guiomar, S. B. Amado, C. S. Martins, and A. N. Pinto, "Time domain Volterra-based digital backpropagation for coherent optical systems," *J. Lightw. Technol.*, vol. 15, no. 33, pp. 3170–3181, August 2015.

-
- [22] S. B. Amado, F. P. Guiomar, N. J. Muga, J. D. Reis, S. M. Rossi, A. Chiuchiarelli, J. R. F. Oliveira, A. L. Teixeira, and A. N. Pinto, "Experimental demonstration of the parallel split-step method in ultra-long-haul 400G transmission," in *41st European Conference and Exhibition on Optical Communication*, 2015.
 - [23] S. B. Amado, F. P. Guiomar, N. J. Muga, R. M. Ferreira, J. D. Reis, S. M. Rossi, A. Chiuchiarelli, J. R. F. Oliveira, A. L. Teixeira, and A. N. Pinto, "Low complexity advanced DBP algorithms for Ultra-Long-Haul 400 G transmission systems," *J. Lightwave Technol.*, vol. 34, no. 8, pp. 1793–1799, Apr 2016.
 - [24] F. Yaman and G. Li, "Nonlinear impairment compensation for polarization-division multiplexed WDM transmission using digital backward propagation," *IEEE Photonics Journal*, vol. 1, no. 2, pp. 144–152, 2009.
 - [25] G. P. Agrawal, *Fiber-Optic Communication Systems*. University of Rochester, New York: John Wiley & Sons, 2011.
 - [26] A. Amari, O. A. Dobre, R. Venkatesan, O. S. S. Kumar, P. Ciblat, and Y. Jaoun, "A survey on fiber nonlinearity compensation for 400 Gbps and beyond optical communication systems," *IEEE Communications Surveys Tutorials*, vol. PP, no. 99, pp. 1–1, 2017.
 - [27] D. Lavery, D. Ives, G. Liga, A. Alvarado, S. J. Savory, and P. Bayvel, "The benefit of split nonlinearity compensation for single-channel optical fiber communications," *IEEE Photonics Technology Letters*, vol. 28, no. 17, pp. 1803–1806, Sept 2016.
 - [28] P. Bayvel, R. Maher, T. Xu, G. Liga, N. A. Shevchenko, D. Lavery, A. Alvarado, and R. I. Killey, "Maximizing the optical network capacity," *Philosophical Transactions of the Royal Society of London A: Mathematical, Physical and Engineering Sciences*, vol. 374, no. 2062, 2016.
 - [29] V. Parahyba, J. Reis, S. Ranzini, E. Schneider, E. Rosa, F. Simões, J. Diniz, L. Carvalho, E. Filho, J. Oliveira, and J. Oliveira, "Performance against implementation of digital backpropagation for high-speed coherent optical systems," *Electronics Letters*, vol. 51, no. 14, pp. 1094–1096, 2015.
 - [30] F. Yaman and G. Li, "Nonlinear impairment compensation for polarization-division multiplexed WDM transmission using digital backward propagation," *IEEE Photonics Journal*, vol. 2, no. 5, pp. 816–832, 2010.
 - [31] O. V. Sinkin, R. Holzlohner, J. Zweck, and C. R. Menyuk, "Optimization of the split-step Fourier method in modeling optical-fiber communications systems," *J. Lightw. Technol.*, vol. 21, no. 1, pp. 61–68, 2003.
 - [32] F. P. Guiomar, J. D. Reis, A. L. Teixeira, and A. N. Pinto, "Digital postcompensation using Volterra series transfer function," *IEEE Photon. Technol. Lett.*, vol. 23, no. 19, pp. 1412–1414, 2011.
-

- [33] F. P. Guiomar, S. B. Amado, C. S. Martins, and A. N. Pinto, "Parallel split-step method for digital backpropagation," in *Proc. Optical Fiber Communication Conf. and Exposition (OFC)*, 2015.
- [34] T. Tanimura, S. Oda, T. Tanaka, T. Hoshida, Z. Tao, and J. C. Rasmussen, "A simple digital skew compensator for coherent receiver," in *Proc. 35th European Conf. Optical Communication (ECOC)*, 2009, pp. 1–2.
- [35] C. S. Petrou, A. Vgenis, I. Roudas, and L. Raptis, "Quadrature imbalance compensation for PDM QPSK coherent optical systems," *IEEE Photon. Technol. Lett.*, vol. 21, no. 24, pp. 1876–1878, 2009.
- [36] I. Fatadin, S. J. Savory, and D. Ives, "Compensation of quadrature imbalance in an optical QPSK coherent receiver," *IEEE Photon. Technol. Lett.*, vol. 20, no. 20, pp. 1733–1735, 2008.
- [37] I. Fatadin, D. Ives, and S. Savory, "Blind equalization and carrier phase recovery in a 16-QAM optical coherent system," *J. Lightw. Technol.*, vol. 27, no. 15, pp. 3042–3049, 2009.
- [38] A. Leven, N. Kaneda, U.-V. Koc, and Y.-K. Chen, "Frequency estimation in intradyne reception," *IEEE Photon. Technol. Lett.*, vol. 19, no. 6, pp. 366–368, 2007.
- [39] S. Hoffmann, S. Bhandare, T. Pfau, O. Adamczyk, C. Wordehoff, R. Peveling, M. Porrmann, and R. Noe, "Frequency and phase estimation for coherent QPSK transmission with unlocked DFB lasers," *IEEE Photon. Technol. Lett.*, vol. 20, no. 18, pp. 1569–1571, 2008.
- [40] A. Viterbi, "Nonlinear estimation of PSK-modulated carrier phase with application to burst digital transmission," *IEEE Trans. Inf. Theory*, vol. 29, no. 4, pp. 543–551, 1983.
- [41] M. Paskov, D. Lavery, and S. Savory, "Blind equalization of receiver in-phase/quadrature skew in the presence of nyquist filtering," *IEEE Photon. Technol. Lett.*, vol. 25, no. 24, pp. 2446–2449, 2013.

Chapter 4

Frequency-Hybrid Superchannel

In the previous chapter, a dual-carrier PM-16QAM 400G superchannel solution was proposed and experimentally evaluated. This solution is compatible with the 75 GHz grid and proved to be suitable for ultra-long-haul (ULH) transmission systems, achieving transmission distances up to 5700 km [1]. Additionally, in [2] a triple-carrier PM-64QAM 400G superchannel solution targeted for the 50 GHz grid slot was proposed and proved to be suitable for metro applications, allowing to achieve transmission distances up to 1000 km. The recent ITU-T G.694.1 recommendation [3, 4], proposes a new flexible frequency grid based on 12.5 GHz spectral granularity, opening the possibility for the development of solutions for the 62.5 GHz slot. Solutions compatible with this frequency grid slot can rely, for example, on time- or frequency-hybrid superchannel systems. However, the design of hybrid modulation transmission systems involves a new key degree of freedom – the power-ratio (PR) between modulation formats – which is strongly dependent on the transmitter operation strategy.

In this chapter, we proposed a 400G frequency-hybrid triple-carrier superchannel solution, composed of a central PM-64QAM and two edge PM-16QAM carriers, to be applied in the 62.5 GHz grid slot [5]. The proposed superchannel is experimentally assessed in a long-haul transmission system by co-propagation with other 8 similar superchannels. The optimum PR between carriers is analytically determined, in the linear and nonlinear regimes of operation for three distinct forward error correction (FEC) paradigms, using the enhanced Gaussian noise (EGN) model [6] and validated by experimental and simulation results.

The organization of this chapter is defined as follows. Initially, the configuration of the proposed 400G frequency-hybrid superchannel is described in section 4.1. The nonlinear propagation model used along this chapter is briefly introduced in section 4.2. The laboratorial setup and the DSP subsystems used in the demodulation of each superchannel carrier are described in section 4.3. Section 4.4 is devoted to the assessment of the performance of each superchannel carrier, with both linear and nonlinear equalization. Section 4.5 addresses the optimization of the PR between superchannel carriers for three distinct FEC techniques. In section 4.6, different DBP based nonlinear mitigation strategies are applied over the central superchannel of the system aiming to evaluate its impact on the optimum PR and system achievable reach. Finally, the main conclusions drawn from this chapter are summarized in section 4.7.

4.1 Superchannel Configuration

The configuration of the proposed 400G frequency-hybrid triple-carrier superchannel is depicted in Figure 4.1. Each frequency-hybrid superchannel is composed of three carriers: two PM-16QAM edge carriers and a central PM-64QAM carrier, each operating at a symbol rate of 18 GBaud and separated by 20 GHz (guard-band of 2 GHz between carriers). The entire superchannel is assigned to a grid slot of 62.5 GHz, compatible with the recently proposed 12.5 GHz spectral granularity (ITU-T G.694.1 recommendation), allowing the achievement of a net SE of 6.4 bits/s/Hz. The proposed superchannel has a gross bit-rate of 504 Gbit/s, englobing 400 Gbit/s of net bit-rate and 26% of overhead, 20% for SD-FEC and 6% for the network protocol overheads. Therefore, the system can operate a target pre-FEC BER of 2.4×10^{-2} [7].

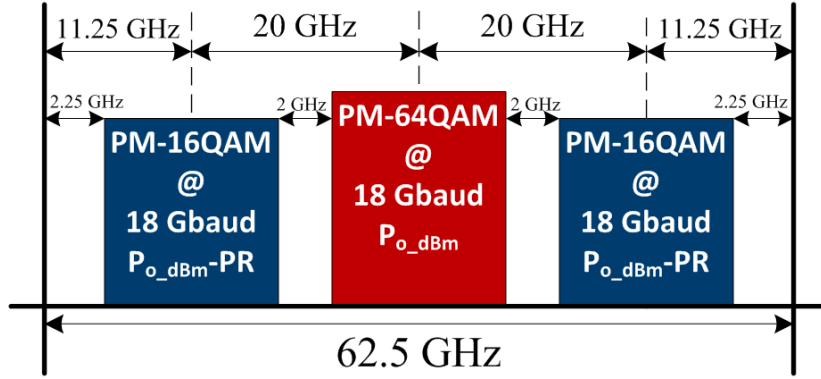


Figure 4.1: Proposed frequency-hybrid superchannel composed of a central PM-64QAM carrier and two edge PM-16QAM carriers, each carrier operating at 18 GBaud.

In alternative to the proposed frequency-hybrid superchannel, a superchannel composed of PM-32QAM carriers could have also been considered. However, since Gray coding can not be applied on non-square cross QAM constellation, the BER can not be further improved. Moreover, a more complex transmitter structure would be required to implement a correlated I-Q modulation [8]. When compared to PM-32QAM carrier superchannel, the proposed hybrid solution is more resilient to ROADMs-based WSS filtering, due to the use of PM-16QAM carriers at the edges of the superchannel (which can operate at a lower power and also presents higher filtering tolerance than PM-32QAM carriers) [9, 10], whilst avoiding the use of non-square QAM carriers.

In hybrid modulation systems, the optimum PR between formats depends on the transmitter operation strategy. In [11], four transmitter operation strategies for time-hybrid modulation formats were proposed and the respective theoretical optimum PR were derived for additive white Gaussian noise (AWGN) channels. However, the nonlinear effects generated during signal propagation may substantially change the optimum PR regimes derived for AWGN channels. To address this issue, the use of advanced nonlinear modeling techniques [6, 12–16] is required, such as the recently proposed EGN model [6]. The EGN model accounts for the impact of different modulation formats assigned to each superchannel carrier on the generated nonlinear interference (NLI). In this work, the proposed superchannel is initially analyzed from the theoretical point of view using the

EGN model and later validated by experimental and simulation (split-step based) results. In addition, since in hybrid modulation transmission systems the different formats may have quite different performances, three distinct FEC coding schemes are considered in the evaluation of the superchannel performance after linear and nonlinear compensation.

4.2 Nonlinear Interference

Optical fibers are known to be a nonlinear propagation channel, where the capacity of the optical transmission channel has a nonlinear dependency with the transmitted power. For low optical powers, the channel capacity is proportional to the signal-to-noise ratio (SNR), but when the optical power increases beyond a certain value, Kerr nonlinear effects arise and the channel capacity is reduced due to nonlinear interferences (NLIs) [17, 18]. Therefore, in long-haul optical transmission systems, where the optical losses are compensated by lumped amplification, the channel capacity is mainly limited by the amplified spontaneous emission (ASE) noise accumulation due to erbium-doped fiber amplifiers (EDFAs), for low optical power, and by the NLI, for high optical power.

The modeling of ASE noise effects in the optical systems is well known within the scientific community. However, the modeling of nonlinearities is still an active research topic. In the last few years, several models that address the impact of nonlinear propagation effects in uncompensated transmission channels have been proposed, and validated by simulation and experimental results [6, 12–16].

Along this chapter, we focus on the modeling of the impact of nonlinear propagation effects in optical coherent transmission systems, aiming to evaluate the performance of the proposed 400G frequency-hybrid triple-carrier superchannel solution. We will start with a brief introduction to the well known Gaussian noise (GN) model and its recently-proposed enhancement, known as enhanced Gaussian noise (EGN) model. Later, we analytically evaluate the impact of the NLI on the proposed transmission system.

4.2.1 Gaussian noise model

The so-called GN model was initially proposed with the intent of finding an effective and accurate way of predicting impact of nonlinear propagation effects in uncompensated coherent transmission systems, and consequently evaluate the performance of such systems. Considering uncompensated optical fiber systems, the proposed GN model emerged based on the assumptions that [14, 16]:

- the transmitted signal statistically behaves as a stationary Gaussian noise. Although this assumption is not true at the transmitter output, the I-Q signal components tend to get dispersed as it propagates through an uncompensated and dispersive optical fiber, assuming a Gaussian-like distribution;
- the NLI disturbance manifests as additive GN. Therefore, it can be seen as a perturbative approach where nonlinear distortions are considered as additive noise with zero-mean Gaussian distribution, statistically independent from ASE noise.

The statistical distribution of a PM-QPSK signal was analyzed by simulations in [19] and by experiments in [20], where the above assumptions were found to be true, in both linear and nonlinear propagation regimes. It was also shown that even in the absence of ASE noise and after DSP, the statistical Gaussian distribution of the signal components remain.

Assuming that the optical link is composed of identical spans (homogeneous link), and that the losses of each span are totally compensated by optical amplification (transparent link), GN model reference formula is given by [16]

$$G_{NLI}(f) = \frac{16}{27} \gamma^2 L_{eff}^2 \int_{-\infty}^{\infty} \int_{-\infty}^{\infty} G_{WDM}(f_1, f_2, f) \varrho(f_1, f_2, f) \chi(f_1, f_2, f) df_2 df_1. \quad (4.1)$$

Equation (4.1) represents the power spectral density (PSD) of the NLI noise at the end of the optical link for a frequency f , $G_{NLI}(f)$, corresponding to the integrated result of all the non-degenerated FWM products occurring among any three spectral components of the transmitted signal, located at f_1 , f_2 and $f_3 = (f_1 + f_2 - f)$. The integrand factor

$$G_{WDM}(f_1, f_2, f) = G_{WDM}(f_1) G_{WDM}(f_2) G_{WDM}(f_3), \quad (4.2)$$

represents the power spectral density that each of the three pumps carries. It is related to the FWM process as it is a product of three signal frequency components that act as 'pumps' for the FWM process itself. The integrand factor $\varrho(f_1, f_2, f)$ accounts for the non-degenerate FWM efficiency of the beating of three 'pump' frequencies. Assuming EDFA amplification, like in our setup, the following closed-form is obtained

$$\varrho(f_1, f_2, f) = \left| \frac{1 - \exp^{-2\alpha L_{span}} \exp^{j4\pi^2 \beta_2 L_{span} (f_1 - f)(f_2 - f)}}{2\alpha - j4\pi^2 \beta_2 (f_1 - f)(f_2 - f)} \right|^2 L_{eff}^{-2}, \quad (4.3)$$

where α is the fiber loss coefficient [km^{-1}], L_{span} is the fiber span length [km], β_2 is the group velocity dispersion coefficient [$\text{ps}^2 \text{km}^{-1}$] and L_{eff} is the span effective length, which is defined as

$$L_{eff} = \frac{1 - \exp^{-2\alpha L_{span}}}{2\alpha}. \quad (4.4)$$

Finally, the factor $\chi(f_1, f_2, f)$ is accounting for the NLI accumulation along the channel and is defined as

$$\chi(f_1, f_2, f) = \frac{\sin^2(2N_{spans} \pi^2 (f_1 - f)(f_2 - f) \beta_2 L_{span})}{\sin^2(2\pi^2 (f_1 - f)(f_2 - f) \beta_2 L_{span})}, \quad (4.5)$$

where N_{spans} is the total number of spans in a link. Note that, in practice, the integration range of equation (4.1) is limited by the optical bandwidth of the transmitted WDM signal spectrum.

4.2.2 Enhanced Gaussian noise model

The EGN model was derived from the GN model by removing the assumption that the signal launched into the optical channel behaves statistically as Gaussian noise. Therefore, for the EGN model the NLI PSD, $G_{NLI}^{EGN}(f)$, can be obtained as follow

$$G_{NLI}^{EGN}(f) = G_{NLI}^{GN}(f) + G_{NLI}^{corr}(f), \quad (4.6)$$

where $G_{NLI}^{GN}(f)$ is the NLI PSD derived in equation (4.1), and $G_{NLI}^{corr}(f)$ is the correction term that has to be considered in order to account for the signal non-Gaussianity effect. Since the focus of this work is not on the modeling of fiber nonlinear propagation, we will not elaborate on this correction term. A detailed explanation of this term used to rectify the errors caused by the GN model can be found in [6].

The EGN model also takes into account the impact of different modulation formats on the generated NLI [6]. This is a feature of interest, since in this work the proposed superchannel is composed of different modulation formats.

It must be noticed that the EGN model addresses several types of NLIs, thereby it can also be defined as

$$G_{NLI}^{EGN}(f) = G_{SCI}^{EGN}(f) + G_{XCI}^{EGN}(f) + G_{MCI}^{EGN}(f), \quad (4.7)$$

with $G_{SCI}^{EGN}(f)$, $G_{XCI}^{EGN}(f)$ and $G_{MCI}^{EGN}(f)$ accounting for the PSDs of the self-channel interference (SCI), cross-channel interference (XCI) and multi-channel interference (MCI) at the receiver [16].

4.2.3 System performance estimation

Despite there is no closed-form expression for the optical channel capacity, it can be accurately modeled using an AWGN channel model, where the channel capacity is giving by the following equation

$$C = 2BW \log_2(1 + SNR), \quad (4.8)$$

where the factor 2 accounts for the fact that information is carried in the two polarizations of the fiber, BW is the optical signal bandwidth and SNR is the signal-to-noise ratio of the channel.

In the case of a linear AWGN channel, with additive Gaussian noise and neglecting PDLs, the SNR is defined as

$$SNR = \frac{P_{tx}}{P_{ASE}}, \quad (4.9)$$

where P_{tx} is the average signal power per channel and $P_{ASE} = G_{ASE}BW_N$ is the ASE noise power measured in a given optical noise bandwidth, BW_N .

$$G_{ASE} = [N_{spans}(G - 1)Fhf_0] \quad (4.10)$$

is the dual-polarization ASE noise PSD, with G the EDFA gain, F the noise figure of the EDFA, h the Planck's constant and f_0 the central frequency of the optical channel.

Since nonlinear channels are also impacted by nonlinearities that can be modeled as additive Gaussian noise, the SNR in an optical communication system should be re-defined, in order to account for both ASE and NLI noise power contributions, as follows

$$SNR_{NL} = \frac{P_{tx}}{P_{ASE} + P_{NLI}}. \quad (4.11)$$

The P_{NLI} is the NLI noise power falling over the center channel of the WDM comb and is defined as

$$P_{NLI} = \int_{-R_s/2}^{R_s/2} G_{NLI}(f) df. \quad (4.12)$$

The $G_{NLI}(f)$ is calculated using one of the previously presented nonlinear propagation models. This formulation is valid when using a matched filter at the receiver and a signal with an approximately rectangular pulse spectrum (small roll-off factor).

Besides ASE and NLI noises, other impairments due to transmitter and receiver implementation penalties can also be present, namely linear interchannel crosstalk noise and intersymbol interference. In order to account for this extra B2B noise power, P_{B2B} , the overall modified SNR becomes

$$SNR_{total} = \frac{P_{tx}}{P_{ASE} + P_{NLI} + P_{B2B}}. \quad (4.13)$$

We must point out that this penalty might vary for different modulation formats.

From the computed SNR we can derive the system BER, which is dependent on the modulation format, symbol rate (R_s), and chosen value for BW_N . The general BER formula for M-QAM constellations is given by

$$BER_{M-QAM} = \frac{2}{\log_2 M} \left(1 - \frac{1}{\sqrt{M}} \right) \text{erfc} \left(\sqrt{\frac{3}{2(M-1)}} SNR \right), \quad (4.14)$$

where $\text{erfc}(\cdot)$ gives the complementary error function.

Note that, along this chapter, the BER associated to each modulation format composing the superchannel is determined using equation (4.14), while the overall superchannel performance is dependent on the FEC strategy being considered. Additional details regarding the considered FEC modes are provided in section 4.5.

4.3 400G Frequency-Hybrid Transmission System

In this section, we describe the experimental setup and the set of DSP algorithms used in the experimental validation of the proposed 400G frequency-hybrid superchannel. This work was carried out in collaboration with Politecnico di Torino and Istituto Superiore Mario Boella, Torino, Italy, from where all the experimental data presented here was obtained.

4.3.1 Experimental setup

The scheme of the experimental setup used for the transmission of a WDM channel composed of nine 400G frequency-hybrid superchannels is depicted in Figure 4.2. At the transmitter side, the central superchannel carriers (superchannel under test) are generated by 3 external cavity laser (ECL) (<100 kHz linewidth), while the remaining 24 carriers are generated by distributed feedback (DFB) lasers. The central PM-64QAM optical carrier is modulated using a DP-IQM, driven by a DAC operating at 64 GSa/s and with an electrical bandwidth of 8 GHz. A second DAC is then used to create two independent 16QAM signals, which are then PM by means of a polarization multiplexer emulator, yielding the two edge PM-16QAM carriers. The modulation signals are obtained from uncorrelated $2^{15}-1$ pseudo random bit sequences (PRBSs), digitally shaped by a raised-cosine filter with a roll-off factor of 0.05 and pre-emphasized to compensate for the bandwidth limitations of the transmitter components. After coupling the optical carriers, the PR between superchannel carriers is adjusted by a programmable optical filter placed at the optical coupler output, before the EDFA. The PR between carriers is adjusted identically for all the 9 WDM superchannels.

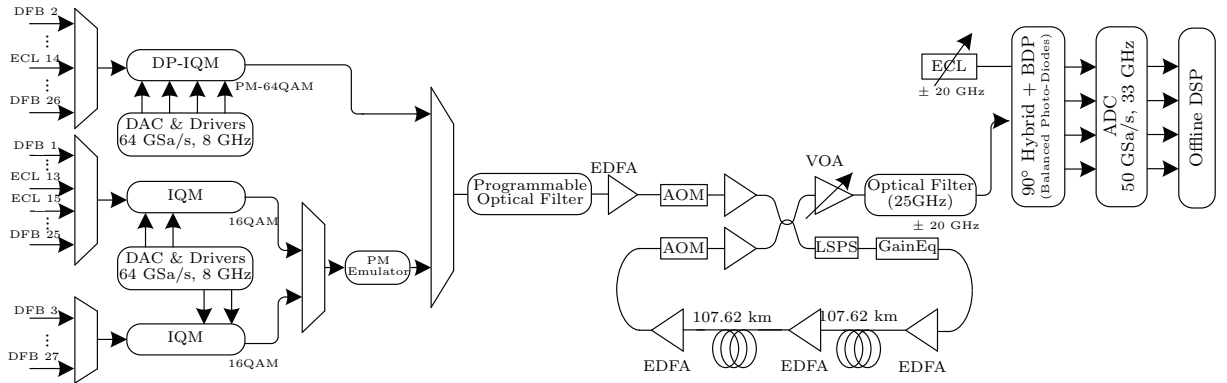


Figure 4.2: Experimental setup of an WDM transmission system composed by 9 of the proposed 400G frequency-hybrid superchannels.

The generated 9 WDM 400G superchannels are then launched into the optical recirculating loop, controlled by two acousto-optic modulators (AOM) and composed of 2×107.62 km spans of PSCF, where each span consists of 54.44 km of PSCF150 followed by 53.18 km of PSCF110. It was considered that the fiber has an attenuation (α) of 0.16 dB/km, a dispersion slope (D) of 20.6 ps/nm/km, a nonlinearity coefficient (γ) of $0.7 \text{ W}^{-1}\text{km}^{-1}$ and 1.5 dB of extra losses per span that are attributed to the splices between PSCF transition patch-cords and the fiber spools [21]. A loop synchronous polarization scrambler (LSPS) is inserted to average out polarization dependent effects in the loop. After each fiber span, an EDFA, with a noise figure of 5.5 dB, compensates for the total span loss of 18.75 dB. The loop also includes a gain-equalizer unit, represented in the figure by the block *Gain Eq*, which is required to correct for residual gain errors and to preserve the applied PR between carriers.

After the recirculating loop, a standard coherent receiver detects each carrier of the central superchannel, tuning the LO laser (ECL) and the optical filter to the desired

carrier. A 25 GHz bandwidth tunable optical filter is inserted at the receiver input, aiming to prevent excessive optical power from reaching the photo-detectors. Finally, the signal is sampled by a 50 GSa/s real-time oscilloscope, with an analog bandwidth of 33 GHz, so that offline DSP can be independently applied to each superchannel carrier.

4.3.2 Digital signal processing

The DSP is firstly applied in the compensation of the optical frontend impairments, namely deskew and orthonormalization functions. Before the downconversion of the superchannel carriers to baseband, the signal passes through a band-pass filter in order to obtain the carrier of interest. Afterwards, the remaining DSP algorithms are independently applied to each carrier of the superchannel. A digital resampling stage is then applied to downsample the signal to 2 samples-per-symbol and a static equalization algorithm is applied to perform CDE based on a frequency-domain implementation, or alternatively, intra-carrier nonlinear compensation based on a split-step Fourier DBP technique.

To compensate for the polarization-dependent effects and residual CD, a 2×2 MIMO radially-directed equalizer (RDE) [22, 23] is independently applied to each superchannel carrier. For the PM-16QAM carriers, the RDE is initialized in a data-aided (DA) mode, with the correct radii of the 16QAM constellation being known *a priori* from a training sequence. After the tap convergence is reached, the RDE equalizer is switched to a decision-directed (DD) mode [22, 23]. In turn, for the PM-64QAM carrier, the RDE equalizer is kept in DA mode at all times, to avoid possible tap divergence issues. Note that, when using SD-FEC, the PM-64QAM carrier can be operating in a high BER regime, which may be more challenging for the equalizer convergence and stability. Therefore, the use of fully-DA equalization for the PM-64QAM carrier is a design choice thus ensuring a more robust equalization, and thus avoiding any interference of possible DSP implementation issues on the performance analysis of the frequency-hybrid 400G superchannel. Nevertheless, we do not expect this simplified DSP assumption to create significant performance changes, since it has been already shown in other works that blind DSP can be adequately designed for PM-64QAM with very small implementation penalty [23].

After channel impairments equalization, the frequency estimation is performed by a 4th-power spectral method, while an initial coarse phase estimation based on the 4th-power Viterbi-Viterbi algorithm is applied to the QPSK-like symbols in the PM-16QAM and PM-64QAM carriers. Although this Viterbi-Viterbi carrier phase estimation (CPE) stage is applied on the $2 \times$ oversampled signal, phase estimation is actually performed on a downsampled version of the signal (1 sample-per-symbol). The extracted phase noise trace is then upsampled to 2 samples-per-symbol and removed from the signal, allowing for a subsequent fractionally-spaced FIR-based adaptive equalization stage. An additional ISI 4×4 adaptive equalizer is required after CPE for fine tuning of the linear adaptive equalization, and to compensate for the residual I-Q transmitter skew. This equalizer is based on a LMS algorithm, with a DA convergence stage followed by DD operation in steady-state for the PM-16QAM carriers and fully-DA operation for the

PM-64QAM carrier, with the real and imaginary parts of each signal polarization being independently treated. At the end, the signal is downsampled to 1 sample-per-symbol and a second fine-tuned CPE stage based on a maximum likelihood decision-directed (ML-DD) algorithm, using 31 taps, is applied [24]. Note that, the number of taps used in each algorithm is separately optimized for each of the two modulation formats. Finally, after signal demapping, the BER associated to each superchannel carrier is estimated.

4.4 Individual Superchannel Carriers Performance

Optical transmission systems based on hybrid modulation formats may present different performances for the distinguish modulation formats composing the channel. Therefore, for a given modulation format, we must optimize the transmission parameters to achieve a near optimal performance of our optical transmission system. In this section, we aim to individually evaluate the performance of each superchannel carrier by varying the applied PR between formats, since this parameter plays an important role in hybrid modulation formats transmission systems. The experimental results are obtained using the setup presented in the previous section, while split-step-based simulations were carried out using the commercial optical system simulator OptSimTM. The experimental and simulation results are also validated by the EGN model. The analysis being conducted here aims to determine the superchannel maximum reach for a BER threshold of 2.4×10^{-2} (assumption of a 20% SD-FEC). The system performance is analyzed when applying regular CDE (EGN_{CDE}, SIM_{CDE}, LAB_{CDE}), and also when applying DBP-based nonlinear equalization (EGN_{DBP}, SIM_{DBP}, LAB_{DBP}). The latter is applied to assess the improvement in terms of maximum reach and evaluate its impact on the optimum PR and optimum launch power. Since DBP is independently applied on each superchannel carrier, we are compensating only for the nonlinear effects caused by the carrier on itself.

Initially, we evaluate the experimental setup in a B2B configuration, aiming to determine the transmitter and receiver implementation penalties associated to each superchannel carrier, which will affect the theoretical performance predictions of our transmission system. Considering the defined BER threshold of 2.4×10^{-2} , the experimental B2B penalties associated with the PM-16QAM and PM-64QAM carriers were determined to be 0.8 dB and 2.3 dB, respectively. For uniformity with the experimental scenario, B2B penalties were taken into account by noise loading to the received signal in the simulation, and by adjusting the target SNR in the EGN model. Afterwards, the experimental setup was analyzed for different values of PR. For each PR, we varied the input mean power per superchannel between -8 dBm and 2 dBm, and the number of loop recirculations, ranging from 1 to a maximum of 20 recirculations (about 4300 km).

Along this section, the plotted curves (dashed, dotted lines) refer to the EGN model predictions, the open markers (Δ , ∇ , \circ , \square) refer to the simulation results and the filled markers (\blacktriangle , \blacktriangledown , \bullet , \blacksquare) refer to the experimental results. Note that, the PM-16QAM experimental and simulation results presented in the figures were obtained from the BER mean of the two PM-16QAM edge carriers. Figure 4.3 presents the estimated maximum

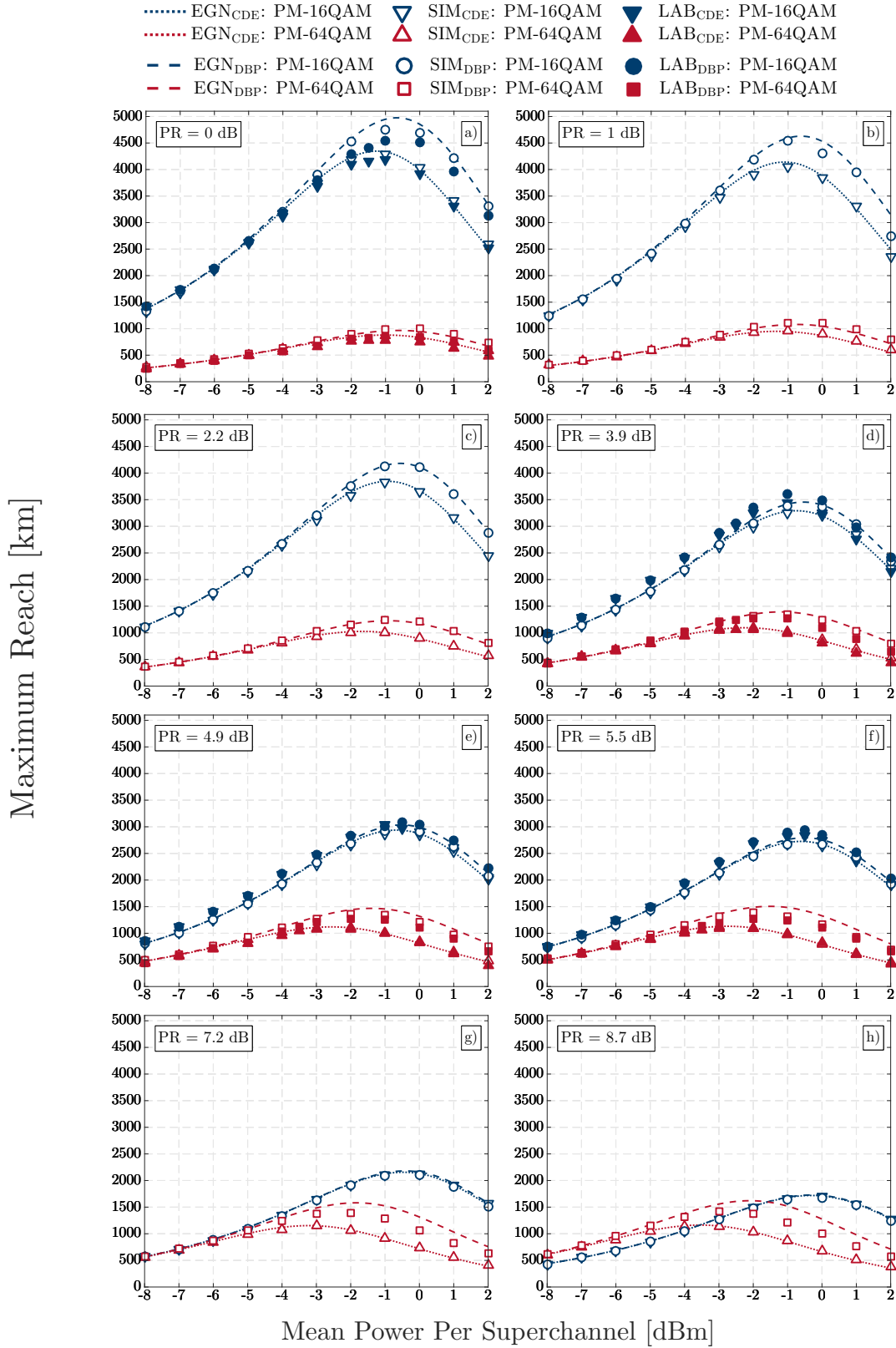


Figure 4.3: Maximum reach as a function of the mean power per superchannel, for different values of PR between carriers, when considering CDE or alternatively DBP of each superchannel carrier (for the superchannel under test).

4.4. Individual Superchannel Carriers Performance

reach (MR) of each superchannel carrier as a function of the mean power per superchannel and PR, for CDE (dotted-curves and Δ , \blacktriangle , ∇ , \blacktriangledown markers) and DBP (dashed-curves and \square , \blacksquare , \circ , \bullet markers) cases. To evaluate the effect of single-carrier NLE, SSFM-based DBP with 2 steps per span was applied to both experimental and simulation results, aiming to guarantee a near optimal DBP performance. For the analytical EGN model, we firstly run the EGN model for a single-carrier system under analysis, thus calculating the amount of NLI generated by the single-carrier alone ($P_{NLI,1ch}$). Afterwards, in the post-processing, the obtained $P_{NLI,1ch}$ is removed from the total NLI affecting each superchannel carrier (when considering the WDM transmission of the 9 superchannels), as follows

$$P_{NLI,res} = P_{NLI} - P_{NLI,1ch}. \quad (4.15)$$

In the above equation, $P_{NLI,res}$ is the residual value of NLI impacting the superchannel carrier after NLE. This corresponds to the ideal case where we completely remove the single-carrier nonlinear effects while leaving in all the other nonlinearities (i.e. XCI and MCI).

The experimental and simulative MRs presented as a function of mean power per superchannel were obtained from the interpolation of the BER results obtained after each recirculation, every 2 spans. As expected, the PM-64QAM carrier (red results) shows a shorter MR than PM-16QAM (blue results) for low PRs, this happens mainly because of the higher SNR required by the PM-64QAM to deliver the target BER, but also, because it has an higher sensitivity to nonlinear propagation effects. For high PRs, the carriers performances are leveled out. It can be observed that the increase of PR involves a compromise between the MRs achieved by the PM-16QAM and PM-64QAM carriers, caused by the inter-carrier NLI. Increasing the PR causes a reduction of the MR achieved by the PM-16QAM carrier, since the PM-16QAM power is reduced relatively to the PM-64QAM power, thereby suffering from higher inter-carrier NLI produced by the adjacent PM-64QAM carriers. On the other hand, the MR achieved by the PM-64QAM increases due to the lower NLI generated by the adjacent reduced power PM-16QAM carriers.

We can also observe that, when DBP is applied, there is a clear improvement of the superchannel carriers MR. However, as PR increases, the nonlinear compensation benefit on the PM-16QAM carriers tends to become less pronounced, due to the fact that we are decreasing its power and consequently the nonlinearities caused by the carrier over itself. On the other hand, the PM-64QAM carrier performance significantly improves not only due to the compensation of SCI, but also due to the lower nonlinear effects caused by the adjacent carriers. Indeed, for PR=2.2 dB, a MR increase of $\sim 20\%$ and $\sim 9\%$ is obtained for the PM-64QAM (~ 1200 km against ~ 1000 km) and PM-16QAM carriers (~ 4150 km against ~ 3800 km), respectively. In turn, for higher PRs, such as 8.7 dB, a MR gain of $\sim 40\%$ is obtained for the PM-64QAM carrier (~ 1650 km against ~ 1150 km), while it becomes negligible for the PM-16QAM carriers, due to its low power, i.e. linear regime of operation.

In general, there is a good agreement between the experimental results with the EGN model and simulation analysis, Figure 4.3. Only for few cases based on DBP there is a small misalignment between results, which may be due to the presence of stronger

nonlinear signal-to-noise interactions in the optical link and also due to the possible correlations between the various carriers in the laboratorial experiment (resulting from the even-odd modulation) [25, 26]. Note although, that these differences are always less than 15%. This comprehensive study on the individual performance of superchannel carriers allowed us to confirm that both EGN model and simulation analysis are fully aligned with the experimental results, proving that an accurate parameter identification has been successfully conducted. Under these conditions, in the next sections we assess different FEC techniques and compensation strategies applied to our transmission system. Later, in section 4.6 we take advantage of the EGN model to extend our analysis beyond the experimental data and demonstrate some advanced DBP approaches that can be applied over superchannel-based transmission systems.

4.5 Joint Power-Ratio and FEC Optimization

In the previous section, we focus on the individual performance analysis of each superchannel carrier for different PRs between modulation formats. In this section, we extend our previous analysis for taking into account the overall superchannel performance. To do so, we will determine the optimum PR between superchannel carriers when considering different FEC paradigms.

In [11] four transmitter operation strategies for time-hybrid modulation formats were proposed and the respective theoretical optimum PR was derived when considering AWGN channels. However, it has been shown that the nonlinear effects arising during signal propagation in fiber may substantially change the optimum PR regimes derived for AWGN channels. Moreover, given the different performances associated to each modulations format, different FEC techniques have been proposed for the hybrid scenarios, aiming to determine the approach that provides the best overall system performance. In [27] a flexible FEC approach was applied to a TDHMF system based on hybrid PM-QPSK and PM-16QAM formats, where each format operates with its own FEC code, which showed an improvement of the system sensitivity compared to a single FEC approach. This technique was also applied to a superchannel system [28] and to a full WDM C+L-band transmission system [29, 30] aiming to counteract the performance variations between different carriers and/or channels.

4.5.1 FEC paradigms

In this section and for the remaining of this chapter, the overall system performance is evaluated considering the following three distinct FEC paradigms:

- **superchannel FEC (SC-FEC)**, consisting of a single FEC code that is applied to the overall 400G data stream carried by the three carriers composing the superchannel. Figure 4.4a depicts the block diagram corresponding to the SC-FEC implementation. A single FEC encoder is applied to the entire data stream of a superchannel, which is then sent to an interleaver block that decorrelates the

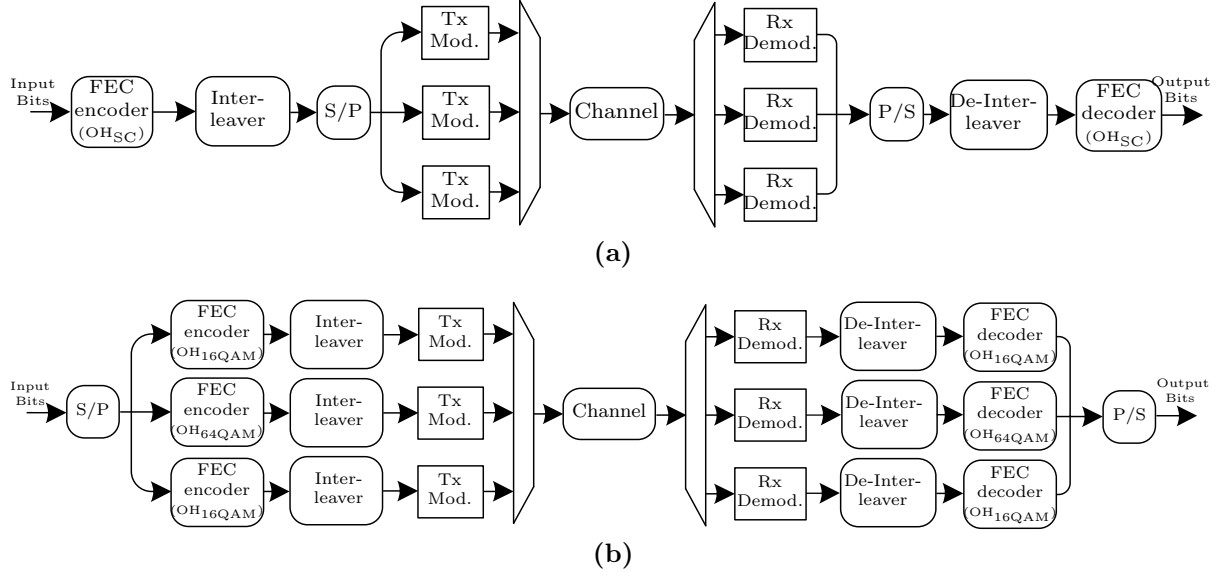


Figure 4.4: Block diagram for the implementation of the considered FEC paradigms: a) SC-FEC (OH_{SC} = 20%) and b) IC-FEC (OH_{16QAM} = OH_{64QAM} = OH_{SC} = 20%) or Flex-FEC (OH_{16QAM} ≠ OH_{64QAM} but OH_{SC} = 20%).

data stream over time and across the superchannel carriers. After that, a serial-to-parallel (S/P) conversion block is applied to divide the data streams into the carriers data streams. Each carrier is then independently modulated and combined in a superchannel for optical transmission. At the receiver, after independent demodulation of the each superchannel carrier, the data streams are combined again by a parallel-to-serial (P/S) conversion block and send to the de-interleaver block. A single FEC decoder block is then applied to the entire superchannel data stream, aiming to retrieve the transmitted bits.

In this work, the superchannel FEC overhead (OH) is defined to be 20%. Since FEC coding/decoding is interleaved among all superchannel carriers, the system performance can be assessed through the following equation

$$\text{BER}_{\text{SC}} = \frac{\sum_n \log_2(M_n) \text{BER}_n}{\sum_n \log_2(M_n)}, \quad (4.16)$$

where BER_{SC} is the pre-FEC weighted average BER of the entire superchannel, BER_n is the BER measured on the n -th superchannel carrier and M_n is the constellation cardinality of the n -th superchannel carrier and $\log_2(M_n)$ is the number of bits-per-symbol of the n -th superchannel carrier. The SC-FEC paradigm can be seen as an equivalent of the minimum BER strategy proposed in [11].

- **independent carrier FEC (IC-FEC)**, consisting of N independent FEC codes, one for each superchannel carrier, with a fixed and common OH. In this case, independent FEC encoder and decoder blocks are applied to each carrier of the superchannel, as can be seen in Figure 4.4b.

In this work, all superchannel carriers operate with the same FEC OH of 20%. Since all superchannel carriers are coded and decoded independently, the overall superchannel performance is set by the worst performing carrier and thus it can be assessed by the highest individual pre-FEC BER, as follow

$$\text{BER}_{\text{SC}} = \max(\text{BER}_n). \quad (4.17)$$

Therefore only the worst performing carrier is operating at the FEC threshold, while the remaining carriers are practically working error free, thus presenting some margin to the defined FEC threshold. The IC-FEC paradigm can be seen as an equivalent of the same BER strategy proposed in [11].

- **independent carrier flexible FEC (Flex-FEC)**, similarly to the IC-FEC case, an independent FEC code is assigned to each superchannel carrier, but, in this case, the allocated OHs are optimized on a per-carrier basis.

In order to maintain a net bit-rate of 400 Gbit/s and get a fair comparison with the SC-FEC and IC-FEC approaches, in this work we constrain the total superchannel Flex-FEC overhead OH_{SC} (weighted average of all FEC OHs per carrier) to 20%. Considering that the two PM-16QAM edge carriers should exhibit a similar performance, we constrain them to have the same OH. For a given OH in the PM-64QAM carrier, $\text{OH}_{64\text{QAM}}$, the correspondent OH in the PM-16QAM carriers, $\text{OH}_{16\text{QAM}}$, is given by

$$\text{OH}_{16\text{QAM}} = \frac{(\sum_n \log_2(M_n))\text{OH}_{\text{SC}} - \log_2(M_{64\text{QAM}})\text{OH}_{64\text{QAM}}}{2\log_2(M_{16\text{QAM}})}. \quad (4.18)$$

where the 2 factor is accounting for the two PM-16QAM edge carriers. Then, similarly to the IC-FEC case, the superchannel performance with Flex-FEC coding can be assessed from the maximum pre-FEC BER among all carriers, equation (4.19). However, in this case, the limit pre-FEC BER must be adjusted according to the OH required by each FEC, details are provided in the next paragraphs.

The application of the Flex-FEC strategy requires the determination of the new BER threshold depending on the set of FEC OHs. Figure 4.5 shows the pre-FEC BER thresholds, for a pos-FEC BER of 10^{-15} , as a function of FEC OHs. We took advantage of the values presented in [7], Table I, to determine the pre-FEC BER associated to each FEC OH. The NCG associated to each FEC OH is determine by linear interpolation of these values. We can then determine the respective pre-FEC BER defined as

$$\text{BER}_{\text{pre-FEC}} = \text{erfc} \left(10^{\frac{20 \log_{10}(\text{erfc}^{-1}(2\text{BER}_{\text{pos-FEC}})) - \text{NCG} + 10 \log_{10} R_c}{20}} \right) / 2, \quad (4.19)$$

where $\text{BER}_{\text{pre-FEC}}$ is the pre-FEC BER, $\text{BER}_{\text{pos-FEC}}$ is the reference pos-FEC BER and R_c is the code rate, defined as the ratio of bit rate without and with FEC. Considering the constraint of an overall $\text{OH}_{\text{SC}} = 20\%$, in Figure 4.5, we present the considered values of PM-64QAM OH ($\text{OH}_{64\text{QAM}}$) and the correspondent PM-16QAM OH ($\text{OH}_{16\text{QAM}}$).

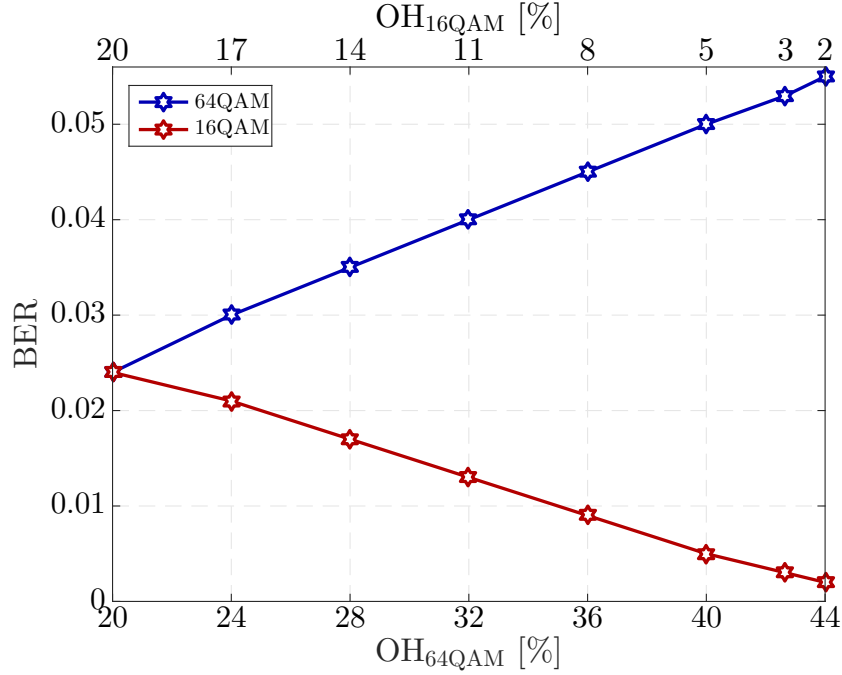


Figure 4.5: Pre-FEC BER as a function of the OH_{64QAM} (bottom X axis) and respective OH_{16QAM} (top X axis), for a pos-FEC BER of 1×10^{-15} . The markers correspond to the set of OHs (OH_{64QAM}, OH_{16QAM}) considered in this work. Note that, the OH_{64QAM}=20% (OH_{16QAM}=20%) point is equivalent to the IC-FEC strategy.

4.5.2 Power ratio optimization

In this section, the PR between the two modulation formats is varied between 0 and 10 dB aiming to determine the optimum system performance for SC-FEC, IC-FEC and Flex-FEC paradigms. The PR is given by

$$PR_{dB} = 10 \log_{10} \left(\frac{SNR_{64QAM}}{SNR_{16QAM}} \right), \quad (4.20)$$

where SNR_{16QAM}/SNR_{64QAM} corresponds to the SNRs required by the 16QAM/64QAM format, which depends on the adopted transmitter operation strategy.

Considering the AWGN channels theory devised in [11], we can theoretically determine the optimum PR values for both IC-FEC and SC-FEC strategies. For the IC-FEC strategy, the optimum performance is obtained when $BER_{16QAM} = BER_{64QAM} = BER_{threshold}$, therefore the required SNR is defined as

$$SNR_{M-QAM}(M) = \frac{2(M-1)}{3} \text{erfc}^{-1} \left(\frac{\sqrt{M} \log_2(M) BER_{threshold}}{2(\sqrt{M}-1)} \right), \quad (4.21)$$

which is then applied in equation (4.20). For the SC-FEC strategy case, we should find the optimum SNR pair, $[SNR_{16QAM}^{opt}, SNR_{64QAM}^{opt}]$, that minimizes the estimated average

BER. For any average SNR, we can derive the optimum $\text{SNR}_{64\text{QAM}}$ from $\text{SNR}_{16\text{QAM}}$, therefore, the following procedure is applied

$$\begin{aligned} \text{SNR}_{16\text{QAM}}^{\text{opt}} &= \left\{ \text{SNR}_1 : \text{BER}_{16\text{QAM}} \left(\text{SNR}_{16\text{QAM}}, \frac{\overline{\text{SNR}} - \kappa_{\text{QAM}} \text{SNR}_{16\text{QAM}}}{1 - \kappa_{\text{QAM}}}, M_{16\text{QAM}} \right) \right. \\ &= \min \left[\text{BER}_{16\text{QAM}} \left(\text{SNR}_{16\text{QAM}}, \frac{\overline{\text{SNR}} - \kappa_{\text{QAM}} \text{SNR}_{16\text{QAM}}}{1 - \kappa_{\text{QAM}}}, M_{16\text{QAM}} \right) \right] \Bigg\}, \end{aligned} \quad (4.22)$$

from which

$$\text{SNR}_{64\text{QAM}}^{\text{opt}} = \frac{\overline{\text{SNR}} - \kappa_{\text{QAM}} \text{SNR}_{16\text{QAM}}^{\text{opt}}}{1 - \kappa_{\text{QAM}}}, \quad (4.23)$$

where κ_{QAM} is the frame ratio between modulation formats defined as $N_{16\text{QAM}}/N$, the $N_{16\text{QAM}}$ represents the number of carriers occupied by the PM-16QAM format and N represents the total number of carriers composing the superchannel.

From equations (4.20), (4.21), (4.22) and (4.23), the optimum performance of the IC-FEC and SC-FEC paradigms are obtained for PRs of 5.7 dB and 3.6 dB, respectively, when considering a target BER of 2.4×10^{-2} . However, these results do not take into account the implementation penalties of any modulation format. Given the different B2B penalties associated with the PM-16QAM (0.8 dB) and PM-64QAM (2.3 dB), in this work the required nominal PRs is increased to 7.2 dB and 4.4 dB for the IC-FEC and SC-FEC strategies, respectively. In fact, Figure 4.3g (PR = 7.2 dB) shows that both modulation formats are performing similarly in the linear propagation regime (the two curves overlap, thereby they are operating at the same BER). However, when the system enters in the nonlinear propagation regime the optimal condition derived in B2B is not valid anymore, due to the generation of different NLIs between optical carriers. This corroborates the previous simulation results presented in [2] for a system with similar hybridization approaches.

After running the EGN model for PRs ranging between 0 and 10 dB, we observed that the MR for the IC-FEC and SC-FEC strategies is in fact achieved for PRs of 8.7 dB and 2.2 dB, respectively, Figure 4.8a. In the IC-FEC strategy, the global MR is set by the worse performing carrier at the optimum superchannel launched power, therefore originating two different regimes of operation:

1. at low PR, where the system MR and the optimum power are set by the worse performing modulation format (in our study case, the PM-64QAM is limiting the MR, since the PM-16QAM always outperforms the PM-64QAM, Figure 4.3);
2. at high PR, where the system MR and the optimum power are set by the crossing point between the MR curves of each modulation format, which are consequently operating at the same BER.

The best system performance is achieved on the transition between these two regimes of operation, occurring in the considered scenario for a PR of 8.7 dB (as can be confirmed from Figure 4.8a). After this point, the maximum system performance starts to be limited

by the PM-16QAM carrier, operating still in the linear regime, due to its very low power, while the PM-64QAM is already operating in the nonlinear regime. In turn, for the SC-FEC strategy, the system MR and optimum power require a continuous balanced compromise between the two modulation formats, since these are determined from the weighted average BER of the superchannel. In the considered scenario, since the PM-16QAM carriers simultaneously enable higher reach and also transport more data (2×4 bits per symbol, against 6 bits per symbol of the PM-64QAM carrier), the maximum performance of the system is achieved for a relatively low PR of 2.2 dB, which provides the best compromise between the two modulation formats in terms of average superchannel BER.

Considering now the application of the Flex-FEC strategy and taking into account for the new BER thresholds associated to each modulation format, the B2B penalties were re-calculated from the experimental B2B characterization. The EGN model was also re-evaluated for all the OHs presented in Figure 4.5, aiming to find the set of OHs $[\text{OH}_{64\text{QAM}}, \text{OH}_{16\text{QAM}}]$ providing the best performance for the Flex-FEC strategy. Figure 4.6, presents the MR as a function of the PR between carriers, for the set of FEC OHs considered in Figure 4.5, when a) CDE and b) DBP techniques are applied. In our hybrid scenario, we achieve the best performance when increasing the $\text{OH}_{64\text{QAM}}$, while reducing the $\text{OH}_{16\text{QAM}}$, in order to maintain a total OH_{SC} of 20%, corresponding to 400 Gbit/s of net bit-rate. Increasing $\text{OH}_{64\text{QAM}}$ allow us to operate at a higher pre-FEC BER, thereby extending the MR of this carrier. The opposite happens for the two PM-16QAM edge carriers. Therefore, the crossing point between the two modulation formats curves will occur for a lower value of PR, which can be confirmed from Figure 4.6. From the same figure we can determine the MR and the correspondent optimum PR for each set of FEC OHs being considered for both equalization approaches. The MR obtained at the optimum PR as a function of the FEC OHs is shown in Figure 4.7, for both CDE and DBP techniques. As expected, the increase of $\text{OH}_{64\text{QAM}}$ enables a gradual increase of MR up to ~ 1940 km and ~ 2300 km (corresponding to an improvement of $\sim 70\%$ and $\sim 50\%$ with respect to the IC-FEC strategy), jointly with a reduction of 6.5 dB and 5 dB in the optimum PR for the CDE and DBP techniques, respectively. The optimum set of FEC OHs for CDE is found for $[\text{OH}_{64\text{QAM}} = 40\%, \text{OH}_{16\text{QAM}} = 5\%]$ and $[\text{OH}_{64\text{QAM}} = 36\%, \text{OH}_{16\text{QAM}} = 8\%]$ for DBP. After these points, the system performance starts deteriorating again, since it becomes limited by the reduced reach of the PM-16QAM carriers, due to their very low $\text{OH}_{16\text{QAM}}$. Results for $[\text{OH}_{64\text{QAM}} = 44\%, \text{OH}_{16\text{QAM}} = 2\%]$ are not shown in Figure 4.6 neither in Figure 4.7, since for this case the optimum performance occurs for a PR less than 0 dB.

All our previous conclusions are summarized in Figure 4.8a, where we show the MR as a function of the PR for all three FEC paradigms. Note that, in the Flex-FEC case, we only present the curve corresponding to the best FEC OH pair, $[\text{OH}_{64\text{QAM}}, \text{OH}_{16\text{QAM}}]$. In the considered scenario, when considering the application of only CDE, the PR optimization allows for a MR extension of $<10\%$, $\sim 30\%$ and $\sim 15\%$ for the SC-FEC, IC-FEC and Flex-FEC strategies, respectively (Figure 4.8a). From the FEC paradigms point of view, the theoretical, simulation and experimental results show that the SC-FEC strategy always outperform IC-FEC strategy in terms of MR. For $\text{PR} = 0$ dB, the

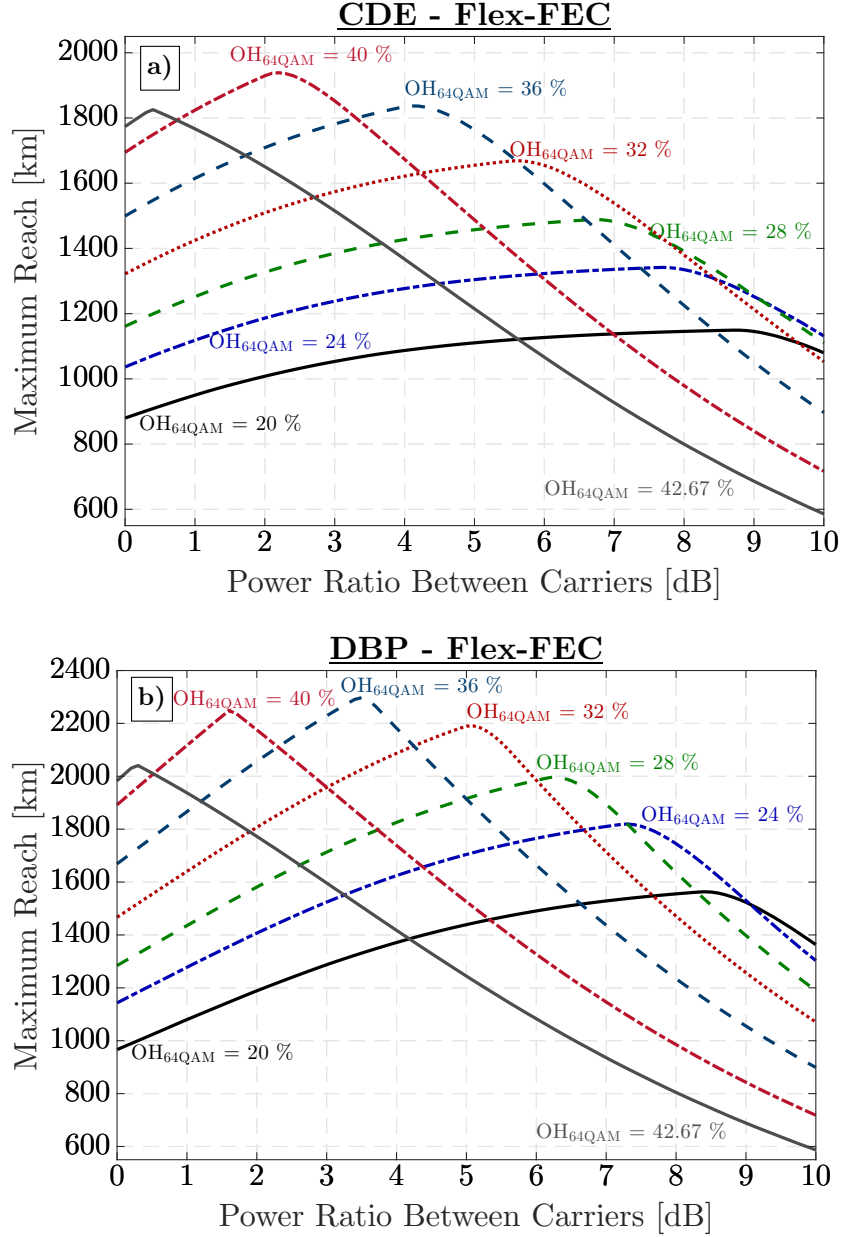


Figure 4.6: Maximum reach as a function of the power-ratio for different sets of FEC OHs, when a) CDE and b) DBP are applied.

SC-FEC strategy doubles the reach provided by IC-FEC. Considering the optimum PR for each FEC strategy (2.2 dB for SC-FEC and 8.7 dB for IC-FEC), the MR gain provided by SC-FEC is $\sim 70\%$. On the other hand, we can note that by adjusting the FEC OHs of each modulation format (Flex-FEC strategy), we can achieve approximately the same MR ($\sim 1\%$ gain using Flex-FEC) of the SC-FEC under the same conditions of operation (PR and optimum launched power). We also demonstrate that when applying DBP the MR achieved with the SC-FEC/Flex-FEC and IC-FEC strategies can be further improved by $\sim 20\%$ and $\sim 35\%$, respectively, see Figure 4.8b. Besides, as consequence of

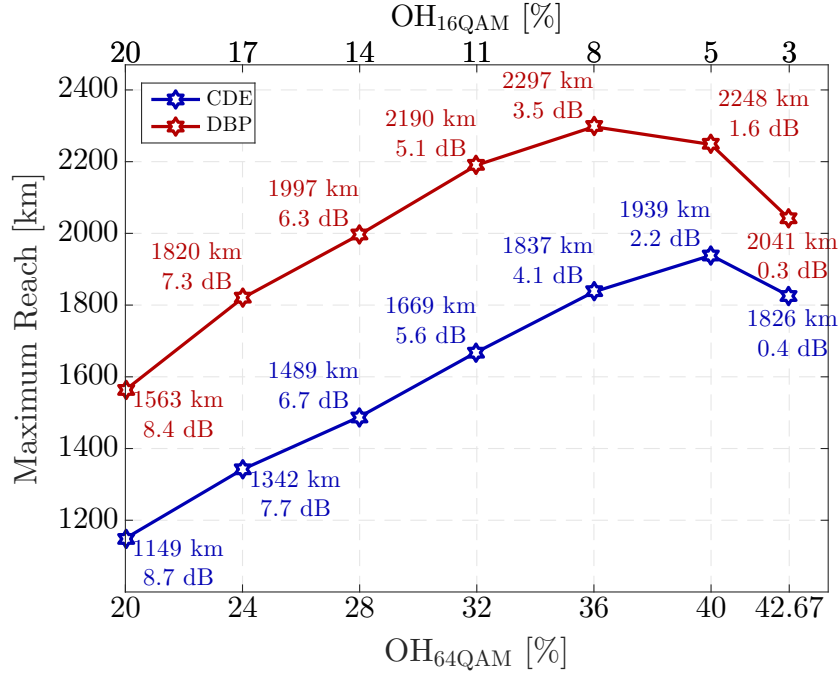


Figure 4.7: Maximum reach as a function of the OH_{64QAM} (bottom X axis) and OH_{16QAM} (top X axis), for both CDE (blue curve) and DBP (red curve) techniques. Note that, for each set of FEC OHs the correspondent maximum reach and optimum power ratio are specified.

DBP, the optimum PR for the SC-FEC and Flex-FEC strategy increases to 3 dB and 3.5 dB (Figure 4.8b), since the MR achieved by the PM-64QAM will be significantly improved when compared with the MR of PM-16QAM. It is also worth to mention that the optimization of PR becomes more important when DBP is applied. In this case, the MR extension provided by optimized PR over PR = 0 dB is of ~15% (from ~2000 km to ~2300 km), ~60% (from ~960 km to ~1560 km) and ~40% (from ~1650 km to ~2300 km) for the SC-FEC, IC-FEC and Flex-FEC strategies, respectively.

Another key system parameter is the optimum launched power per superchannel (P_{opt}), i.e. the mean launched power per superchannel corresponding to the MR. The P_{opt} values as a function of the PR for three FEC paradigms implemented, for both CDE and DBP cases, are shown in Figure 4.9. It can be observed that the lower PR and higher MR achieved by the SC-FEC and Flex-FEC strategies comes at the expense of a 2 dB higher optimum launched power ($P_{\text{opt}} = -1.6$ dBm against $P_{\text{opt}} = -3.6$ dBm for the IC-FEC strategy, in the CDE case). On the other hand, the application of DBP will also impact the optimum launched power, besides its impact on the optimum PR and MR. Indeed, we observe that after DBP, the P_{opt} increases to -0.9 dBm (PR = 3 dB), -1 dBm (PR = 3.5 dB) and -2.2 dBm (PR = 8.4 dB) for the SC-FEC, Flex-FEC and IC-FEC strategies, respectively. This corresponds to a P_{opt} nonlinear tolerance improvement of 0.7 dB, 0.6 dB and 1.4 dB, respectively. The previous 2 dB difference in the optimum powers between SC-FEC/Flex-FEC and IC-FEC operation strategies (see Figure 4.9a) is now reduced to about 1 dB (see Figure 4.9b). The abrupt change of behavior that can be observed for the Flex-FEC P_{opt} curve is due to the transition between different

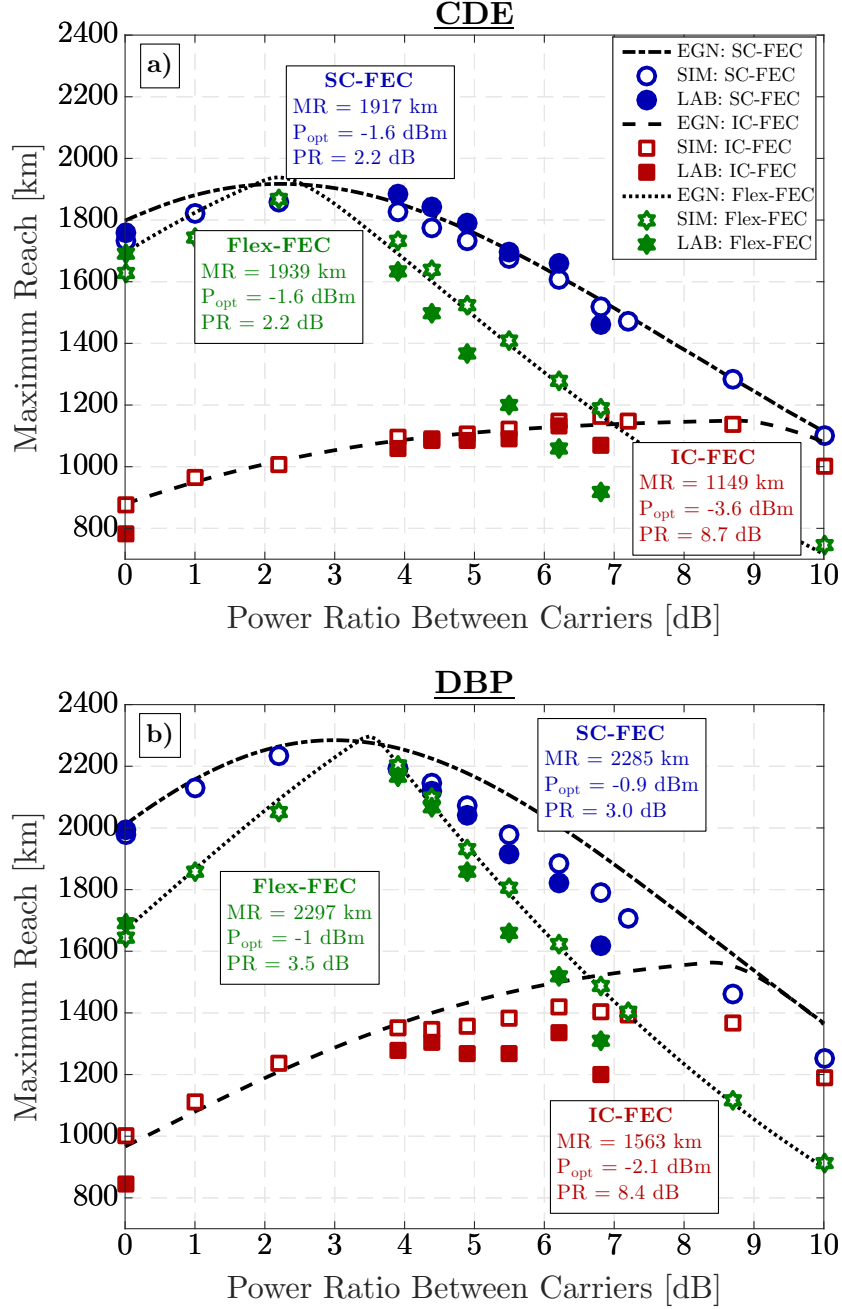


Figure 4.8: System performance in terms of maximum reach as a function of power-ratio for the three FEC strategies, when applying a) CDE and b) DBP individually over each superchannel carrier. Dashed-dotted, dashed and dotted lines correspond to the EGN model predictions for the SC-FEC, IC-FEC and Flex-FEC operation strategies, respectively. Filled and open markers correspond to experimental and simulative results, respectively.

regions of operation: initially P_{opt} is set by the PM-64QAM carrier (in the region where its performance is worse than PM-16QAM), while then, there is a PR for which the two modulation format curves match and P_{opt} is defined by the intersection between the two curves (where one format is operating in the nonlinear regime, while the other is

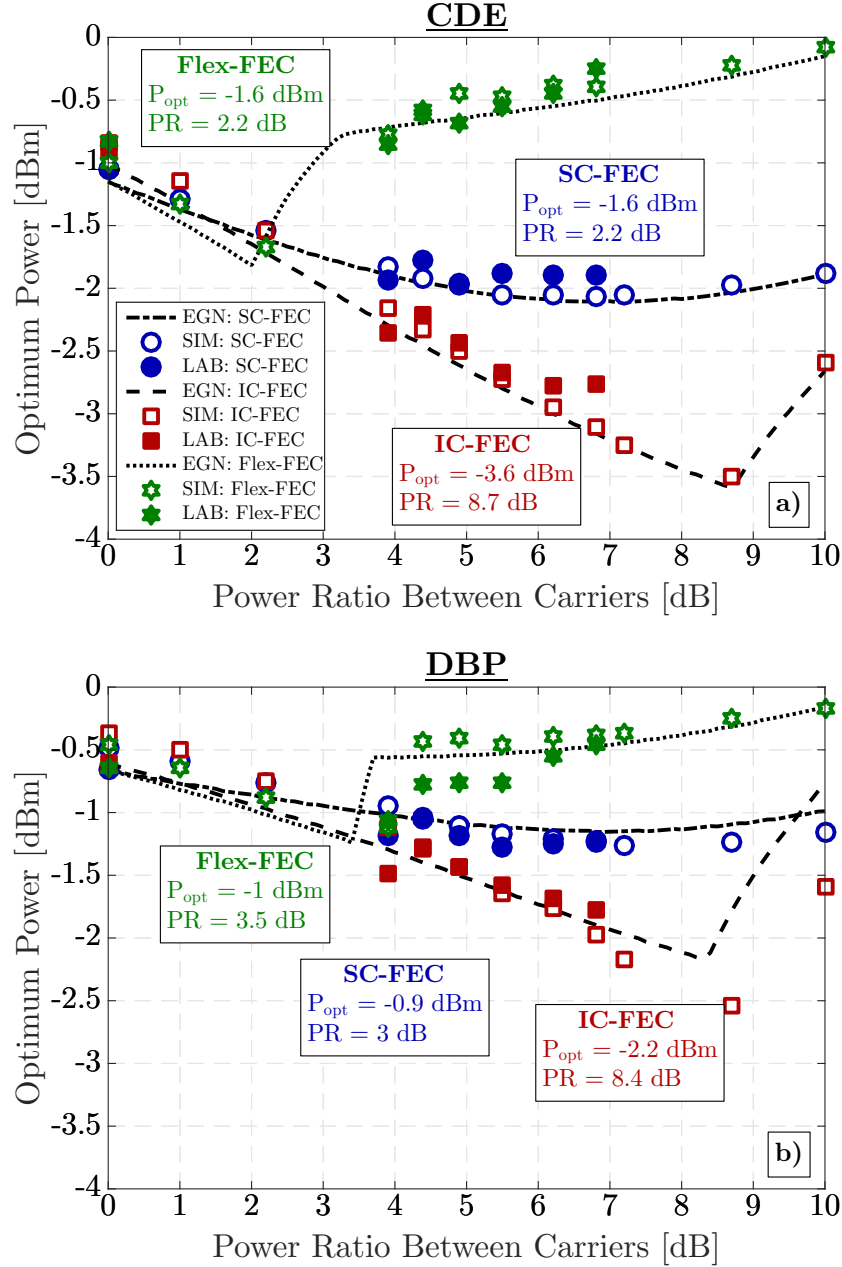


Figure 4.9: Optimum mean power per superchannel as a function of power-ratio for both FEC strategies, when applying a) CDE and b) DBP on each superchannel carrier. Dashed-dotted, dashed and dotted lines correspond to the EGN model predictions for the SC-FEC, IC-FEC and Flex-FEC operation strategies, respectively. Filled and open markers correspond to experimental and simulative results, respectively.

operating in the linear regime). By increasing even more the PR, there will be a point where P_{opt} starts to be given by the PM-16QAM carrier, since its maximum performance becomes worse than PM-64QAM for all mean launched power per superchannel. Note that this transition occurs more steeply in the DBP case.

From the previous analysis, we can conclude that the IC-FEC strategy can be

considered as a lower performance bound, being limited by the highest BER among all superchannel carriers. On the other hand, the SC-FEC strategy tends to present a better performance at the expense of requiring the application of a single FEC to the entire superchannel, for interleaving the bit errors of the worst performing carrier with the bit errors of the remaining carriers. Alternatively, the application of an optimized FEC OH to each modulation format allow us to nearly achieve the same performance of the SC-FEC (under same operation conditions). However, the performance of the Flex-FEC strategy around its optimum PR value was found to vary more abruptly, both in terms of MR (which decreases) and in terms of P_{opt} (which increases).

4.6 Advanced Nonlinear Compensation Strategies

In this section, more advanced nonlinear compensation strategies are applied over the proposed superchannel, aiming to determine the performance improvement that can be obtained when broadening the DBP compensation to account for the entire superchannel nonlinear interferences. We use the EGN model to extend the previous analysis considering different methods for the application of nonlinear equalization to the superchannel under test. Up to this point, we have been considering DBP applied to all the three carriers individually, eliminating only the nonlinear interference from the carrier itself. We now consider three extra nonlinear equalization cases:

1. DBP is applied only to the two PM-16QAM edge carriers individually ($\text{DBP}_{16\text{QAM}}$);
2. DBP is applied only to the center PM-64QAM carrier ($\text{DBP}_{64\text{QAM}}$);
3. DBP is applied jointly to all three carriers forming the superchannel (DBP_{WB} , where WB accounts for the wide-band receiver).

Figure 4.10 shows the EGN model predictions for CDE, DBP (corresponding to the prior DBP results), $\text{DBP}_{16\text{QAM}}$, $\text{DBP}_{64\text{QAM}}$ and DBP_{WB} , for all three FEC strategies: a) SC-FEC (Figure 4.10a), b) IC-FEC (Figure 4.10b) and c) Flex-FEC (Figure 4.10c). From Figure 4.10a it can be seen that there is no significant enhancement of the system MR ($< 5\%$) when DBP is applied individually to all superchannel carriers ($\text{MR}_{\text{DBP}} = 2285$ km) compared to the case where DBP is applied only to PM-64QAM ($\text{MR}_{\text{DBP}_{64\text{QAM}}} = 2242$ km). Thereby, in the case of a single FEC being applied over the hybrid superchannel, the application of DBP only over the PM-64QAM carrier ($\text{DBP}_{64\text{QAM}}$) proves to be a convenient design option for the analyzed scenario, enabling a complexity reduction of approximately $2/3$. Alternatively, if DBP is applied jointly to the whole superchannel (DBP_{WB}) an additional $\sim 10\%$ MR extension is achieved over $\text{DBP}_{64\text{QAM}}$, which in turn corresponds to an improvement of $\sim 30\%$ over CDE. However, this case requires a wide-band (WB) receiver for the joint detection of all three superchannel carriers, such that full-field DBP can be applied. Considering that we employ 62.5 GHz frequency grid, today state-of-the art receivers allow a practical implementation of such approach, but due to limitations in our equipment we could not test it experimentally. Alternatively, we could also detect each carrier independently, through phase and time

4.6. Advanced Nonlinear Compensation Strategies

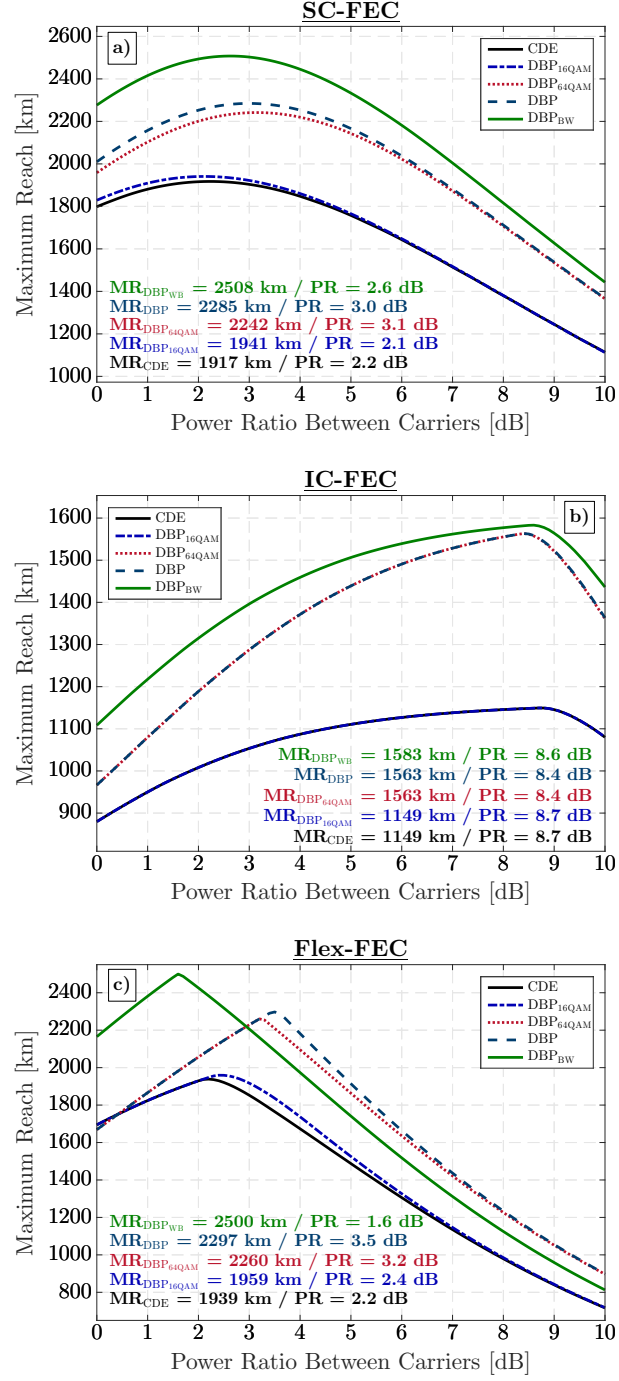


Figure 4.10: Theoretical performance comparison, in terms of maximum reach, for different DBP applications and for all three FEC paradigm: a) SC-FEC; b) IC-FEC and c) Flex-FEC. Black solid lines correspond to the CDE case; Dark blue dashed lines correspond to the individual DBP of all three superchannel carriers (DBP); Blue dashed-dotted lines correspond to the DBP of the edges PM-16QAM carriers (DBP_{16QAM}); Red dotted lines correspond to the DBP of the central PM-64QAM carrier (DBP_{64QAM}); Green solid lines correspond to the jointly DBP on all superchannel carriers.

locked co-operating receivers, and then apply a coupled equations DBP, at the cost of additional implementation complexity [31].

Regarding the IC-FEC strategy, Figure 4.10b shows that the compensation of $\text{DBP}_{16\text{QAM}}$ does not bring any improvement over CDE, neither over $\text{DBP}_{64\text{QAM}}$, since the system performance is limited by the PM-64QAM carrier up to the crossing point between individual carriers MR curves. After the crossing point PRs (> 8 dB) NLI is mainly generated by the PM-64QAM carrier, as proved in the previous sections. In other words, for low values of PR, DBP is not so effective, due to the nonlinear effects of the adjacent channels. On the other hand, increasing the PR between carriers significantly decreases the PM-16QAM power, thereby the nonlinear dominant effects are due to the PM-64QAM carrier of the superchannel, since also the remaining PM-64QAM adjacent carriers are at spaced by 62.5 GHz, not causing significant effect on the system performance. In contrast with the previous case, DBP_{WB} with IC-FEC brings an improvement of only 1% on the achievable system MR (at the optimum PR). Note that the improvement provided by DBP_{WB} is more significant for PR = 0 dB, being of $\sim 15\%$ for both SC-FEC and IC-FEC strategies.

Finally, in the case of Flex-FEC strategy, the EGN based analysis performed in the previous section (Figure 4.6) is also performed for the different DBP methods considered in this section. Figure 4.10c shows the results corresponding to the best performing $[\text{OH}_{64\text{QAM}}, \text{OH}_{16\text{QAM}}]$ pair. The optimum set of OHs were found to be $[\text{OH}_{64\text{QAM}} = 40\%, \text{OH}_{16\text{QAM}} = 5\%]$ for CDE, $\text{DBP}_{16\text{QAM}}$ and DBP_{WB} , whilst it is of $[\text{OH}_{64\text{QAM}} = 36\%, \text{OH}_{16\text{QAM}} = 8\%]$ for DBP and $\text{DBP}_{64\text{QAM}}$. Figure 4.10c shows that again the gains achieved by the application of each DBP strategy over CDE are identical to those achieved with SC-FEC ($\sim 20\%$ using DBP and $\text{DBP}_{64\text{QAM}}$ and $\sim 30\%$ using DBP_{WB}). Moreover, the application of $\text{DBP}_{16\text{QAM}}$ is again insignificant over the $\text{DBP}_{64\text{QAM}}$ and CDE. Comparing the results of Figure 4.10b and Figure 4.10c, we verify that the MRs obtained (at the optimum PRs) are similar to those obtained with the SC-FEC (within $\sim 1\%$ difference). However, in contrast with the SC-FEC case, there is a steep performance degradation when we slightly change the PR for all DBP strategies. Therefore, the use of the Flex-FEC strategy requires a more precise optimization of the system parameters, in order to get its optimal performance.

4.7 Conclusions

In this chapter, we propose a 400G frequency-hybrid superchannels, composed of two edge PM-16QAM carriers and a central PM-64QAM carrier. Its performance is experimentally assessed in an WDM transmission system composed of 9 identical 400G frequency-hybrid superchannels. The proposed solution proves to be compatible with the 62.5 GHz grid slot, thus enabling a spectral efficiency of 6.4 bits/s/Hz, while achieving a maximum transmission distance of 2500 km. The experimental results are supported by complementary OptSimTM simulations and analytical EGN model predictions.

The power-ratio between the superchannel carriers is analyzed in the linear and nonlinear regimes of operation, in order to evaluate its impact on the performance of the transmission system. The system is also evaluated in terms of maximum reach and

optimum average power per superchannel, under three different FEC paradigms. The SC-FEC scheme, based on the average superchannel BER, is found to be the more robust approach for frequency-hybrid superchannels, showing a smoother dependence on the power-ratio between carriers, thus tolerating larger uncertainty on the system parameters optimization. In addition, SC-FEC does not require individual optimization of FEC overheads per carrier, like in the Flex-FEC technique, thereby simplifying the transmitter and receiver implementations. In contrast, the residual performance gain that can be achieved by Flex-FEC encoding requires a very precise optimization of several system parameters such as launched power, power-ratio and FEC overhead, that might not be feasible in a real application. As opposed to it, SC-FEC enables a simpler and more error-tolerant design of frequency-hybrid transmission systems.

The possible performance improvement achieved by the use of advanced DBP techniques, and its implications on the optimum power-ratio and optimum launched power is also investigated. We notice that the unequal transmitted power per carriers creates new challenges and opportunities for the implementation of DBP in frequency-hybrid systems. We demonstrate a maximum transmission distance of ~ 2300 km and ~ 1600 km for the SC-FEC/Flex-FEC and IC-FEC strategies, respectively, when applying self-carrier interference DBP compensation of the PM-64QAM carrier only. We also demonstrate that the nonlinear compensation of all carriers of a frequency-hybrid superchannel might not be worthy. Indeed, most of the benefit provided by DBP is achieved by the standalone compensation of the central PM-64QAM carrier, thereby enabling a reduction of DBP complexity by a factor of roughly $2/3$. Finally, an extended analytical study revealed that jointly compensating nonlinear impairments applying DBP to the overall superchannel signal received through a wideband receiver can potentially bring an additional improvement of about 10% over independent application of DBP for the SC-FEC and Flex-FEC strategies, while this gain becomes negligible for the IC-FEC strategy.

References

- [1] S. B. Amado, F. P. Guiomar, N. J. Muga, R. M. Ferreira, J. D. Reis, S. M. Rossi, A. Chiuchiarelli, J. R. F. Oliveira, A. L. Teixeira, and A. N. Pinto, “Low complexity advanced DBP algorithms for Ultra-Long-Haul 400G transmission systems,” *J. Lightwave Technol.*, vol. 34, no. 8, pp. 1793–1799, Apr 2016.
- [2] F. P. Guiomar, R. Li, C. R. S. Fludger, A. Carena, and V. Curri, “Hybrid modulation formats enabling elastic fixed-grid optical networks,” *IEEE/OSA Journal of Optical Communications and Networking*, vol. 8, no. 7, pp. A92–A100, July 2016.
- [3] J. D. Reis, V. Shukia, D. R. Stauffer, and K. Glass, “Technology options for 400G implementation,” Optical Internetworking Forum, Tech. Rep., 2015.
- [4] “The next generation of coherent optical,” Infinera, Tech. Rep., 2016.
- [5] S. B. Amado, F. P. Guiomar, N. J. Muga, A. Nespola, L. Bertignono, A. Carena,

-
- and A. N. Pinto, “400G frequency-hybrid superchannel for the 62.5 GHz slot,” in *Proc. Opt. Fiber Commun. Conf. (OFC)*, paper Th4D.4, Mar. 2017.
- [6] A. Carena, G. Bosco, V. Curri, Y. Jiang, P. Poggiolini, and F. Forghieri, “EGN model of non-linear fiber propagation,” *Opt. Express*, vol. 22, no. 13, pp. 16 335–16 362, 2014.
- [7] D. Rafique, T. Rahman, A. Napoli, S. Calabro, and B. Spinnler, “Technology options for 400 Gb/s PM-16QAM flex-grid network upgrades,” *Photonics Technology Letters, IEEE*, vol. 26, no. 8, pp. 773–776, April 2014.
- [8] E. Agrell, J. Lassing, E. Strom, and T. Ottosson, “Gray coding for multilevel constellations in gaussian noise,” *IEEE Trans. Inf. Theory*, vol. 53, no. 1, pp. 224–235, 2007.
- [9] T. Rahman, D. Rafique, B. Spinnler, A. Napoli, M. Bohn, T. Koonen, C. Okonkwo, and H. de Waardt, “Digital subcarrier multiplexed hybrid QAM for data-rate flexibility and ROADM filtering tolerance,” in *Optical Fiber Communication Conference*. Optical Society of America, 2016, p. Tu3K.5.
- [10] T. Rahman, A. Napoli, D. Rafique, B. Spinnler, M. Kuschnerov, I. Lobato, B. Clouet, M. Bohn, C. Okonkwo, and H. de Waardt, “On the mitigation of optical filtering penalties originating from ROADM cascade,” *IEEE Photonics Technology Letters*, vol. 26, no. 2, pp. 154–157, Jan 2014.
- [11] V. Curri, A. Carena, P. Poggiolini, R. Cigliutti, F. Forghieri, C. R. Fludger, and T. Kupfer, “Time-division hybrid modulation formats: Tx operation strategies and countermeasures to nonlinear propagation,” in *Proc. Optical Fiber Communication Conf. and Exposition (OFC)*, paper Tu3A.2, 2014.
- [12] P. Poggiolini, A. Carena, V. Curri, G. Bosco, and F. Forghieri, “Analytical modeling of nonlinear propagation in uncompensated optical transmission links,” *IEEE Photon. Technol. Lett.*, vol. 23, no. 11, pp. 742–744, 2011.
- [13] A. Carena, V. Curri, G. Bosco, P. Poggiolini, and F. Forghieri, “Modeling of the impact of nonlinear propagation effects in uncompensated optical coherent transmission links,” *J. Lightw. Technol.*, vol. 30, no. 10, pp. 1524–1539, 2012.
- [14] P. Poggiolini, “The GN model of non-linear propagation in uncompensated coherent optical systems,” *Journal of Lightwave Technology*, vol. 30, no. 24, pp. 3857–3879, Dec 2012.
- [15] A. Stark, Y.-T. Hsueh, T. Detwiler, M. Filer, S. Tibuleac, and S. Ralph, “System performance prediction with the Gaussian noise model in 100G PDM-QPSK coherent optical networks,” *Journal of Lightwave Technology*, vol. 31, no. 21, pp. 3352–3360, Nov 2013.
-

- [16] P. Poggiolini, G. Bosco, A. Carena, V. Curri, Y. Jiang, and F. Forghieri, "The GN-model of fiber non-linear propagation and its applications," *Journal of Lightwave Technology*, vol. 32, no. 4, pp. 694–721, Feb 2014.
- [17] R.-J. Essiambre, G. Kramer, P. J. Winzer, G. J. Foschini, and B. Goebel, "Capacity limits of optical fiber networks," *J. Lightw. Technol.*, vol. 28, no. 4, pp. 662–701, 2010.
- [18] P. Bayvel, R. Maher, T. Xu, G. Liga, N. A. Shevchenko, D. Lavery, A. Alvarado, and R. I. Killey, "Maximizing the optical network capacity," *Philosophical Transactions of the Royal Society of London A: Mathematical, Physical and Engineering Sciences*, vol. 374, no. 2062, 2016.
- [19] A. Carena, G. Bosco, V. Curri, P. Poggiolini, M. T. Taiba, and F. Forghieri, "Statistical characterization of PM-QPSK signals after propagation in uncompensated fiber links," in *36th European Conference and Exhibition on Optical Communication*, Sept 2010, pp. 1–3.
- [20] F. Vacondio, C. Simonneau, L. Lorcy, J. C. Antona, A. Bononi, and S. Bigo, "Experimental characterization of gaussian-distributed nonlinear distortions," in *2011 37th European Conference and Exhibition on Optical Communication*, Sept 2011, pp. 1–3.
- [21] A. Nespola, S. Straullu, A. Carena, G. Bosco, R. Cigliutti, V. Curri, P. Poggiolini, M. Hirano, Y. Yamamoto, T. Sasaki, J. Bauwelinck, K. Verheyen, and F. Forghieri, "GN-Model validation over seven fiber types in uncompensated PM-16QAM Nyquist-WDM links," *IEEE Photon. Technol. Lett.*, vol. 26, no. 2, pp. 206–209, Jan 2014.
- [22] I. Fatadin, D. Ives, and S. Savory, "Blind equalization and carrier phase recovery in a 16-QAM optical coherent system," *J. Lightw. Technol.*, vol. 27, no. 15, pp. 3042–3049, 2009.
- [23] F. P. Guiomar, S. B. Amado, C. S. Martins, and A. N. Pinto, "Time domain Volterra-based digital backpropagation for coherent optical systems," *J. Lightw. Technol.*, vol. 15, no. 33, pp. 3170–3181, August 2015.
- [24] X. Zhou, J. Yu, M.-F. Huang, Y. Shao, T. Wang, L. Nelson, P. Magill, M. Birk, P. I. Borel, D. W. Peckham, and R. Lingle, "64 Tb/s (640×107 Gb/s) PDM-36QAM transmission over 320 km using both pre- and post-transmission digital equalization," in *Proc. Optical Fiber Communication Conf. and Exposition (OFC)*, 2010.
- [25] L. B. Du and A. J. Lowery, "The validity of "odd and even" channels for testing all-optical OFDM and Nyquist WDM long-haul fiber systems," *Opt. Express*, vol. 20, no. 26, pp. B445–B451, Dec 2012.

- [26] R. Dar and P. J. Winzer, “On the limits of digital back-propagation in fully loaded WDM systems,” *IEEE Photonics Technology Letters*, vol. 28, no. 11, pp. 1253–1256, June 2016.
- [27] A. Arduino, A. Carena, and V. Curri, “Flexible fec optimization for time-domain hybrid modulation formats,” in *Advanced Photonics 2015*. Optical Society of America, 2015, p. SpM4E.4.
- [28] K. Kojima, D. S. Millar, T. Koike-Akino, K. Parsons, S. Kametani, and T. Sugihara, “Maximizing transmission capacity of superchannels using rate-adaptive FEC,” in *2014 The European Conference on Optical Communication (ECOC)*, Sept 2014, pp. 1–3.
- [29] A. Ghazisaeidi, L. Schmalen, I. F. de Jauregui Ruiz, P. Tran, C. Simonneau, P. Brindel, and G. Charlet, “Transoceanic transmission systems using adaptive multirate FECs,” *Journal of Lightwave Technology*, vol. 33, no. 7, pp. 1479–1487, April 2015.
- [30] A. Ghazisaeidi, I. F. de Jauregui Ruiz, L. Schmalen, P. Tran, C. Simonneau, E. Awwad, B. Uscumlic, P. Brindel, and G. Charlet, “Submarine transmission systems using digital nonlinear compensation and adaptive rate forward error correction,” *Journal of Lightwave Technology*, vol. 34, no. 8, pp. 1886–1895, April 2016.
- [31] E. F. Mateo and G. Li, “Compensation of interchannel nonlinearities using enhanced coupled equations for digital backward propagation,” *Appl. Opt.*, vol. 48, no. 25, pp. F6–F10, Sep 2009.

Chapter 5

Conclusions and Future Work

As we are moving to a more connected world, the demand for faster connections leveraged the development and adoption of new optical transmission paradigms for telecommunication networks. Nowadays, coherent detection, together with advanced modulation formats and digital signal processing (DSP) are the best performing technologies, enabling longer transmission distances and higher bit-rates. However, the persistent demand for higher capacity continues to push the development of innovative technologies that aim to increase even more the bit rate-reach product of existing optical transmission systems.

Superchannel-based transmission systems composed of higher-order modulation formats have been considered a potential candidate for next-generation networks. These systems can provide better wavelength management and higher spectral efficiency, although, at the expense of a higher sensibility to fiber nonlinear effects. Given so, in the framework of this thesis, we focus our study on the development and implementation of techniques that counteract the signal nonlinearities while being suitable to be deployed in superchannels systems. In this final chapter, the most relevant conclusions are summarized and envisioned future research topics are discussed.

5.1 Conclusions

State-of-the-art nonlinear equalization (NLE) techniques are complex and have a challenging real-time implementation. The development of low-complexity NLE techniques is a research topic of interest, where several low-complexity SSFM- and VSNE-based digital backpropagation (DBP) techniques have been proposed. In this thesis, some of these low-complexity DBP techniques were evaluated over a wavelength-division multiplexing (WDM) ultra-long-haul (ULH) transmission system composed of 5 dual-carrier PM-16QAM 400G superchannels. Taking into account the reduction of complexity, different regions of operations can be considered, where the maximum transmission distance will be related to the number of DBP steps to be applied. We demonstrated that it is possible to reduce the W-SSFM and W-VSNE complexity and still extend the maximum transmission reach over CDE. Furthermore, the W-VSNE allows a 90% maximum reduction of the number of DBP steps, a 85% maximum reduction of

the number of real multiplications, and up to 90% total latency reduction comparing to the standard SSFM technique. Moreover, since the W-VSNE is composed by a set of N_k parallel filters, the tradeoff between performance and computational complexity can be handled more easily. The results obtained in this work show the potential of the W-VSNE to be applied as an alternative low-complexity and efficient DBP technique for high-speed ULH transmission systems.

Hybrid modulation formats have been recently proposed for fulfilling the demand for higher capacity of future networks. Such technique is of interest since it offers a finer adjustment of the SE, providing a new degree of freedom in the optimization of the system performance. With this in mind, we have proposed a 400G frequency-hybrid superchannel system, composed of two edge PM-16QAM carriers and a central PM-64QAM carrier, that fits in the 62.5 GHz grid slot. Comparing with a 400G superchannel composed of uniform PM-16QAM carriers in the 75 GHz grid slot, the proposed solution allows for an increase of the SE from 5.33 bits/s/Hz to 6.4 bits/s/Hz. The frequency-hybrid superchannel was experimentally evaluated in an WDM transmission system and the experimental results were validated by OptSimTM simulations and analytical EGN model predictions.

The power-ratio between modulation-formats plays an important role on the performance of hybrid-based modulation format systems. We have evaluated the power-ratio under different FEC paradigms, aiming to determine the most suitable strategy for the proposed frequency-hybrid superchannel transmission system. We showed that the SC-FEC scheme is the more robust approach since it does not require the individual optimization of FEC overheads per carrier, like the Flex-FEC scheme. Despite the Flex-FEC shows a small improvement of the system performance over the SC-FEC, it requires a more precise optimization of the channel parameters. On the other hand, although the IC-FEC approach has the shortest transmission distance and the higher power-ratio between carriers, it requires a smaller optimal power.

We also investigated the performance gains obtained by the application of different DBP techniques in the frequency-hybrid superchannel. We showed that the application of DBP only over the carrier that transports the highest-order modulation format gives a significant performance improvement, while reducing the DBP complexity approximately by 2/3. Finally, an extended analytical study revealed that jointly compensating nonlinear impairments applying DBP to the overall superchannel signal received through a wideband receiver can potentially bring an additional improvement of about 10% over independent application of DBP for the SC-FEC and Flex-FEC strategies, while this gain becomes negligible for the IC-FEC strategy. However, this would require the use of a wideband coherent receiver or a set of coherent receivers with a bank of phase locked LO lasers together with total-field or couple-equations DBP, making its implementation more challenging.

5.2 Future work

The superchannels solution together with the use of efficient equalization and mitigation DBP techniques proposed in this thesis have opened new possibilities and research directions to approach the issue of nonlinear impairment compensation in coherent optical fiber systems. Resulting from the efforts of this work, several research directions remain as open and challenging topics, from which we highlight the following:

- The heterogenous and dynamic traffic in current optical transmission systems have been making reconfigurable optical transceivers the probable paradigm for future optical networks. These transceivers adapt their parameters to achieve the best performance and power efficiency depending on the nature of the traffic [1, 2]. In this sense, the study of hybrid-modulation format based superchannel can be extended to account for the application of different baud-rates, overhead FECs and/or guard-band between superchannel carriers, in order to assess its suitability to different types of traffic. Hybrid-modulation format based superchannels might prove to be an efficient technique for reconfigurable transceiver networks.
- Deployed optical networks typically have a meshed network architecture where the signal passes through multiple ROADMs [3]. These might be based on WSSs, which in turn induces penalties due to the optical filtering. It might be interesting to further study the performance of the nonlinear compensation algorithms in systems using higher-order modulation formats or hybrid-modulation formats based superchannels that are subjected to optical filtering. The mitigation of optical filtering penalties can also be applied to the proposed systems and the performance improvement brought by the equalization method can be evaluated.
- In ULH communications, besides deterministic nonlinear effects, the accumulation of ASE noise and its interaction with the optical signal might lead to a significant performance limitation. The majority of the nonlinear compensation techniques do not take into consideration the interaction of ASE noise with the optical signal, neither the interaction between nonlinear and non-deterministic linear effects, such as PDL and PMD [4]. Techniques to mitigate such interactions should also be proposed as a way of improving system performance.
- Probabilistic shaping has been pointed out a promising solution for near-future optical networks. Probabilistic shaping have been demonstrated in optical channels as a way to close the gap with the Shannon limit. Additionally, it also allow us to increase the SE and bit-rate granularity of the optical transmission system [5]. The application of Volterra-based DBP algorithms can be applied over probabilistic shaped systems to evaluate the DBP gains over such systems.
- The capacity of SSFM is reaching its limits. The use of better fibers, with low fiber loss or low nonlinear coefficient and wider amplification bands is a possible approach for the near future networks. However, none of these techniques can provide a sustainable path to overcome the optical network capacity crunch. It

is expected that future networks would be based in multi-core and/or multi-mode fibers [4, 6]. Such fibers have been extensively explored in the last couple of years, however they still present a reduced transmission reach and new challenges in terms of channel impairments equalizations, since they suffer from different impairments, such as crosstalk and interferences between cores and/or modes. Therefore, new and efficient digital signal processing techniques have to be developed, and Split-step and Volterra-based DBP techniques can be adapted to this kind of fibers, in order to evaluate their benefits in such optical systems.

References

- [1] D. A. Morero, M. A. Castrilln, A. Aguirre, M. R. Hueda, and O. E. Agazzi, “Design tradeoffs and challenges in practical coherent optical transceiver implementations,” *Journal of Lightwave Technology*, vol. 34, no. 1, pp. 121–136, Jan 2016.
- [2] J. D. Reis, V. Shukia, D. R. Stauffer, and K. Glass, “Technology options for 400G implementation,” Optical Internetworking Forum, Tech. Rep., 2015.
- [3] V. A. J. M. Sleiffer, D. van den Borne, V. Veljanovski, M. Kuschnerov, M. Hirano, Y. Yamamoto, T. Sasaki, S. L. Jansen, and H. de Waardt, “Transmission of 448 Gb/s dual-carrier POLMUX-16QAM over 1230 km with 5 flexi-grid roadm passes,” in *OFC/NFOEC*, March 2012, pp. 1–3.
- [4] A. Amari, O. A. Dobre, R. Venkatesan, O. S. S. Kumar, P. Ciblat, and Y. Jaoun, “A survey on fiber nonlinearity compensation for 400 Gbps and beyond optical communication systems,” *IEEE Communications Surveys Tutorials*, vol. PP, no. 99, pp. 1–1, 2017.
- [5] K. Roberts, Q. Zhuge, I. Monga, S. Gareau, and C. Laperle, “Beyond 100 Gb/s: capacity, flexibility, and network optimization,” *J. Opt. Commun. Netw.*, vol. 9, no. 4, pp. C12–C24, Apr 2017.
- [6] P. J. Winzer, “Scaling optical fiber networks: Challenges and solutions,” *Opt. Photon. News*, vol. 26, no. 3, pp. 28–35, Mar 2015.